Technische Universität Ilmenau

Faculty of Computer Science and Automation

Department of Control Engineering

Universitetet i Agder

Faculty of Engineering and Science

Department of Engineering Sciences

Master's Thesis

of Benjamin Voß

Fractional-Order Controller Design with Partial Pole-Zero Cancellation

Supervisors:	Prof. Dr.-Ing. Johann Reger (TU Ilmenau) Prof. Dr.-Ing. Michael Ruderman (Universitetet i Agder) Dr.-Ing. Chistoph Weise (TU Ilmenau)
Submission Date:	March 01, 2022

Abstract

Considering a plant that contains a non-minimum phase zero or unstable pole, limits on the achievable performance of the closed-loop system are imposed. However, a straight-forward compensation cannot be applied as it renders the process internally unstable.

In this work, the partial cancellation of right-half plane zeros/poles is investigated and applied within a loop-shaping controller design procedure. The key idea is to split the zero/pole into a product of fractional-order *pseudo* zeros/poles. Those located in the stable region can be subjected to a stable fractional-order cancellation term, hence without introducing instability. This concept is extended to conjugate complex zeros/poles. Also stable but low-damped poles are considered. Here, a cancellation of those pseudo poles closest to the stability border entirely erases the oscillatory behavior. Furthermore, we include implicit fractional-order terms that yield the same asymptotic frequency characteristics, however differ in the crossover region. Regarding a non-minimum phase zero, the implicit cancellation achieves a higher phase margin and steeper magnitude slope.

This concept is applied to enhance the robust control of a two-mass oscillator with non-collocated actuation and measurement, as well as an artificially injected input time-delay. Two cases are considered: a dominant and a small delay. A detailed derivation of the plant model reveals a nonlinear input gain and non-white process noise as three dominant harmonics are detectable. The plant is controlled by a PI-lead based controller with feedforward action. The delay approximation with Padé-terms leads to a non-minimum phase zero which is subjected to partial cancellation. For comparison, a two-degree of freedom reference controller is designed using the $\mathcal{H}_\infty$ framework that yields a similar order and frequency-response.

Detailed experimental and simulation studies confirm the expected similarity for disturbance attenuation, with the $\mathcal{H}_\infty$ controller being more robust against delay uncertainties. The tracking performance is evaluated with commonly used metrics. Best performance is achieved with the fractional-order controller due to its feedforward action based on the model-inverse. This, however, may lead to saturation issues for step-like reference signals. Due to the weighted sensitivities, the considered $\mathcal{H}_\infty$ framework does not allow similar feedforward action. Thus, the $\mathcal{H}_\infty$ controller is significantly slower but more robust against both, delay uncertainties and step-like reference changes.

Kurzfassung

Im Falle einer Strecke mit nicht-minimalphasiger Nullstelle oder instabilem Pol ist die erreichbare Regelgüte grundlegend limitiert. Direkte Kompensation kann die interne Stabilität nicht garantieren.

Die vorliegende Arbeit behandelt die partielle Pol-Nullstellen-Kürzung sowie ihre Anwendung im Rahmen des Reglerentwurfs an der offenen Kette. Die Kernidee liegt in der Aufteilung der Nullstelle bzw. des Pols in ein Produkt von *Pseudo*-Nullstellen/-Polen nicht-ganzzahliger, d.h. *fraktionaler*, Ordnung. All jene innerhalb des Stabilitätsbereichs können mithilfe eines Terms nicht-ganzzahliger Ordnung gekürzt werden, ohne die Stabilität zu gefährden. Dieses Konzept wird um konjugiert-komplexe Nullstellen/Pole erweitert. Im Falle *stabiler* Polpaare mit geringer Dämpfung führt eine Kürzung nur desjenigen *Pseudo*-Polpaars, welches am nächsten der Stabilitätsgrenze liegt, zur Beseitigung der Oszillationen. Desweiteren werden implizite Terme fraktionaler Ordnung in die Betrachtungen einbezogen. Diese führen zu vergleichbarem asymptotischen Verhalten, unterscheiden sich jedoch im Bereich der Schnittfrequenz deutlich. Bei partieller Kürzung einer nicht-minimalphasigen Nullstelle erzielt die implizite Darstellung einen größeren Phasenrand sowie höhere Steigung des Amplitudengangs.

Dieses Konzept wird im Reglerentwurf für einen Zwei-Massen-Oszillator angewendet, wobei der Messpunkt vom Ansteuerungspunkt verschieden ist. Zusätzlich verfügt die Strecke über eine künstlich eingefügte, teils dominante, Eingangs-Totzeit. Das detaillierte Modell beinhaltet eine Eingangs-Nichtlinearität sowie ein Prozessrausch-Modell mit Harmonischen. Die PI-Lead basierte, robuste Regelung wird mit Vorsteuerung realisiert. Die Padé-Approximation der Totzeit führt zu einer nicht-minimalphasigen Nullstelle, welche eine partielle Kürzung erfährt. Zum Vergleich wird ein Zwei-Freiheitsgrade-Regler mit ähnlicher Ordnung und Frequenzcharakteristik mittels $\mathcal{H}_\infty$ Synthese entworfen.

Die Regler-Ähnlichkeit im Hinblick auf Störunterdrückung bestätigt sich in simulativen und experimentellen Untersuchungen, wobei der $\mathcal{H}_\infty$ Regler robuster gegenüber Totzeit-Unsicherheiten ist. Das Führungsverhalten wird mithilfe gängiger Metriken evaluiert. Der Regler mit fraktionalen Elementen erzielt durchweg die besten Ergebnisse aufgrund der Vorsteuerung, welche auf der Modell-Inversen basiert. Jedoch kann diese, beispielsweise für Referenzsprünge, zu Sättigungsproblemen führen. Für den $\mathcal{H}_\infty$ Regler sind solche unproblematisch. Dieser zeigt deutlich langsameres, hingegen robusteres Verhalten mit Blick auf Totzeitunsicherheiten. Die Ursachen für die Unterschiede der Vorsteuerungen liegen in den gewichteten Sensitivitäten des $\mathcal{H}_\infty$ Reglers, welche ein ähnlich aggressives Verhalten nicht zulassen.

Acknowledgment

The accomplishment of this thesis was only possible thanks to the support that I received from many parties.

From the first idea to the completion, Dr.-Ing. Christoph Weise guided me through this work. He was available to answer my questions at any time, helped me with constructive feedback and comments regarding both the research and the writing. With his ideas, he encouraged me to immerse myself in the fractional-order world.

I thank Prof. Dr.-Ing. Johann Reger for giving me the opportunity to work on this project and to be part of the exchange. With valuable remarks and suggestions he drew my attention on fruitful ideas and, in addition, helped me improving my writing.

Furthermore, I thank Prof. Dr.-Ing. Michael Ruderman for the organization and close supervision during my entire stay in Grimstad, Norway. He welcomed me at the Universitetet i Agder and helped me with the laboratory setup. Moreover, I value his expert advice for the experiments and evaluation as well as the supportive feedback.

During the stay in Grimstad, I was lucky to share the office with Riccardo Checchin and I am grateful for the inspiring ideas and discussions as well as the support in the final stage.

I also received great support from the International Office of the Technische Universität Ilmenau.

Finally, I am very grateful to my close family and friends for their patience, moral support and backing in every way.

Remark:

This master's thesis is part of a cooperation of the Universitetet i Agder (UiA) and the Technische Universität Ilmenau (TUIl) within the area of dynamics and control of fractional-order systems and compensators for non-minimum phase systems. The exchange is funded by the DAAD and RCN.

Contents

List of Tables

List of Figures

Notation

Symbol	Description
$\mathbb{N}$	Set of natural numbers
$\mathbb{Q}$	Set of rational numbers
$\mathbb{Q}_+$	Set of positive rational numbers
$\mathbb{R}$	Set of real numbers
$\mathbb{R}_+$	Set of positive real numbers
$\mathbb{C}$	Set of complex numbers
$\mathbb{C}_+$	Set of complex numbers with positive real part
$\mathbb{C}_-$	Set of complex numbers with negative real part
$\mathbb{C}_\alpha$	Set of complex numbers with $\lvert\arg(\cdot)\rvert > \alpha\frac{\pi}{2}$
${}_{t_0}\mathcal{D}_t^\alpha$	Caputo fractional-order derivative operator
${}_{t_0}^{\mathrm{R}}\mathcal{D}_t^\alpha$	Riemann-Liouville fractional-order derivative operator
$\mathcal{D}^\alpha$	Fractional-order derivative operator with lower limit $t_0 = 0$
$E_{\alpha,\beta}(\cdot)$	Two-parameter Mittag-Leffler function
$\mathcal{F}_\mathrm{l}(\cdot,\cdot)$	Lower linear fractional transformation
$f^{(n)}(\cdot)$	n-th order derivative of the function $f(\cdot)$, $n \in \mathbb{N}$
$\Gamma(\cdot)$	Euler's gamma function
$\mathcal{L}\{\cdot\}(s)$	Laplace transform
$\bar{\sigma}(\cdot)$	Maximum singular value
$\lVert w\rVert_2$	$\mathcal{L}_2$ norm of the piecewise continuous time signal $w = w(t)$
$\lVert P\rVert_\infty$	$\mathcal{H}_\infty$ norm of the transfer function $P(s)$
γ, γ_min	(Minimal) upper bound on the $\mathcal{H}_\infty$ norm: $\gamma_\mathrm{min} \leq \gamma$
ω_0	Absolute value of a complex number
φ	Argument of a complex number
ω_c	Open-loop crossover frequency
A_r	Gain margin
Φ_r	Phase margin
$S_u(s)$	Input sensitivity function
$S_y(s)$	Output sensitivity function
$T(s)$	Complementary sensitivity function
$S_{yd}(s)$	Input disturbance sensitivity including the communication delay

Symbol	**Description**
α	Fractional-order exponent, $\alpha \in (0,1]$ if not further specified
ν	Positive integer, $\nu \in \mathbb{N}$
$H_\alpha(s)$	Oustaloup approximation of s^α
ω_l, ω_h	Lower and upper limit of the Oustaloup approximation, ω_i in rad/s
N_oust	Order of the Oustaloup approximation, $N_\mathrm{oust} \in \mathbb{N}$
$C(s)$	Controller
$G(s)$	Non-minimum phase/unstable plant
$\hat{G}(s)$	Stable and minimum phase part of $G(s)$
$D_1^k(s)$	First-order term with zero/pole $z < 0$
$D_2^k(s)$	Second-order term with conjugate complex zeros/poles $z, \bar{z} \in \mathbb{C}_-$
$P_2(s)$	Second-order term with conjugate complex poles $p, \bar{p} \in \mathbb{C}_-$
$Z_1^k(s)$	First-order term with zero/pole $z > 0$
$Z_2^k(s)$	Second-order term with conjugate complex zeros/poles $z, \bar{z} \in \mathbb{C}_+$
$X_{z,\alpha}^k(s)$	Representation of an explicit pseudo zero/pole
$\tilde{X}_{z,\alpha}^k(s)$	Representation of an implicit pseudo zero/pole
$\mathcal{X}_{z,\alpha}^k(s)$	Pair of explicit conjugate complex pseudo zeros/poles
$\tilde{\mathcal{X}}_{z,\alpha}^k(s)$	Pair of implicit conjugate complex pseudo zeros/poles
$Q_{z,\nu}^k(s)$	Partial cancellation of an explicit pseudo pole/zero
$\tilde{Q}_{z,\nu}^k(s)$	Partial compensation of an implicit pseudo pole/zero
$\mathcal{Q}_{z,\nu}^k(s)$	Partial cancellation of explicit conj. compl. pseudo poles/zeros
$\tilde{\mathcal{Q}}_{z,\nu}^k(s)$	Partial compensation of implicit conj. compl. pseudo poles/zeros

Symbol	**Description**	**Unit**
d, D	Gravitational force of the active and passive mass	N
f_s	Sampling frequency	Hz
g	Gravitational acceleration	m/s^2
k	Spring constant	N/m
m, M	Active and passive mass	kg
η, ζ	Viscous damping of the active and passive mass	kg/s
Ψ	Actuator electromotive force constant	Vs/m
R	Actuator resistance	V/A
r_0, r_1	Starting point and endpoint of a set-point transition	mm
τ, τ_1, τ_2	Communication delay and the two nominal values	s
T_s	Sample time	s
T_t	Duration of a set-point transition	s
ω_0	Eigenfrequency of the plant model	rad/s
Ω_d	Frequency range of the input disturbance	rad/s
A_j	Amplitude of the jitter signal	V
ω_j	Frequency of the jitter signal	rad/s
u_d	Nominal feedforward action to compensate gravitational forces	V
u_ss	Steady-state input to compensate the gravitational forces	V
e_RMS	Root-mean-square error	mm
$\lvert e_\mathrm{max}\rvert$	Maximum absolute error	mm
$\lvert u_\mathrm{max}\rvert$	Maximum absolute control effort	V
e_SNR	Signal-to-noise ratio of the control error and input disturbance	-
u_SNR	Signal-to-noise ratio of the control effort and input disturbance	-
e_ITAE	Integral time-multiplied absolute error	ms^2
e_IAE	Integral absolute error	ms
T_IAE	Settling time	s

Symbol	**Description**
$G_{yu}(s)$	Input-output behavior of the plant
$G_\mathrm{d}(s)$	Delay element
$R_j(s)$	j-th order Padé-approximation of $G_\mathrm{d}(s)$
$G(s)$	Plant model including the communication delay $G_\mathrm{d}(s)$
$\tilde{G}(s)$	Plant model including the Padé-approximation $R_j(s)$ of G_d
$d_u(t)$, $d_y(t)$	Input and output disturbance
$e(t)$	Control error
$r(t)$	Reference signal
$u(t)$	Control signal
$u^*(t)$	Feedforward action based on the model-inverse
$x(t)$	Plant state
$y(t)$	Plant output
x_0, $x_{0,\mathrm{d}}$, $x_{0,\mathrm{t}}$	Initial state vector, for disturbance attenuation and tracking
A	System matrix
B	Input matrix
C	Output matrix
E	Disturbance matrix
I	Identity matrix
$v(t)$	Performance output
$w(t)$	External input
$P(s)$	Generalized plant
$W_1(s)$, $W_2(s)$	Weight functions for the performance outputs v_1, v_2
$T_{v_1 r}(s)$	Weighted sensitivity function: from r to v_1
$T_{v_1 d_u}(s)$	Weighted sensitivity function: from d_u to v_1
$T_{v_2 r}(s)$	Weighted sensitivity function: from r to v_2
$T_{v_2 d_u}(s)$	Weighted sensitivity function: from d_u to v_2
$C_{\infty,i}(s)$	2DOF $\mathcal{H}_\infty$ controller
$F_{\mathrm{FO},i}(s)$	Feedforward action of fractional-order controller with prefilter
$C_{\mathrm{FO},i}(s)$	PI-lead based controller using fractional-order elements
$K_\mathrm{PIL}(s)$	PI-lead controller
$K_\mathrm{PI}(s)$	PI controller
$K_{\mathrm{PI}^\mu}(s)$	PI$^\mu$ controller

Abbreviations

2DOF	two-degree of freedom.
BIBO	bounded-input bounded-output.
EMF	back electromotive force.
FO	fractional-order.
HP	high-pass.
IAE	integral of absolute error.
IO	integer-order.
ITAE	integral of time-multiplied absolute error.
LHP	left-half plane.
LP	low-pass.
LTI	linear time-invariant.
PI	proportional-integral.
RHP	right-half plane.
RMS	root-mean-square.
SISO	single-input single-output.
SNR	signal-to-noise ratio.

1 Introduction

It is well known that non-minimum phase zeros and unstable poles impose limits on the achievable performance of the closed-loop system. These restrictions also apply to open-loop tuning methods in terms of bounds on the crossover frequency, gain and phase margins [2, 39]. Furthermore, a compensation cannot ensure internal stability, hence the system may destabilize in case of disturbances or parameter uncertainties.

This is where fractional-order operators come into play, i.e. derivatives of non-integer order α. Although the idea of generalized derivatives is rather old and has been used e.g. by Abel to describe the tautochrone problem back in 1823 already [29], it has gained high popularity in the past decades only. Nowadays, applications can be found in many fields, e.g. electro-chemistry [7], bio-engineering [21] and control [5, 29–31, 35], to mention a few. Due to the practical relevance of PI and PID (proportional-integral-derivative) control (it makes roughly 90 % of the applied control in industry [18, 49]), these concepts have been generalized to allow integration and differentiation of non-integer order. In terms of the Laplace transform, this yelds 's^{α}' and gives a further degree of freedom. Advantages are for example less phase loss for the fractional integrator compared to the integer-order case as well as an arbitrary magnitude slope. Furthermore, these controllers can be tuned to be robust against gain variations by means of a constant phase in the open-loop crossover region, i.e. the iso-damping property [34, 35].

Let us come back to the zero or pole in the right-half complex plane. Allowing non-integer orders, we may split an integer-order term in the following way

$$(s-1) \quad \longrightarrow \quad (s^{0.5}-1)(s^{0.5}+1)$$

where the stable part can be compensated without introducing instability. This idea can be generalized to an almost arbitrary order [27] that makes straight-forward tuning possible. It is, however, restricted to single non-minimum phase zeros or unstable poles. What if the plant contains a conjugate complex pair of poles, either unstable or stable but low-damped?

One of the reasons for various applications of the fractional derivative is the fact that it is a non-local operator. Therefore, processes containing memory phenomena can easily be modeled [29, p. 4]. In the case of controller design, however, this shows to be a drawback when it comes to implementation, as only limited memory is available in physical real-time systems. For this reason, higher-order approximations are commonly used to meme the fractional-order operator in the relevant frequency range (e.g. [29, 31]). A reasonable approximation of the fractional derivative operator over a broad frequency range starts with five states. Most examples in the literature compare fractional-order controllers to classical PID controllers. However, due to the significant differences of the controller orders, there is a lack of comparability. To overcome this problem, it is more natural to choose a design procedure for comparison that leads to higher-order controllers as well, e.g. the $\mathcal{H}_\infty$ synthesis as in [38].

In the scope of this thesis, we apply the designed controllers to a physical plant in a real-time experimental setup, located at the *Universitetet i Agder* in Grimstad, Norway. The considered plant is a two-mass oscillator with non-collocated actuation and measurement. It consists of an active, i.e. controlled, mass and a hanging load that are connected with a spring. Only the position of the load is available for control, hence actuation and measurement are non-collocated. Such setup has high practical relevance, especially when the spring constant and masses are varying or unknown, e.g. in the case of load transportation on construction sites. Already in the early 90s, it has been used to formulate benchmark problems for robust controller design due to its universality [47]. An $\mathcal{H}_\infty$ control approach has been made e.g. by Chiang and Safonov [6]. In this work, we artificially inject a communication delay into the plant model in terms of an input time delay. An approximation of this delay using Padé-terms leads to non-minimum phase zeros that can be addressed using the above-mentioned procedure.

Before regarding the contribution and outline of the thesis in detail, the preliminary work on the cancellation strategy as well as the oscillator are briefly summarized.

1.1 Preliminary Work

There are only few publications on the partial cancellation of non-minimum phase zeros or unstable poles [22, 26, 27]. The derivations for a single non-minimum phase zero are part of [27]. The strategy is also applied to several examples, however only in a simulation setup and without comparable reference controllers (especially in terms of the finally implemented controller order). In [26] the proposed cancellation strategy is applied to models of flexible-link robots. Still, no direct comparison to different approaches is given and, to the best of the authors knowledge, the non-minimum phase zeros of the considered plants are not dominating. Finally, Mahani et al. [22] compare the performance of classical PI control with an extended controller that partially cancels the non-minimum phase zero of the plant.

The considered plant can be found in two publications [36, 37] so far. In the first publication [37], Ruderman proposes a robust output feedback controller that makes use of a notch filter and a delay-based compensator as a second degree of freedom to counteract disturbance- or uncertainty-caused oscillations. Furthermore, a detailed robustness analysis regarding parameter uncertainties is part of the article as well as simulation studies. The second article [36] proposes a frequency-estimation algorithm which proves to be globally convergent, robust against measurement noise and false initialization and only requires one design parameter.

1.2 Contribution and Outline of this Thesis

The necessary theoretical background to follow the considerations in this work is summarized in Chapter 2. It covers an introduction into fractional-order linear time-invariant systems and mentions typical fractional-order control approaches as well as their implementation. Furthermore, the basics of the $\mathcal{H}_\infty$ framework are discussed. As we consider a plant with an input delay, the chapter concludes with the frequency characteristics of the commonly used Padé-approximation.

The main contributions of this work can be divided into two categories. First, we extend the concept of partial pole-zero cancellation to a pair of conjugate complex zeros/poles in Chapter 3. Furthermore, implicit pseudo zeros/poles are included into the considerations and a closed-loop stability analysis is conducted. This chapter focuses on the frequency domain and recaptures the results presented in [45].

Second, we consider the two-mass oscillator itself. In Chapter 4, a detailed model of the plant is derived. It consists of a linear part used for the controller design, an experimentally identified nonlinearity at the input, a process noise model and the artificially injected input delay.
The proposed fractional-order terms are applied to the robust control of the plant with delay, using a two degree of freedom control structure. For comparability, a reference controller of similar order and frequency characteristics is designed based on the $\mathcal{H}_\infty$ framework. We consider controllers for two nominal time delays and compare the frequency responses in Chapter 5. These controllers are evaluated by means of simulations and experiments with regard to disturbance attenuation and tracking performance. Detailed discussions and illustrations are part of Chapter 6. The Chapters 4 to 6 contain results presented in [44].

We conclude this thesis with a summary of the main findings and give perspectives for future work in Chapter 7.

2 Theoretical Background

In this chapter we introduce and briefly discuss the most important concepts and preliminaries for the scope of this thesis. It consists of three parts. First, we consider the fundamentals of fractional-order systems in Section 2.1, i.e. the general definition of the fractional-order derivative as well as the concept of fractional-order transfer functions (with exemplary step responses) and stability. Furthermore, typical fractional-order PID-type controllers as well as their realization are discussed. The second part, Section 2.2, addresses the basics of $\mathcal{H}_\infty$ control including the definitions of the two most relevant norms. Finally, as one of the main motivations behind this thesis is the application to time-delay processes, we present the widely used Padé-approximations in the frequency domain.

2.1 Fundamentals of Fractional-Order Systems and Control

To describe fractional-order input-output behavior of a system, we first need to consider the very basics, i.e. the derivative of non-integer order and its Laplace transform. This allows analyzing fractional-order transfer functions and stability in terms of the pseudo pole locations in the complex plane. Furthermore, we describe the frequency response of fractional-order transfer functions and briefly present two typical controller structures. As the controller with non-integer order elements shall be implemented in a real-time experimental setup, different approximation methods are discussed at the end of this section.

2.1.1 The Fractional Derivative

We can generalize the derivative of integer-order $n \in \mathbb{N}$ to an operator of arbitrary order $\alpha \in \mathbb{R}_+$ with $\mathbb{R}_+ = \{x \in \mathbb{R} \mid x > 0\}$ in different ways. Detailed discussions and derivations are done e.g. by Podlubny [33]. Here, we shortly discuss two operators.

On the one hand, consider the Riemann-Liouville fractional derivative operator for the function $f(\cdot)$ which is bounded for $t_0 \leq t \leq t_\mathrm{f}$ given by [29, p. 11]

$$ {}^{\mathrm{R}}_{t_0}\mathcal{D}^{\alpha}_{t} f(t) = \frac{\mathrm{d}^n}{\mathrm{d}t^n} \left[\frac{1}{\Gamma(n-\alpha)} \int\limits_{t_0}^{t} \frac{f(\tau)}{(t-\tau)^{\alpha-n+1}} \mathrm{d}\tau \right] , \quad n-1 < \alpha < n \tag{2.1} $$

with the positive integer $n \in \mathbb{N}$, fractional order $\alpha \in \mathbb{R}_+$ and $\Gamma(\cdot)$ denoting Euler's Gamma function. On the other hand, if we restrict us to functions $f(\cdot)$ with an absolute integrable n-th order derivative $f^{(n)}(\cdot)$, the Caputo operator can be used. It is defined as [29, p. 11]

$$ {}_{t_0}\mathcal{D}_t^{\alpha} f(t) = \frac{1}{\Gamma(n-\alpha)} \int_{t_0}^{t} \frac{f^{(n)}(\tau)}{(t-\tau)^{\alpha-n+1}} \, \mathrm{d}\tau, \quad n-1 < \alpha < n \tag{2.2} $$

with $n \in \mathbb{N}$ and $\alpha \in \mathbb{R}_+$.

The Laplace transforms $\mathcal{L}\{\cdot\}(s)$ of the defined fractional-order derivatives are given by [29, p. 12]

$$ \mathcal{L}\left\{ {}_0^{\mathrm{R}}\mathcal{D}_t^{\alpha} f(t) \right\} = s^{\alpha} \mathcal{L}\{f(t)\} - \sum_{k=0}^{n-1} s^k \left[{}_0^{\mathrm{R}}\mathcal{D}_t^{\alpha-k-1} f(t) \right]_{t=0} \quad \text{and} \tag{2.3} $$

$$ \mathcal{L}\left\{ {}_0\mathcal{D}_t^{\alpha} f(t) \right\} = s^{\alpha} \mathcal{L}\{f(t)\} - \sum_{k=0}^{n-1} s^{\alpha-k-1} f^{(k)}(0) \tag{2.4} $$

with $n-1 < \alpha < n$. In contrast to the Riemann-Liouville definition in (2.1) and (2.3), the Caputo operator allows using the initial conditions of the integer-order derivatives. In the following, we use the short-hand $\mathcal{D}^{\alpha}$ for the fractional derivative of order α with $t_0 = 0$. As we consider zero initial conditions only, both operators can be applied.

2.1.2 Fractional-Order Systems

In order to describe the input-output behavior of fractional-order systems, we make use of fractional-order differential equations. Considering linear time-invariant (LTI) single-input single-output (SISO) systems of *commensurate* order $\alpha \in \mathbb{R}_+$ only, it can be described by [29, p. 17]

$$ \sum_{k=0}^{n} a_k \mathcal{D}^{k\alpha} y(t) = \sum_{k=0}^{m} b_k \mathcal{D}^{k\alpha} u(t) \tag{2.5} $$

with real coefficients $a_k, b_k \in \mathbb{R}$ and the continuous-time input $u(t)$ and output $y(t)$. Given a base order $\alpha \in \mathbb{Q}_+$ with $\mathbb{Q}_+ = \{x \in \mathbb{Q} \mid x > 0\}$, e.g. $\alpha = \nu^{-1}$, $\nu \in \mathbb{N}$, the system is of *rational* order.

Applying the Laplace transform to (2.5) for zero initial conditions leads to the fractional-order transfer function [29, p. 18]

$$G(s) = \frac{Y(s)}{U(s)} = \frac{\sum\limits_{k=0}^{m} b_k s^{\alpha k}}{\sum\limits_{k=0}^{n} a_k s^{\alpha k}} = \frac{B(s^\alpha)}{A(s^\alpha)} \tag{2.6}$$

with input and output Laplace transforms $\mathcal{L}\{u(t)\}(s)=U(s)$ and $\mathcal{L}\{y(t)\}(s)=Y(s)$. It can be seen as a pseudo-rational function in terms of $\lambda = s^\alpha$.

In the following, we call the solutions $p \in \mathbb{C}$ to $A(p) = 0$ *pseudo poles*, whereas all $z \in \mathbb{C}$ satisfying $B(z) = 0$ are termed *pseudo zeros*. The bounded-input bounded-output (BIBO) stability of a given commensurate fractional-order system can be classified in terms of the argument of its pseudo poles:

Theorem 1 (Stability of LTI Fractional-Order Systems [24]) *Consider the coprime fractional-order transfer function $G(s) = B(s^\alpha)/A(s^\alpha)$ in (2.6) of commensurate order α. $G(s)$ is BIBO stable if and only if*

$$|\arg(p)| > \alpha\frac{\pi}{2}$$

holds for all $p = s^\alpha$, $p \in \mathbb{C}$ with $A(p) = 0$.

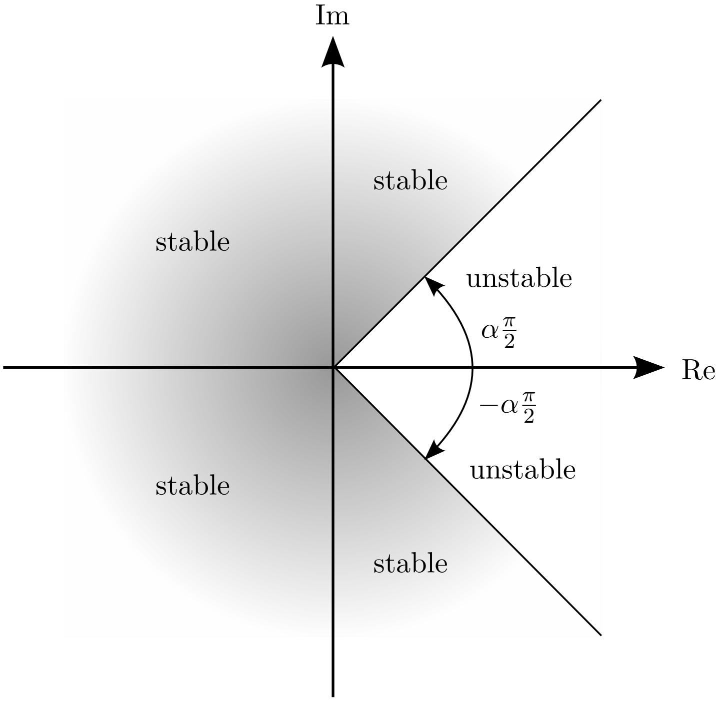

Figure 2.1: Schematic representation of the stability condition for systems of commensurate fractional-order $\alpha \in (0, 1]$.

Note that this condition can be extended to the integer-order case, as for $\alpha = 1$ the right-hand side coincides with the imaginary axis of the complex plane. An illustration of the stability condition is depicted in Figure 2.1, which also shows the enlargement of the stable region $\mathbb{C}_\alpha = \{x \in \mathbb{C} \,|\, |\arg(x)| > \alpha\frac{\pi}{2}\}$ for $\alpha \in (0, 1)$.

2.1.3 Time and Frequency Response of Fractional-Order Systems

To gain some insight into the behavior of fractional-order systems, we shortly discuss their time and frequency responses.

By utilizing the inverse Laplace transform $\mathcal{L}^{-1}\{\cdot\}(t)$ on $G(s)$ in its partial fraction expansion

$$G(s) = \sum_{k=0}^{n} \frac{r_k}{s^\alpha - p_k}, \tag{2.7}$$

the impulse response $g(t)$ and the step response $h(t)$ can be obtained as [29, p. 27]

$$g(t) = \sum_{k=0}^{n} r_k t^{\alpha-1} E_{\alpha,\alpha}(p_k t^\alpha) \quad \text{and} \tag{2.8}$$

$$h(t) = \sum_{k=0}^{n} r_k t^{\alpha} E_{\alpha,\alpha+1}(p_k t^\alpha). \tag{2.9}$$

The two-parameter Mittag-Leffler function $E_{\alpha,\beta}(\cdot)$ is given by [33, p. 17]

$$E_{\alpha,\beta}(z) = \sum_{k=0}^{\infty} \frac{z^k}{\Gamma(\alpha k + \beta)}, \quad \mathrm{Re}(\alpha) > 0, \mathrm{Re}(\beta) > 0 \tag{2.10}$$

which is a generalization of the exponential function. Detailed information on the Gamma function as well as the Mittag-Leffler function can be found in e.g. [29, 33]. In the scope of this work, we utilize integer-order approximations of the fractional derivative. Further discussions on exact solutions to fractional-order differential equations are therefore not part of it.

However, we make an exemplary graphical illustration. For this purpose, consider

$$G(s) = \frac{1}{(s^{0.25} - p)\,(s^{0.25} - \bar{p})} = \frac{1}{1 - 2|p|\cos(\varphi)s^{0.25} + |p|^2 s^{0.5}} \tag{2.11}$$

with $\alpha = 0.25$ and the conjugate complex pair of pseudo poles $p, \bar{p} \in \mathbb{C}$. Figure 2.2 illustrates the relationship between the argument φ_i of the pseudo poles $p_i = 1e^{\mathrm{j}\varphi_i}$ and the corresponding step responses. The time responses are calculated using the *FOMCON* toolbox in Matlab [41].

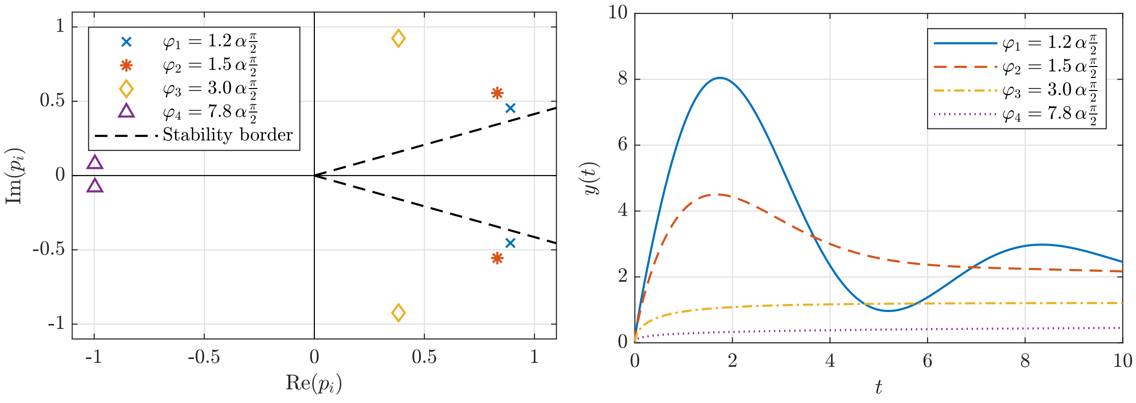

(a) Pseudo-poles p_i in the complex plane.

(b) Step responses.

Figure 2.2: Step responses of a fractional-order transfer function with a pair of conjugate complex pseudo poles $p_i, \bar{p}_i$ and its location in the complex plane.

Similar to the integer-order case, oscillations can be observed for pseudo poles close to the stability limit, e.g. p_1, p_2. More precisely, an oscillatory step response occurs whenever $\alpha\,\frac{\pi}{2} < |\varphi| < \alpha\,\pi$ and a monotonically decreasing response can be observed for $|\varphi| \geq \alpha\,\pi$ [29, p. 27]. For the latter case consider p_3 with $\varphi_3 = 3\,\alpha\,\frac{\pi}{2} > \alpha\,\pi$. In contrast to the integer-order case, the convergence for systems of non-integer order is *algebraic* only as $t \to \infty$, i.e. significantly slower than *exponential* convergence. Detailed discussions on the convergence of Mittag-Leffler-type functions can be found in [23].

Finally, we shortly summarize the asymptotic frequency response of LTI commensurate fractional-order systems given by [29, p. 29]

$$G(s) = \frac{\prod\limits_{k=0}^{m} (s^\alpha + z_k)}{\prod\limits_{k=0}^{n} (s^\alpha + p_k)}, \quad p_k \neq z_k, \tag{2.12}$$

since Bode-like plots can be obtained allowing intuitive controller tuning similar to the integer-order case. Each pseudo zero that is located in the stable region leads to a magnitude slope of $0\,\frac{\mathrm{dB}}{\mathrm{dec}}$ for low frequencies and $\alpha\,20\,\frac{\mathrm{dB}}{\mathrm{dec}}$ for high frequencies, whereas the phase start at 0° and tends to $\alpha\,90°$. Every stable pseudo pole yields the opposite, i.e. the magnitude slope tends to $-\alpha\,20\frac{\mathrm{dB}}{\mathrm{dec}}$ and the phase reaches $-\alpha\,90°$ [29, p. 29]. Note that the magnitude at the asymptote intersection frequency $\omega = |p_k|$ does not coincide with the integer-order case of $-3\,\mathrm{dB}$, i.e. the straight line approximation is worse for fractional-order systems around $\omega = |p_k|$.

Pseudo zeros and poles that are located in the unstable region are omitted here, as they are discussed in detail in the following chapter.

2.1.4 Fractional-Order PID-Type Controller

Various generalizations of integer-order control structures to non-integer orders can be found in the literature, cf. [5, 29–31, 35] and the references therein. To mention only two that are relevant in the scope of this thesis, consider first the classical and broadly used PID controller which can be generalized using the fractional derivative. Its Laplace transform for zero initial conditions is given by [29, p. 82]

$$C_{\mathrm{FOPID}}(s) = K_{\mathrm{p}} + \frac{K_{\mathrm{i}}}{s^{\mu}} + K_{\mathrm{d}} s^{\beta} \tag{2.13}$$

with $\beta, \mu \in (0, 1]$. By choosing $\beta = \mu = 1$ the integer-order PID controller is recovered. As the magnitude slope of s^{α} is $\alpha\, 20\, \frac{\mathrm{dB}}{\mathrm{dec}}$ and its phase $\alpha\, 90°$, this generalization obviously increases the degrees of freedom for the controller tuning.

Second, consider the fractional lead-lag compensator given by [31, 35]

$$C_{\mathrm{FOLL}}(s) = c_0 \left(\frac{1 + \frac{s}{\omega_{\mathrm{low}}}}{1 + \frac{s}{\omega_{\mathrm{high}}}} \right)^{\alpha}, \quad \alpha \in \mathbb{R} \tag{2.14}$$

where ω_{low} and ω_{high} denote the transitional frequencies and $c_0 > 0$ is the gain for low frequencies. This compensator may be used to stress a constant phase of the open loop over a frequency range Ω leading to a constant damping for loop gain variations, the so-called *iso-damping* property. An illustrative derivation and example can be found in [35].

2.1.5 Approximation of Fractional-Order Transfer-Functions

In this work we apply controllers with fractional-order elements to a physical system using real-time hardware in the laboratory setup. Consider the derivative operators of non-integer order in (2.1) and (2.2). The knowledge of the entire history of $f(t)$ is necessary in both cases, however the storage of the implementation hardware is obviously limited. Thus, the fractional-order derivative operator is approximated.

Depending on the application, various approximation methods are possible, see e.g. [29, 43, 48]. On the one hand, the Grünwald-Letnikov definition can be directly approximated and the *short memory principle* can be applied. This means that only the recent past is considered, i.e. $t \in [t - L, t]$ with positive constant L (size of the memory), since earlier time instants only have limited influence on the solution [29, p. 16].

On the other hand, we can approximate the frequency response of the fractional-order operator using integer-order terms. There are continued-fraction based methods, e.g. continued-fraction expansion, the Carlson filter or Matsuda-Fujii filter, that may involve the following problems [48, Chap. 5]:

- ◦ poor behavior in the frequency and/or time domain response,
- ◦ not specifiable range of approximation and
- ◦ no capability of retaining the original transfer functions stability.

If we consider the realization of a fractional-order controller, a good approximation fit in the crossover region as well as stability requirements are crucial. Therefore, these methods are not further discussed. Another possibility to approximate given frequency response data is utilizing the Matlab routine `invfreqs`, which is based on [20] and yields an analog filter least-squares optimal fit of a given order. However, the routine relies on, broadly speaking, matrix inversion and may lead to numerical issues.

Finally, consider the Oustaloup filter which approximates the fractional-order operator in the frequency range $\Omega = \{\omega \in \mathbb{R} \,|\, \omega_\mathrm{l} \leq \omega \leq \omega_\mathrm{h}\}$ by alternately placing integer-order poles and zeros. The resulting approximation of order $N_\mathrm{oust} = 2N + 1$ is given by [29]

$$s^\alpha \approx H_\alpha(s) = \omega_\mathrm{h}^\alpha \prod_{k=-N}^{N} \frac{s + \omega_k^-}{s + \omega_k^+} \tag{2.15a}$$

with

$$\omega_k^\pm = \omega_\mathrm{l} \left(\frac{\omega_\mathrm{h}}{\omega_\mathrm{l}}\right)^{\frac{k+N+(1\pm\alpha)/2}{2N+1}}, \quad \alpha \in (0,1). \tag{2.15b}$$

As all poles and zeros are located in $\mathbb{C}_-$, the open-loop controller design method is not affected.

2.2 Fundamentals of $\mathcal{H}_\infty$ Control

This section covers the main idea and basics of $\mathcal{H}_\infty$ control. First, we consider relevant norms of time-domain signals and transfer functions. Then, a special case of the linear fractional transformations is discussed and illustrated in Section 2.2.2 and, finally, we introduce the $\mathcal{H}_\infty$ synthesis problem in Section 2.2.3.

2.2.1 Norms of Signals and Systems

We shortly introduce and discuss the most relevant norms in the scope of this work, i.e. the $\mathcal{L}_2$ norm of a time signal w as a special case of $\mathcal{L}_p$ and the $\mathcal{H}_\infty$ norm of a proper and real-rational transfer function P. An overview of all relevant signal and system norms can be found in [9], whereas more detailed derivations and an introduction of the corresponding spaces are made by Zhou et al. [52, Chap. 4].

The $\mathcal{L}_2$ norm of a piecewise continuous signal $w = w(t)$, $t \in (-\infty, \infty)$ is defined as [9, p. 13]

$$\|w\|_2 := \sqrt{\int_{-\infty}^{\infty} w(t)^2 \mathrm{d}t}. \tag{2.16}$$

This definition also allows signals that start at $t = 0$, i.e. with $w(t) = 0 \; \forall \, t < 0$, and can easily be generalized to vector-valued signals, see e.g. [39, p. 536]. It can be interpreted as the total signal energy which becomes evident if we consider w as the current through a resistor of 1 ohm [9, p. 14].

Now consider the input-output behavior of a plant with transfer function P. If the input w is a disturbance, we naturally try to keep its impact on the output v as low as possible. The $\mathcal{H}_\infty$ norm of the scalar-valued, proper, real-rational transfer function P is defined as [9, p. 16]

$$\|P\|_\infty := \sup_\omega \left(P(j\omega)\right) \tag{2.17}$$

which can be generalized to transfer matrices using the maximum singular value of the transfer matrix $\bar{\sigma}(P(\mathrm{j}\omega))$ [39, p. 537]. Note that $\|P\|_\infty$ is finite if and only if P is proper and has no poles on the imaginary axis [9, p. 16]. Then, it is evident that $\|P\|_\infty$ equals the maximum amplitude in the corresponding Bode plot (or the maximum of the largest singular value). In order to estimate the impact of the input w on the output v, we may utilize the induced norm, i.e. the maximum system gain. In case of signals with finite energy, it can be shown that [9, p. 18]

$$\|P\|_\infty = \sup_{w \neq 0} \frac{\|v\|_2}{\|w\|_2} \tag{2.18}$$

for any $w \in \mathcal{L}_2$. Thus, if w is considered as a disturbance, we try to keep $\|P\|_\infty$ low, which can be interpreted as worst case description. It is therefore of special interest and may be used to measure system performance [9, p. 19].

2.2.2 Linear Fractional Transformations

We introduce a special case of linear fractional transformations that can be used to describe the input-output behavior of a connected system.

Consider the transfer matrix $P(s)$ which is partitioned as

$$P(s) = \begin{bmatrix} P_{11}(s) & P_{12}(s) \\ P_{21}(s) & P_{22}(s) \end{bmatrix}. \tag{2.19}$$

Figure 2.3 shows P in the standard $\mathcal{H}_\infty$ configuration, where w denotes the external input and v is termed performance output, u is the output of controller C and y is the controller input. The transfer matrix from w to v coincides with the lower linear fractional transformation with respect to C, defined as [52, p. 240]

$$\mathcal{F}_l(P, C) := P_{11} + P_{12}C_\infty \left(I - P_{22}C_\infty\right)^{-1} P_{21}, \tag{2.20}$$

provided that $\left(I - P_{22}C_\infty\right)^{-1}$ exists, with P and C of appropriate dimensions.

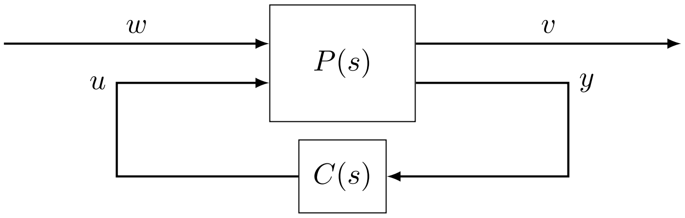

Figure 2.3: Standard $\mathcal{H}_\infty$ configuration.

Further detailed discussions on linear fractional transformations can be found e.g. in [52, Chap. 10].

2.2.3 $\mathcal{H}_\infty$ Synthesis

In this work, we make use of $\mathcal{H}_\infty$ controller synthesis methods to design a robust reference controller for the two-mass oscillator discussed in Chapter 4. The focus, however, is on the theoretical and practical investigation of partial pole-zero cancellation. Therefore, we only briefly discuss the main idea and a general approach of $\mathcal{H}_\infty$ controller design. Further information can be found in e.g. [12, 39, 52] and, with a focus on $\mathcal{H}_\infty$ control of time delay systems, see [19, 25, 28, 51].

Consider Figure 2.3 which shows the (generalized) plant P in standard $\mathcal{H}_\infty$ configuration. As mentioned above, if w is an external disturbance, we try to minimize its impact on the performance output v. In the scope of $\mathcal{H}_\infty$ control, we consider the signal energy $\|v\|_2$ that should be minimal for all external inputs with $\|w\|_2 \leq 1$. This is equivalent to the minimization of the $\mathcal{H}_\infty$ norm of the transfer function from w to v, i.e. [12, p. 37]

$$\min_{C \text{ stabilizing}} \|\mathcal{F}_l(P, C)\|_\infty =: \gamma_{\min}. \tag{2.21}$$

In case there is some knowledge about the disturbances, we may use it in terms of weight functions (typically high- or low-pass filters) [12, p. 37]. In a similar manner, weight functions can be used to fulfill design specifications and stress the desired closed-loop behavior. For this purpose, the plant is augmented with the weight functions W_i and thus incorporated into P. Standard procedures to find compromises between conflicting design specifications are e.g. the S/CS design. Here, the Sensitivity function S is addressed with low-pass filter W_1, which yields a small stationary error, and CS is weighted with W_2 to limit the bandwidth of the closed-loop system [39, p. 376].

In general the plant P is not scalar and thus the solution to the minimization problem in (2.21) is not unique [12, p. 39]. Instead of finding the controller C that minimizes the $\mathcal{H}_\infty$ norm, we consider a suboptimal solution, i.e.

$$\|\mathcal{F}_l(P, C)\|_\infty < \gamma \tag{2.22}$$

where $\gamma > 0$ is a positive number. Note that $\gamma > \gamma_{\min}$, but a γ-iteration algorithm can be used, e.g. bisection, to come arbitrarily close to the minimum. However, it can be observed that the solutions close to the optimum in terms of $\gamma_{\min}$ are numerically ill-conditioned [12, p. 39]. Therefore, in practice, a suboptimal controller C is usually employed [39, p. 376].

In order to find a solution to (2.22), two algebraic equations are to be solved. Necessary and sufficient conditions for the existence of a solution have been determined by Glover and Doyle [11]. Relaxed assumptions and the application to e.g. the S/CS design are discussed in [12]. An implementation of the described problem and its solution for a given generalized plant can be determined utilizing the Matlab routine `hinfsyn` based on [8, 11].

2.3 Time-Delay Approximations

It is well known that a time delay of length τ can be characterized in the frequency domain by [10]

$$G_{\mathrm{d}}(s) = e^{-\tau s}. \tag{2.23}$$

However, in the scope of classical $\mathcal{H}_\infty$ controller synthesis methods $G_{\mathrm{d}}(s)$ cannot be used directly, since it is of infinite dimension [52]. To overcome this problem, rational approximations of the exponential function are possible, e.g. by Taylor- or Padé-terms.

A standard procedure is to utilize the allpass Padé-appoximations [32] which do not affect the stability and have unity gain over all frequencies. As special cases consider the first- and second-order approximations given by [32, p. 16]

$$R_1(s) = \frac{2+\tau s}{2-\tau s} \quad \text{and} \tag{2.24a}$$

$$R_2(s) = \frac{12-6(\tau s)+(\tau s)^2}{12+6(\tau s)+(\tau s)^2}. \tag{2.24b}$$

It can be seen that the approximations consist of stable poles and non-minimum phase zeros, which is necessary to achieve allpass behavior. Thus, the first-order approximation R_1 yields a total phase lag of $-180°$ whereas R_2 leads to a negative phase of $-360°$. A phase plot of $G_{\mathrm{d}} = e^{-\tau\, s}$ with $\tau = 1$ opposite to its approximations R_j up to order four is depicted in Figure 2.4b . The locations in the complex plane of the corresponding poles and zeros are shown in Figure 2.4a. As expected, the poles and zeros are mirrored at the imaginary axis and all approximations of higher order ($j > 1$) involve a dominant pair of non-minimum phase zeros.

If we restrict the considerations to the frequency domain, the advantage of allpass approximations is evident. If a better time domain fit is prioritized in terms of the step response, however, Padé-approximations with order $j-1$ of the numerator (where j is the order of the denominator) may be more appropriate [10, p. 413f].

Having briefly discussed the most important preliminaries, we are prepared for the concept of partial pole-zero cancellation.

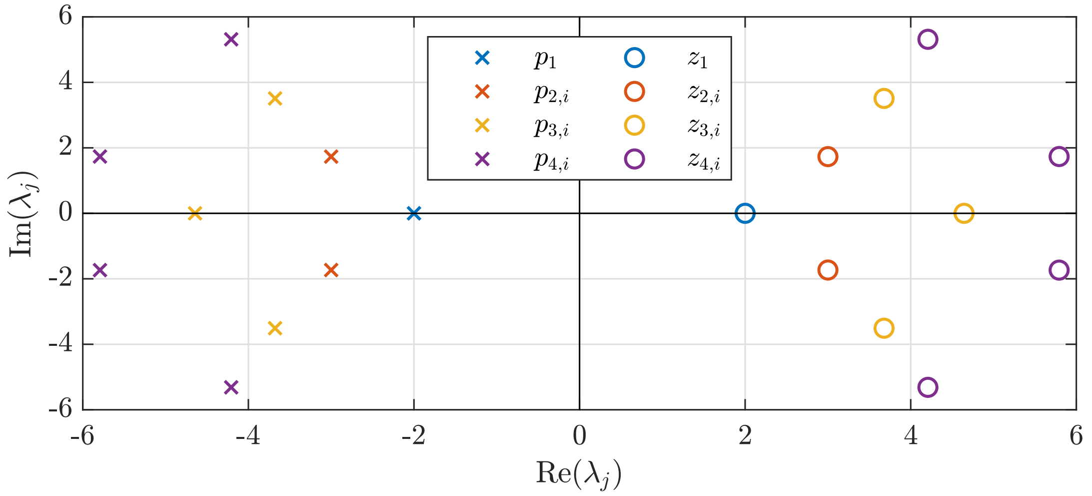

(a) Poles p_j and zeros z_j in the complex plane.

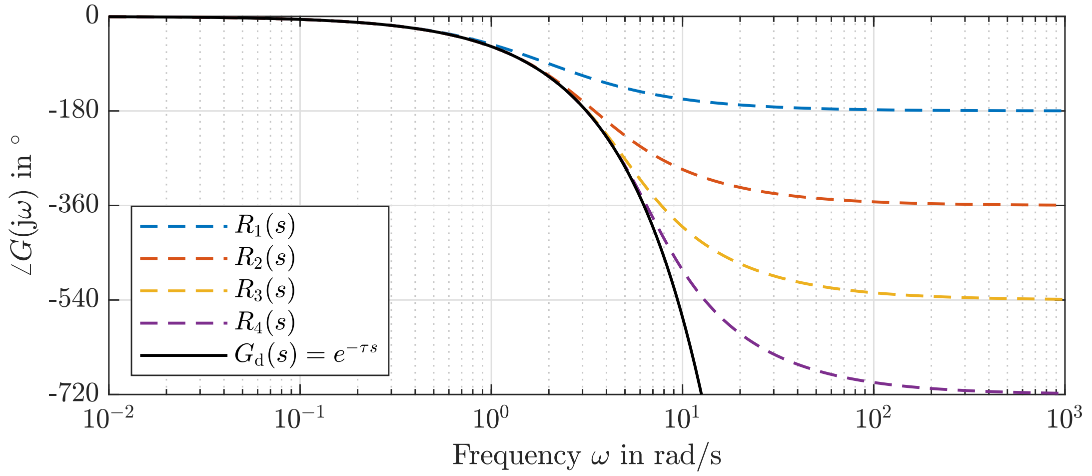

(b) Phase plot of the Padé-approximations $R_j(s)$ opposite to $G_\mathrm{d}(s) = e^{-\tau s}$.

Figure 2.4: Locations of the poles and zeros in the complex plane of the Padé-approximations of $G_\mathrm{d}(s) = e^{-\tau s}$ for $\tau = 1$ and their phase plots.

3 Partial Pole-Zero Cancellation

Partial pole-zero cancellation of non-minimum phase zeros can increase the robustness of the closed-loop system and reduce the undershoot of the step-response [22, 26, 27], therefore we investigate the frequency-domain behavior of fractional-order right-half plane poles and zeros in this section. This concept is extended to parts of the fractional-order lead-lag-element (implicit fractional-order zeros/poles) in Section 3.2 and a pair of conjugate complex pseudo zeros or poles in Section 3.3. Here, not only right-half plane zeros/poles are considered but also stable, low-damped poles since they significantly affect the stability margins of the control loop, too. Section 3.4 discusses the effect on the sensitivity functions of a standard control loop. To use the fractional-order elements in a real-time experimental setup, we utilize the Oustaloup recursive approximation that is presented in Section 3.5. The final section deals with an academic example to show the effect of the different cancellation strategies in the frequency-domain as well as in time-domain simulations.

Parts of this chapter have been submitted to an IFAC conference for possible publication [45].

3.1 Fractional-Order Pseudo Zeros and Poles

Consider the term in the Laplace domain

$$X_{z,\alpha}^{k}(s) = \left(1 - \left(\frac{s}{z}\right)^{\alpha}\right)^{k}, \quad s \in \mathbb{C},\ z \in \mathbb{C}_{+},\ \alpha \in (0,1],\ k \in \{-1, 1\} \tag{3.1}$$

where $\mathbb{C}_{+} = \{x \in \mathbb{C} \,|\, \mathrm{Re}(x) > 0\}$ is the set of right-half plane (RHP) complex numbers. Thus, $X_{z,\alpha}^{k}$ represents a right-half plane (RHP) zero for $k = 1$ and a pole for $k = -1$. As the exponent α is placed at the Laplace variable s directly, it is termed *explicit representation.*

In order to calculate the magnitude and phase of $X_{z,\alpha}^{k}(\mathrm{j}\omega)$, we make use of the polar coordinates $z = \omega_0 e^{\mathrm{j}\varphi}$ with absolute value $\omega_0 = |z|$ and argument $\varphi = \arg(z)$

leading to

$$\begin{aligned}
X^k_{z,\alpha}(\mathrm{j}\omega) &= \left(1-\left(\frac{\mathrm{j}\omega}{z}\right)^{\alpha}\right)^k \overset{z=\omega_0 e^{\mathrm{j}\varphi}}{=} \left(1-\left(\frac{\mathrm{j}\omega}{\omega_0 e^{\mathrm{j}\varphi}}\right)^{\alpha}\right)^k \overset{\mathrm{j}=e^{\mathrm{j}\frac{\pi}{2}}}{=} \left(1-\left(\frac{\omega e^{\mathrm{j}\frac{\pi}{2}}}{\omega_0 e^{\mathrm{j}\varphi}}\right)^{\alpha}\right)^k \\
&= \left(1-\left(\frac{\omega}{\omega_0}\right)^{\alpha} e^{\mathrm{j}\alpha\left(\frac{\pi}{2}-\varphi\right)}\right)^k \\
&= \left(1-\left(\frac{\omega}{\omega_0}\right)^{\alpha}\left[\cos\left(\alpha\left(\frac{\pi}{2}-\varphi\right)\right)+\mathrm{j}\sin\left(\alpha\left(\frac{\pi}{2}-\varphi\right)\right)\right]\right)^k .
\end{aligned}$$

With the abbreviation $\tilde{\varphi} := \frac{\pi}{2}-\varphi$ the magnitude turns out to be

$$\begin{aligned}
\left|X^k_{z,\alpha}(\mathrm{j}\omega)\right|^2 &= \left(1+\left(\frac{\omega}{\omega_0}\right)^{2\alpha}\left[\cos^2(\alpha\tilde{\varphi})+\sin^2(\alpha\tilde{\varphi})\right]-2\left(\frac{\omega}{\omega_0}\right)^{\alpha}\cos(\alpha\tilde{\varphi})\right)^k \\
&= \left(1+\left(\frac{\omega}{\omega_0}\right)^{2\alpha}-2\left(\frac{\omega}{\omega_0}\right)^{\alpha}\cos(\alpha\tilde{\varphi})\right)^k \qquad (3.2)
\end{aligned}$$

and the phase is given by

$$\angle X^k_{z,\alpha}(\mathrm{j}\omega) = k\ \arctan\left(\frac{-\left(\frac{\omega}{\omega_0}\right)^{\alpha}\sin(\alpha\tilde{\varphi})}{1-\left(\frac{\omega}{\omega_0}\right)^{\alpha}\cos(\alpha\tilde{\varphi})}\right). \qquad (3.3)$$

If we consider $z \in \mathbb{R}_+$ (i.e. $z \in \mathbb{R}$ and $\varphi = 0$), the magnitude and phase of $X^k_{z,\alpha}(\mathrm{j}\omega)$ are reduced to [27]:

$$\left|X^k_{z,\alpha}(\mathrm{j}\omega)\right|^2 = \left(1+\left(\frac{\omega}{z}\right)^{2\alpha}-2\left(\frac{\omega}{z}\right)^{\alpha}\cos\left(\frac{\pi\alpha}{2}\right)\right)^k, \qquad (3.4)$$

$$\angle X^k_{z,\alpha}(\mathrm{j}\omega) = k\arctan\left(\frac{-\left(\frac{\omega}{z}\right)^{\alpha}\sin\left(\frac{\pi\alpha}{2}\right)}{1-\left(\frac{\omega}{z}\right)^{\alpha}\cos\left(\frac{\pi\alpha}{2}\right)}\right). \qquad (3.5)$$

The discussions in this section are restricted to RHP pseudo zeros ($k = 1$). However, consider $k = -1$ in order to cover RHP pseudo poles.
Figure 3.1 shows the Bode plot of $X_{z,\alpha}$ for $z = 1$, $k = 1$ and $\alpha \in \{0.25,\ 0.5,\ 1\}$. For $k = -1$ see Figure A.1 in the appendix. To clearly identify integer-order zeros, we introduce the RHP zero

$$Z_1(s) = 1-\frac{s}{z}, \quad z > 0 \qquad (3.6)$$

which coincides with $X_{z,\alpha}(s)$ in (3.1) for $\alpha = 1$, i.e. $Z_1 = X_{z,1}$.

The asymptotic behavior of the magnitude and phase is summarized in Table 3.1. Considering high frequencies, a greater value of α leads to more magnitude slope,

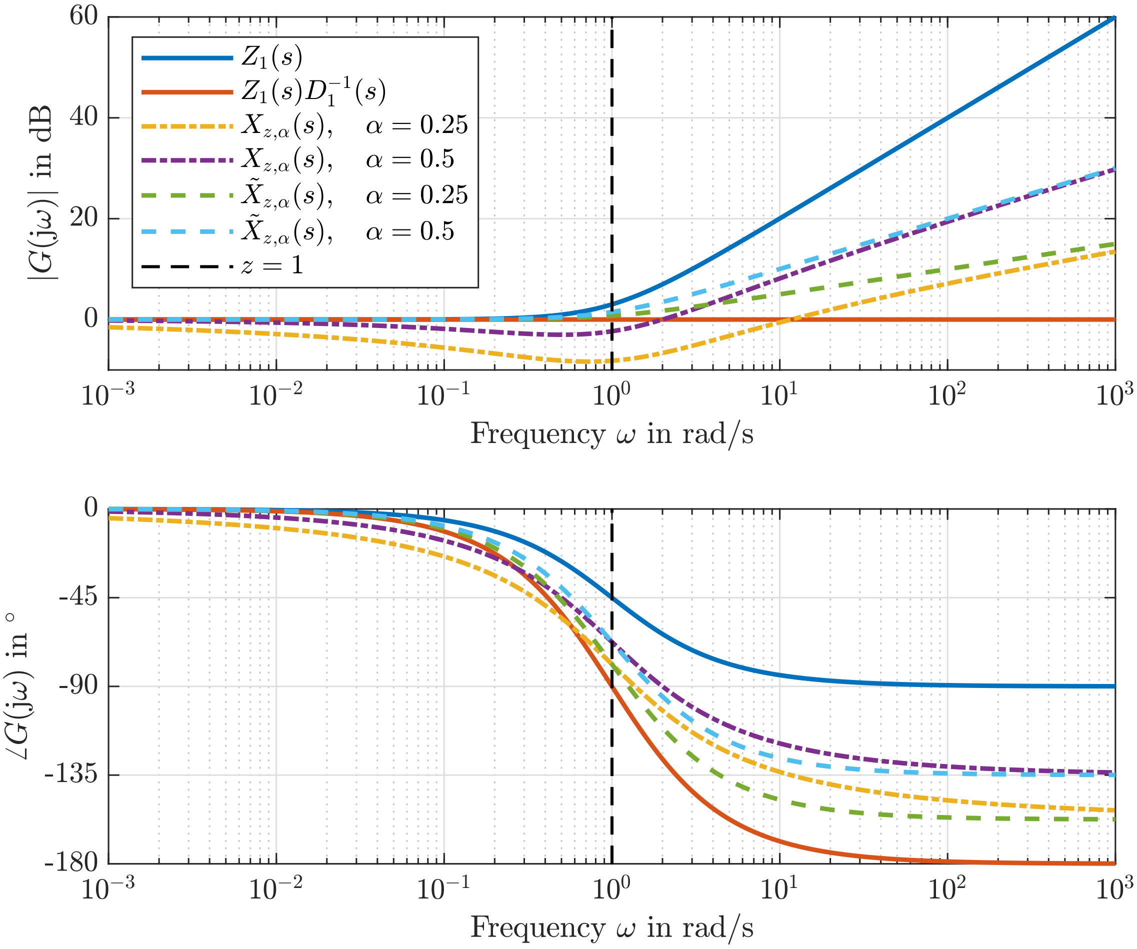

Figure 3.1: Bode plot of $X_{z,\alpha}$ and $\tilde{X}_{z,\alpha}$ for $z = 1$ and $\alpha \in \{0.25, 0.5\}$ opposite to the integer-order term Z_1 and its pseudo compensation $Z_1 D_1^{-1}$.

however less phase lag. The phase drop of $X_{z,\alpha}$ already occurs at lower frequencies in comparison with the integer-order term. Furthermore, the amplitude response of $X_{z,\alpha}$ shows a minimum at the frequency $\omega_{\min}$ that can be found by solving

$$\frac{\mathrm{d}}{\mathrm{d}\omega}\left|X^1_{z,\alpha}(\mathrm{j}\omega)\right|^2 = 0 \tag{3.7}$$

for ω. Then, the calculations for the magnitude are straight forward and those for the phase can be found in Appendix A.1.1 resulting in [27]

$$\omega_{\min} = z\left(\cos\left(\frac{\pi\alpha}{2}\right)\right)^{\frac{1}{\alpha}} \qquad \text{with} \tag{3.8}$$

$$\left|X^1_{z,\alpha}(\mathrm{j}\omega_{\min})\right| = \sin\left(\frac{\pi\alpha}{2}\right) \qquad \text{and} \tag{3.9}$$

$$\angle X^1_{z,\alpha}(\mathrm{j}\omega_{\min}) = \frac{\pi}{2}\left(\alpha - 1\right). \tag{3.10}$$

Regarding the behavior for $\alpha \to 0$, we can derive [27]:

$$\lim_{\alpha \to 0} \left(\omega_{\min}\right) = z, \tag{3.11}$$

$$\lim_{\alpha \to 0} \left(\left|X^1_{z,\alpha}(\mathrm{j}\omega_{\min})\right|\right) = 0 \mathrel{\hat{=}} -\infty\,\mathrm{dB} \quad \text{and} \tag{3.12}$$

$$\lim_{\alpha \to 0} \left(\angle X^1_{z,\alpha}(\mathrm{j}\omega_{\min})\right) = -\frac{\pi}{2}. \tag{3.13}$$

It can be seen that the magnitude lowers for a decrease in α and the phase approaches $-90°$.

Another interesting frequency to consider is $\omega = z$, where the magnitude and phase can be calculated as

$$\left|X^1_{z,\alpha}(\mathrm{j}\omega)\right|_z = \sqrt{2 - 2\cos\left(\frac{\pi\alpha}{2}\right)} = 2\sin\left(\frac{\pi\alpha}{4}\right) \quad \text{and} \tag{3.14}$$

$$\angle\, X^1_{z,\alpha}(\mathrm{j}\omega)\Big|_z = \arctan\left(\frac{-\sin\left(\frac{\pi\alpha}{2}\right)}{1 - \cos\left(\frac{\pi\alpha}{2}\right)}\right) = \frac{\pi}{2}\left(\frac{\alpha}{2} - 1\right). \tag{3.15}$$

The calculations to (3.14) and (3.15) are part of Appendix A.1.1. As expected, the phase lag at $\omega = z$ is half of the total phase lag, cf. Table 3.1. However, the magnitude is decreased compared to the integer-order case ($\alpha = 1$).

Consider a plant with an unstable pole or non-minimum phase zero at $z > 0$. Its integer-order transfer function may be given by

$$G_1(s) = \left(1 - \frac{s}{z}\right)^k \hat{G}_1(s) = Z^k_1(s)\hat{G}_1(s). \tag{3.16}$$

We can expand Z_1 to $\alpha^{-1} = \nu$, $\nu \in \mathbb{N}$ pseudo zeros [27], resulting in

$$Z^k_1(s) = \left(1 - \left(\frac{s}{z}\right)^{\frac{1}{\nu}}\right)^k \left(\sum_{n=1}^{\nu} \left(\frac{s}{z}\right)^{\frac{n-1}{\nu}}\right)^k = X^k_{z,\nu^{-1}}(s) Q^k_{z,\nu}(s) \tag{3.17}$$

with

$$Q^k_{z,\nu}(s) = \left(\sum_{n=1}^{\nu} \left(\frac{s}{z}\right)^{\frac{n-1}{\nu}}\right)^k. \tag{3.18}$$

It can be shown [27] that all $\nu - 1$ pseudo zeros of $Q_{z,\nu}(s)$ are stable, i.e. they are located in the region $\mathbb{C}_\alpha = \{z \in \mathbb{C} \mid |\arg(z)| > \alpha\frac{\pi}{2}\}$, depicted in Figure 3.3.

Hence we can use it for a partial cancellation of the plant's non-minimum phase zero

$$Z^k_1(s)\; Q^{-k}_{z,\nu}(s) = \left(1 - \left(\frac{s}{z}\right)^{\frac{1}{\nu}}\right)^k = X^k_{z,\nu^{-1}}(s). \tag{3.19}$$

For $k = 1$, this results in the above-discussed fractional-order pseudo zero. Utilizing the mirrored pole of $Z_1(s)$, i.e.

$$D_1^k(s) = \left(1 + \frac{s}{z}\right)^k, \tag{3.20}$$

yields the classical integer-order pseudo compensation of the RHP zero. It can be observed in Figure 3.1 that the partial cancellation preserves a steeper slope of the magnitude and a larger phase margin compared to the integer-order pseudo compensation.

Table 3.1: Frequency characteristics for the magnitude and the phase of (implicit) fractional-order pseudo zeros and pseudo poles. The red numbers indicate differences. Due to the limited relevance of the magnitude slope at $\omega = z$, it is denoted as '$*$'.

	Pseudo Zero			**Pseudo Pole**		
Frequency	$\omega \ll z$	$\omega = z$	$\omega \gg z$	$\omega \ll z$	$\omega = z$	$\omega \gg z$
$\lvert\cdot\rvert$	1	$2\sin\left(\frac{\pi\alpha}{4}\right)$	∞	1	$\left(2\sin\left(\frac{\pi\alpha}{4}\right)\right)^{-1}$	0
$\frac{\mathrm{d}}{\mathrm{d}\omega}\lvert\cdot\rvert$	$0\,\frac{\mathrm{dB}}{\mathrm{dec}}$	$*$	$20\,\alpha\,\frac{\mathrm{dB}}{\mathrm{dec}}$	$0\,\frac{\mathrm{dB}}{\mathrm{dec}}$	$*$	$-20\,\alpha\,\frac{\mathrm{dB}}{\mathrm{dec}}$
$\angle(\cdot)$	0	$\frac{\pi}{2}\left(\frac{\alpha}{2}-1\right)$	$\pi\left(\frac{\alpha}{2}-1\right)$	0	$\frac{\pi}{2}\left(1-\frac{\alpha}{2}\right)$	$\pi\left(1-\frac{\alpha}{2}\right)$
	Implicit Pseudo Zero			**Implicit Pseudo Pole**		
Frequency	$\omega \ll z$	$\omega = z$	$\omega \gg z$	$\omega \ll z$	$\omega = z$	$\omega \gg z$
$\lvert\cdot\rvert$	1	$\sqrt{2}^{\alpha}$	∞	1	$\sqrt{2}^{-\alpha}$	0
$\frac{\mathrm{d}}{\mathrm{d}\omega}\lvert\cdot\rvert$	$0\,\frac{\mathrm{dB}}{\mathrm{dec}}$	$*$	$20\,\alpha\,\frac{\mathrm{dB}}{\mathrm{dec}}$	$0\,\frac{\mathrm{dB}}{\mathrm{dec}}$	$*$	$-20\,\alpha\,\frac{\mathrm{dB}}{\mathrm{dec}}$
$\angle(\cdot)$	0	$\frac{\pi}{2}\left(\frac{\alpha}{2}-1\right)$	$\pi\left(\frac{\alpha}{2}-1\right)$	0	$\frac{\pi}{2}\left(1-\frac{\alpha}{2}\right)$	$\pi\left(1-\frac{\alpha}{2}\right)$

3.2 Implicit Fractional-Order Pseudo Zeros and Poles

In order to achieve a similar effect to the partial cancellation of the non-minimum phase zero in (3.19), we introduce the implicit term as a part of the fractional-order lead-lag element [29]

$$\tilde{Q}_{z,\nu}^k(s) = \left(1 + \frac{s}{z}\right)^{k\frac{\nu-1}{\nu}}, \quad z > 0,\ \nu \in \mathbb{N} \tag{3.21}$$

where the integer-order pseudo compensation is covered as an edge case, i.e.

$$\lim_{\nu\to\infty} \tilde{Q}_{z,\nu}^k(s) = D_1^k(s).$$

Applying $\tilde{Q}^k_{z,\nu}$ to the integer-order term Z_1^k yields

$$\tilde{X}^k_{z,\alpha}(s) = \left(1 - \frac{s}{z}\right)^k \tilde{Q}^{-k}_{z,\nu}(s), \quad z > 0,\ \alpha = \frac{1}{\nu}, k \in \{-1, 1\} \tag{3.22}$$

which is the implicit representation corresponding to (3.1). For calculating the magnitude and phase

$$\left|\tilde{X}^k_{z,\alpha}(\mathrm{j}\omega)\right| = \left(1 + \left(\frac{\omega}{z}\right)^2\right)^{k\frac{\alpha}{2}}, \tag{3.23}$$

$$\angle\tilde{X}^k_{z,\alpha}(\mathrm{j}\omega) = k \arctan\left(-\frac{\omega}{z}\right) - k(1-\alpha)\arctan\left(\frac{\omega}{z}\right), \tag{3.24}$$

we make use of the integer-order terms and rewrite the exponent of $\tilde{Q}^k_{z,\nu}$ for $\alpha = \nu^{-1}$, i.e. $(\nu - 1)\nu^{-1} = 1 - \alpha$. Note that we can generalize the definitions of $\tilde{Q}^k_{z,\nu}$ and $\tilde{X}^k_{z,\alpha}$ to $z \in \mathbb{C}_+$ in order to calculate the magnitude and phase given in Appendix A.1.2, which is necessary for later use. For now only $z \in \mathbb{R}_+$ are considered.

In following discussions we focus on implicit pseudo zeros ($k = 1$). However, consider $k = -1$ in order to cover implicit pseudo poles.

As it can be seen in Figure 3.1 and is summarized in Table 3.1, the frequency characteristics of the explicit and the implicit representations are very similar. An interesting frequency to consider is $\omega = z$, as the phase of the two representations in (3.5) and (3.24) coincides:

$$\angle X^k_{z,\alpha}(\mathrm{j}\omega)\Big|_z = \angle\tilde{X}^k_{z,\alpha}(\mathrm{j}\omega)\Big|_z = k\frac{\pi}{2}\left(\frac{\alpha}{2} - 1\right). \tag{3.25}$$

This does not apply to the magnitude. Consider the exemplary Bode plot in Figure 3.1 that show a magnitude drop of the explicit term around $\omega = z$ in contrast to the implicit representation which satisfies

$$\left|\tilde{X}^1_{z,\alpha}(\mathrm{j}\omega)\right|_z = \sqrt{2}^{\alpha} > 0\,\mathrm{dB} \quad \forall\alpha \in (0, 1].$$

In addition, the implicit representation leads to less phase lag for $\omega < z$ which is useful in the case of phase limitations. Therefore, $\tilde{Q}_{z,\nu}(s)$ is preferred to partially compensate a plant's non-minimum phase zero.

Note that the Bode plot analysis and observations are restricted to $z \in \mathbb{R}_{>0}$. Since the analysis of a single complex zero has limited practical relevance, it is omitted here.

3.3 Pair of Fractional-Order Conjugate Complex Pseudo Zeros or Poles

The practical relevance of unstable poles is evident, but also low-damped stable poles significantly affect the stability margins. Furthermore, it is worth considering a pair of non-minimum phase conjugate complex zeros since they arise e.g. due time delay approximations. More precisely, the Padé-approximation of a time delay involves a pair of dominant conjugate complex RHP zeros for approximation orders higher than one [10, 32]. In this section, we therefore consider such RHP zeros and poles in the beginning and discuss a pair of stable poles afterwards.

Following the representations of (3.1) to (3.5), given a RHP pair of conjugate complex pseudo zeros at

$$z = \omega_0 e^{\mathrm{j}\varphi}, \quad \bar{z} = \omega_0 e^{-\mathrm{j}\varphi} \in \mathbb{C}_+ \tag{3.26}$$

with $\omega_0 = |z|$ and $\varphi = \arg(z)$, we may derive

$$\begin{aligned} \mathcal{X}^k_{z,\alpha}(s) = X^k_{z,\alpha}\, X^k_{\bar{z},\alpha} &= \left(1 - \left(\frac{s}{\omega_0} e^{-\mathrm{j}\varphi}\right)^{\alpha}\right)^k \left(1 - \left(\frac{s}{\omega_0} e^{\mathrm{j}\varphi}\right)^{\alpha}\right)^k \\ &= \omega_0^{-2\alpha k} \left(s^{2\alpha} - 2\left(s\omega_0\right)^{\alpha} \cos\left(\varphi\alpha\right) + \omega_0^{2\alpha}\right)^k . \end{aligned} \tag{3.27}$$

For the detailed calculations see Appendix A.1.1.

Again, the integer-order case is covered by (3.27) for $\alpha = 1$, i.e.

$$Z^k_2(s) = \omega_0^{-2k} \left(s^2 - 2s\omega_0 \cos\left(\varphi\right) + \omega_0^2\right)^k . \tag{3.28}$$

Similar to (3.20), it can be pseudo compensated using the integer-order term

$$D^k_2(s) = \omega_0^{-2k} \left(s^2 + 2s\omega_0 \cos\left(\varphi\right) + \omega_0^2\right)^k . \tag{3.29}$$

For $z = 1e^{\mathrm{j}\frac{\pi}{3}}$, the Bode plot of $\mathcal{X}^{-1}_{z,\alpha}$ is shown in Figure 3.2 with $\alpha \in \{0.25,\, 0.5,\, 1\}$, i.e. a pair of pseudo poles. As expected, we can observe a maximum of the magnitude around $\omega = \omega_0$ and, in comparison with the integer-order pseudo compensation, more positive phase for lower frequencies. A summary of the frequency characteristics is given in Table 3.2. The Bode plot of $\mathcal{X}_{z,\alpha}$ (a pair of pseudo zeros) is shown in Figure A.2 in the appendix.

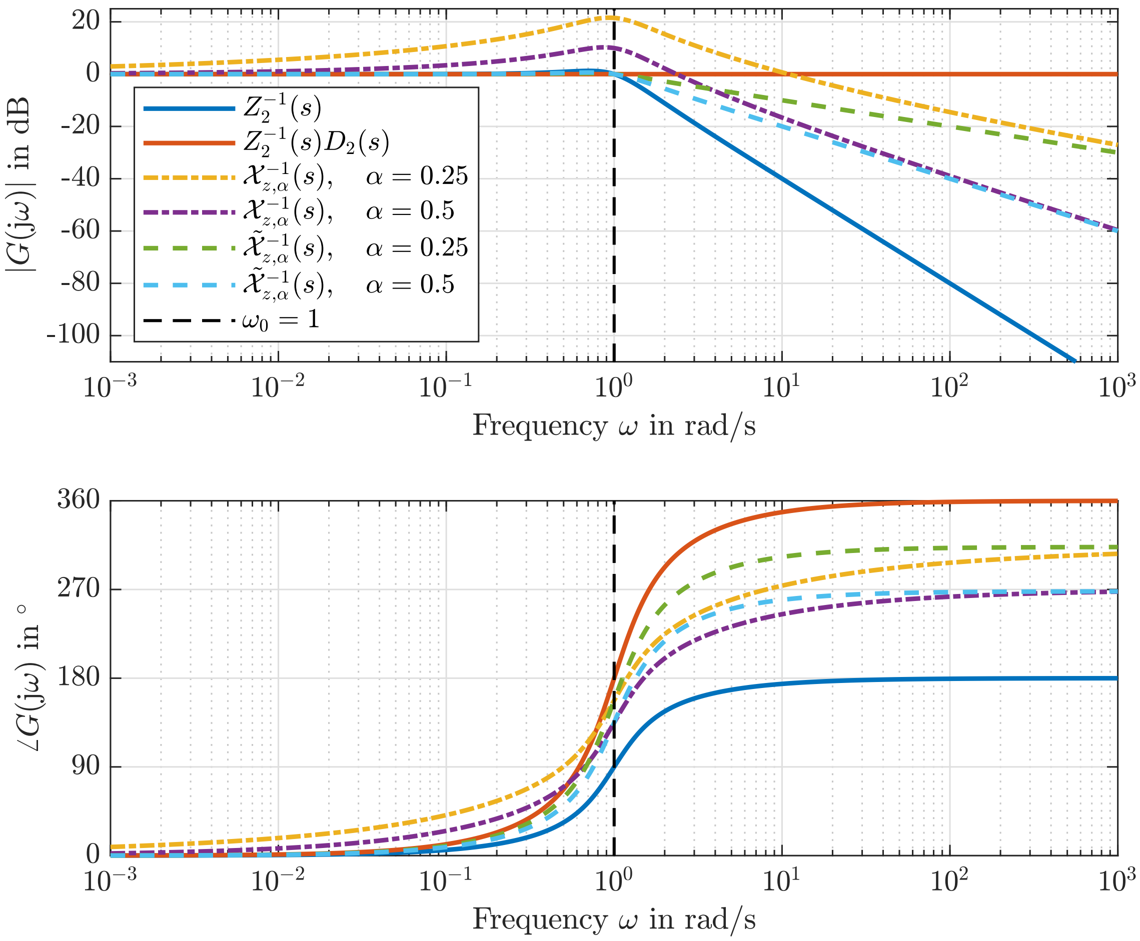

Figure 3.2: Bode plot of $\mathcal{X}_{z,\alpha}^{-1}$ and $\tilde{\mathcal{X}}_{z,\alpha}^{-1}$ for $z = 1e^{\mathrm{j}\frac{\pi}{3}}$ and $\alpha \in \{0.25, 0.5\}$ opposite to the integer-order term Z_2^{-1} and its pseudo compensation $Z_2^{-1}D_2$.

Given a plant with the transfer function

$$G_2(s) = Z_2^k(s)\hat{G}_2(s), \tag{3.30}$$

it involves a pair of RHP conjugate complex poles ($k = -1$) or zeros ($k = 1$). Since the expansion (3.17) holds for complex z as well, we reformulate (3.28) as

$$Z_2^k(s) = \left(1 - \frac{s}{z}\right)^k \left(1 - \frac{s}{\bar{z}}\right)^k. \tag{3.31}$$

Now, each term of Z_2^k can be expanded to ν pseudo zeros/poles (see (3.17)), where $X_{z,\nu^{-1}}^k$ and $Q_{z,\nu}^k$ have a conjugate complex part. As a result

$$\mathcal{Q}_{z,\nu}^k(s) = Q_{z,\nu}^k(s)\; Q_{\bar{z},\nu}^k(s) \tag{3.32}$$

has real coefficients.

Table 3.2: Asymptotic frequency characteristics of a pair of (implicit) fractional-order RHP conjugate complex pseudo zeros and poles.

	Pair of Pseudo Zeros		**Pair of Pseudo Poles**	
Frequency	$\omega \ll \omega_0$	$\omega \gg \omega_0$	$\omega \ll \omega_0$	$\omega \gg \omega_0$
$\frac{\mathrm{d}}{\mathrm{d}\omega}\lvert\cdot\rvert$ in $\frac{\mathrm{dB}}{\mathrm{dec}}$	0	$40\,\alpha$	0	$-40\,\alpha$
$\angle(\cdot)$ in $^\circ$	0	$-360+180\alpha$	0	$360-180\alpha$

In order to use $\mathcal{Q}^k_{z,\nu}$ for a partial cancellation, it is to be shown that $\mathcal{Q}^k_{z,\nu}$ only consist of stable pseudo zeros/poles. Without loss of generality, the discussions can be restricted to pseudo zeros ($k=1$). Since the terms of $\mathcal{Q}_{z,\nu}$ are conjugate complex, we restrict us to one term of (3.32) and its associated integer-order zero in (3.31). The remaining term can be discussed in a similar manner. We follow the reasoning of [45].

Consider $Q^1_{z,\nu}$ having ν pseudo zeros $\lambda_n = \sqrt[\nu]{z}$ with the arguments given by [4]

$$\arg\left(\lambda_n\right) = \varphi_n = \frac{\varphi + 2\pi n}{\nu}, \quad n = 0, 1, \ldots, \nu - 1. \tag{3.33}$$

It is evident that the angle between two consecutive roots is constant:

$$\Delta\varphi = \varphi_n - \varphi_{n-1} = \frac{2\pi}{\nu}. \tag{3.34}$$

We know from the expansion in (3.17) that the principal ν-th pseudo zero λ_0 of $\left(1 - \frac{s}{z}\right)$ is separated from the remaining λ_n, $n \geq 1$. Thus, the pseudo zeros of $Q_{z,\nu}$ have the arguments

$$\varphi_n = \frac{\varphi + 2\pi n}{\nu}, \qquad n = 1, 2 \ldots, \nu - 1. \tag{3.35}$$

As the complex roots of z are evenly distributed on a circle with radius $\sqrt[\nu]{|z|}$ around the origin of the complex plane, two critical cases are to be considered. These cases are illustrated in Figure 3.3, i.e. the roots λ_1 and $\lambda_{\nu-1}$ must not be located in the unstable region. Since we assume that z is located in the RHP, i.e.$|\varphi| < \frac{\pi}{2\nu}$, this condition is equivalent to

$$\Delta\varphi \overset{!}{>} \frac{\pi}{\nu}. \tag{3.36}$$

Knowing that $\Delta\varphi = \frac{2\pi}{\nu} > \frac{\pi}{\nu}$, see (3.34), condition (3.36) is satisfied. An analog discussion can be made for $k=-1$ (considering pseudo poles) and for the conjugate complex part $Q^k_{\bar{z},\nu}$. Thus, $\mathcal{Q}_{z,\nu}$ only consists of stable pseudo zeros.

Therefore, the fractional-order term $\mathcal{Q}^k_{z,\nu}$ can be used to partially cancel a pair of conjugate complex zeros/poles Z^k_2 without encountering stability issues.

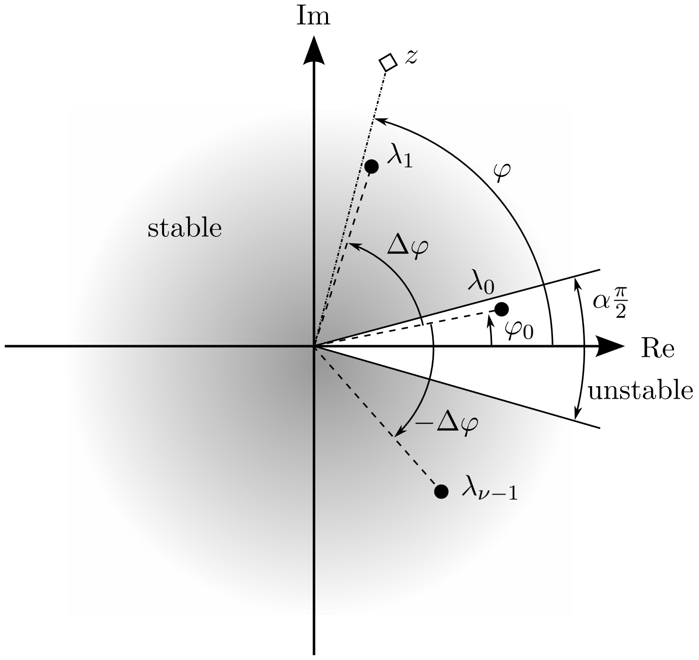

Figure 3.3: Schematic representation of the roots λ_i with argument φ_i of a RHP complex zero/pole z in the complex plane.

This yields

$$Z_2^k(s)\ \mathcal{Q}_{z,\nu}^{-k}(s) = \mathcal{X}_{z,\alpha}^k(s) \tag{3.37}$$

where $\mathcal{X}_{z,\alpha}^k$ consists of a lower-order pair of pseudo zeros/poles ($\alpha = \nu^{-1}$).

We can define the implicit counterparts of $\mathcal{X}_{z,\alpha}^k$ and $\mathcal{Q}_{z,\nu}^k$ for the pair of conjugate complex $z, \bar{z}$ of (3.26) and order $\alpha = \nu^{-1}$ in analogy to the case of a single real RHP zero/pole in (3.22) and (3.21). This yields

$$\tilde{\mathcal{Q}}_{z,\nu}^k(s) = \left(\frac{1}{\omega_0^2}\left(s^2 + 2s\omega_0\cos(\varphi) + \omega_0^2\right)\right)^{k\frac{\nu-1}{\nu}} \qquad \text{and} \tag{3.38}$$

$$\tilde{\mathcal{X}}_{z,\alpha}^k(s) = Z_2^k(s)\ \tilde{\mathcal{Q}}_{z,\nu}^{-k}(s) = \left(\omega_0^{2\alpha}\frac{s^2 - 2s\omega_0\cos(\varphi) + \omega_0^2}{\left(s^2 + 2s\omega_0\cos(\varphi) + \omega_0^2\right)^{1-\alpha}}\right)^k . \tag{3.39}$$

Following the analogy, the integer-order terms of $\tilde{\mathcal{X}}_{z,\alpha}^k(\mathrm{j}\omega)$ can be utilized to derive the magnitude and phase that are therefore omitted here. An exemplary Bode plot of $\tilde{\mathcal{X}}_{z,\alpha}^{-1}$ is shown in Figure 3.2, while Table 3.2 summarizes the frequency characteristics. As expected by the analogy and confirmed by Figure 3.2 and Table 3.2, the comparison of the explicit and implicit pair of pseudo zeros/poles leads to conclusions similar to the case of a single real RHP zero/pole. The most important observations are the differences of the magnitude around $\omega = \omega_0$ and the phase for $\omega < \omega_0$.

As mentioned above, it may be desirable to reduce the effect of a given plant's stable, however low-damped pair of poles. We thus consider the conjugate complex pole pair

$$p = \omega_0 e^{\mathrm{j}\varphi}, \quad \bar{p} = \omega_0 e^{-\mathrm{j}\varphi} \in \mathbb{C}_- \tag{3.40}$$

where $\mathbb{C}_- = \{z \in \mathbb{C} \mid \mathrm{Re}(z) < 0\}$. In order to subject the left-half plane (LHP) poles to a partial cancellation without introducing instability, it is necessary to show that all $\nu = \alpha^{-1}$, $\nu \in \mathbb{N}$ roots of p and $\bar{p}$ remain stable, by means of their location in the complex plane. This can be formulated as

$$|\arg(p)| > \frac{\pi}{2} \quad \overset{!}{\Longrightarrow} \quad p^{\alpha} \in \mathbb{C}_{\alpha},\ \alpha = \nu^{-1}. \tag{3.41}$$

If this condition holds, we may use any combination of the ν-th roots $\lambda_n = \sqrt[\nu]{p}$ and $\bar{\lambda}_n = \sqrt[\nu]{\bar{p}}$ to partially cancel the pair of poles (apart from the natural condition of choosing conjugate complex roots).

For this purpose, we rewrite (3.33) as

$$\begin{aligned} \arg\left(\lambda_n\right) &= \frac{\varphi + 2\pi n}{\nu} \\ \Longleftrightarrow \quad \nu \arg\left(\lambda_n\right) - 2\pi n &= \varphi, \quad n = 0, 1, \ldots, \nu - 1 \end{aligned} \tag{3.42}$$

and consider the absolute values in the next step. This restricts the range to $0 < |\arg(\lambda_n)| < \pi$ and yields

$$\nu \left|\arg\left(\lambda_n\right)\right| \geq |\varphi| \quad \Longleftrightarrow \quad \left|\arg\left(\lambda_n\right)\right| \geq \frac{|\varphi|}{\nu}. \tag{3.43}$$

Knowing that $p \in \mathbb{C}_-$, i.e. $|\varphi| > \pi/2$, it directly follows

$$|\arg(p)| = |\varphi| > \frac{\pi}{2} \quad \Longrightarrow \quad \left|\arg\left(\lambda_n\right)\right| > \frac{\pi}{2\nu} = \alpha\frac{\pi}{2} \tag{3.44}$$

which proves implication (3.41).

Therefore, any pair of roots of the conjugate complex poles may be cancelled. Recall the relationship between the location of pseudo poles and the corresponding step responses in Section 2.1.3. As illustrated, an oscillatory step response is obtained for stable pseudo poles with $|\arg(\lambda)| < \frac{\pi}{\nu}$. In the present case, this concerns the principal ν-th roots

$$\lambda_0 = \sqrt[\nu]{\omega_0}\, e^{\mathrm{j}\frac{\varphi}{\nu}} \quad \text{and} \quad \bar{\lambda}_0 = \sqrt[\nu]{\omega_0}\, e^{-\mathrm{j}\frac{\varphi}{\nu}}. \tag{3.45}$$

Therefore, we may use the term

$$\mathcal{X}_{p,\alpha}(s) = \left(1-\left(\frac{s}{p}\right)^{\alpha}\right)\left(1-\left(\frac{s}{\bar{p}}\right)^{\alpha}\right) = \frac{1}{\omega_0^{2\alpha}}\left(s^{2\alpha} - 2\left(s\omega_0\right)^{\alpha}\cos\left(\varphi\alpha\right) + \omega_0^{2\alpha}\right) \tag{3.46}$$

with $\alpha = \nu^{-1}$ to cancel the principal roots, i.e. the pseudo poles closest to the stability border. Note that, for $z = p$, the term $\mathcal{X}_{p,\alpha}$ coincides with $\mathcal{X}_{z,\alpha}$ of (3.27). Applying $\mathcal{X}_{p,\alpha}$ to a plant with a pair of stable poles $p, \bar{p} \in \mathbb{C}_-$ yields

$$G_3 = \omega_0^2\left(s^2 - 2s\omega_0\cos\left(\varphi\right) + \omega_0^2\right)^{-1}\hat{G}_3(s) = P_2(s)\hat{G}_3(s) \quad \text{and} \tag{3.47}$$

$$P_2(s)\mathcal{X}_{p,\alpha}(s) = \mathcal{Q}_{p,\nu}(s). \tag{3.48}$$

In the same analogy, for $z = p$, the term $\mathcal{Q}_{p,\nu}$ equals $\mathcal{Q}_{z,\nu}$ of (3.32). Figure 3.4 holds a Bode plot of $\mathcal{Q}_{p,\nu}$ for $p = -1e^{\mathrm{j}\frac{9\pi}{20}}$ and $\nu \in \{2, 4\}$. The effect of the partial cancellation is obvious in the Bode plot. As discussed above, we expect a non-oscillating step response, which is confirmed by Figure 3.5. It shows the step response of $\mathcal{Q}_{p,\nu}$ for $\nu \in \{2, 4\}$ opposite to the integer-order case.

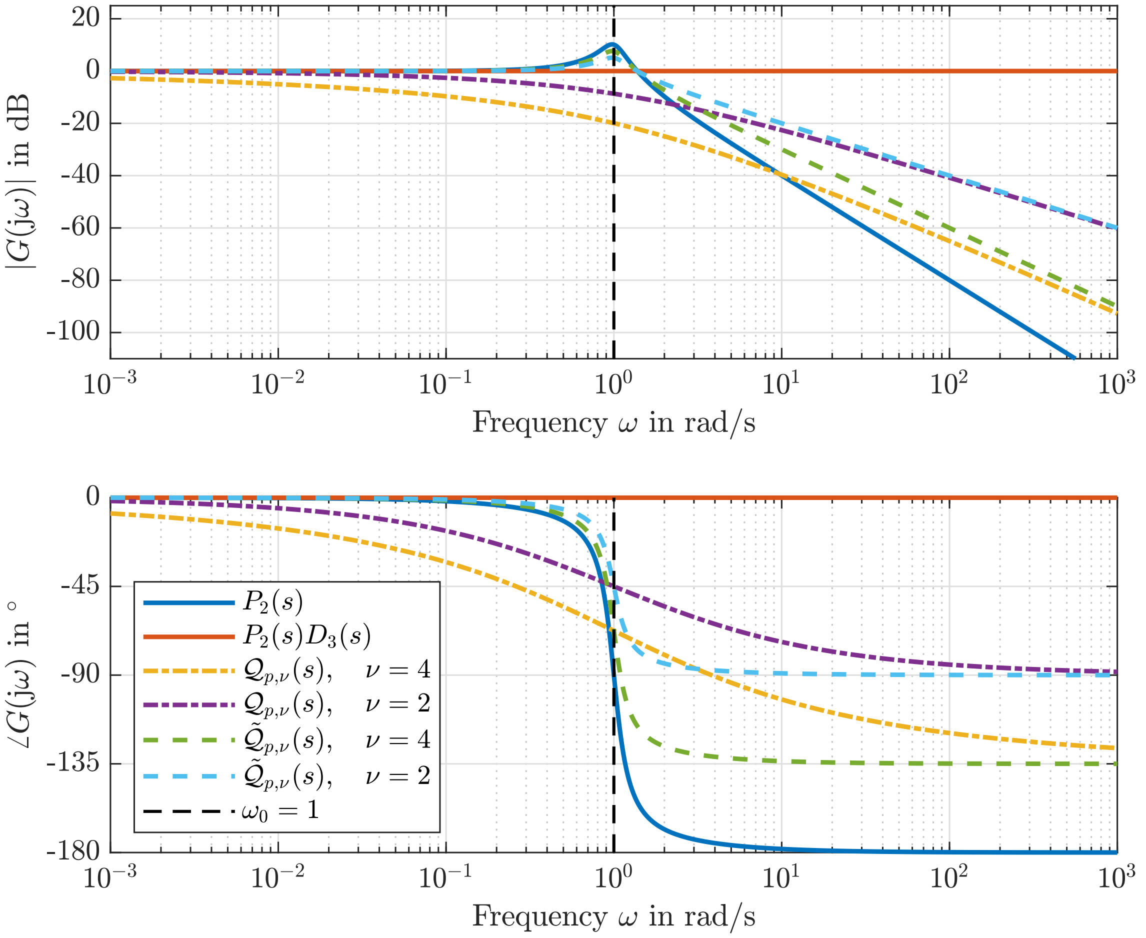

Figure 3.4: Bode plot of $\mathcal{Q}_{p,\nu}$ and $\tilde{\mathcal{Q}}_{p,\nu}$ for $p = -1e^{\mathrm{j}\frac{9\pi}{20}}$ and $\nu \in \{2, 4\}$ opposite to the integer-order term P_2 and its compensation P_2D_3 with $D_3 = P_2^{-1}$.

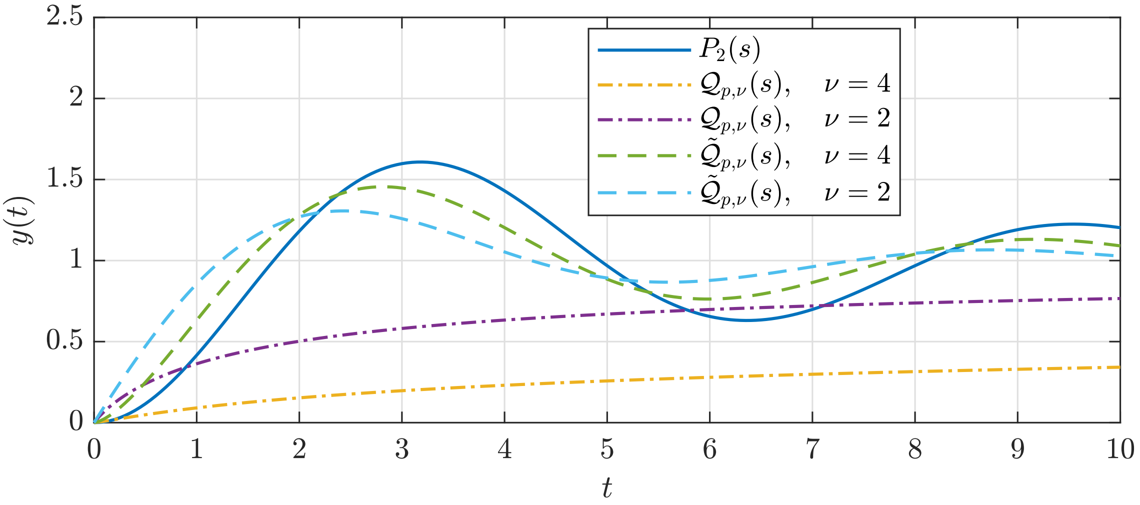

Figure 3.5: Step response of $\mathcal{Q}_{p,\nu}$ and $\tilde{\mathcal{Q}}_{p,\nu}$ for $p = -1e^{\mathrm{j}\frac{9\pi}{20}}$ and $\nu \in \{2, 4\}$ opposite to the integer-order term P_2.

The implicit counterpart of (3.48) for $\alpha = \nu^{-1}$ reads

$$\tilde{\mathcal{X}}_{p,\alpha}(s) = \omega_0^{-2\alpha} \left(s^2 - 2s\omega_0 \cos(\varphi) + \omega_0^2\right)^{\alpha} = P_2^{-\alpha}(s), \tag{3.49}$$

$$\tilde{\mathcal{Q}}_{p,\nu}(s) = P_2(s)\tilde{\mathcal{X}}_{p,\alpha}(s) = P_2^{\frac{1-\nu}{\nu}}(s). \tag{3.50}$$

Analog to the previous considerations, the Bode plot, depicted in Figure 3.4 on the next page, shows the similarities of the different representations for high and low frequencies. Significant differences can be observed around $\omega = \omega_0$, where the explicit representation erases the magnitude peak, hence the oscillatory part. The implicit compensation only reduces the peak (and oscillations, see Figure 3.5 on the next page). Again, the phase lag of the explicit cancellation largely exceeds the negative phase of the implicit counterpart for $\omega < \omega_0$.

In the following section, the effect of partial pole-zero cancellation on the closed-loop stability is analyzed.

3.4 Application to the Standard Control-Loop

Consider the standard SISO control-loop depicted in Figure 3.6, where $G(s)$ and $C(s)$ denote the plant and controller, respectively. The signals are the reference $r(t)$, the control error $e(t) = r(t) - y(t)$, control signal $u(t)$, output $y(t)$ as well as the input disturbance $d_u(t)$ and output disturbance $d_y(t)$.

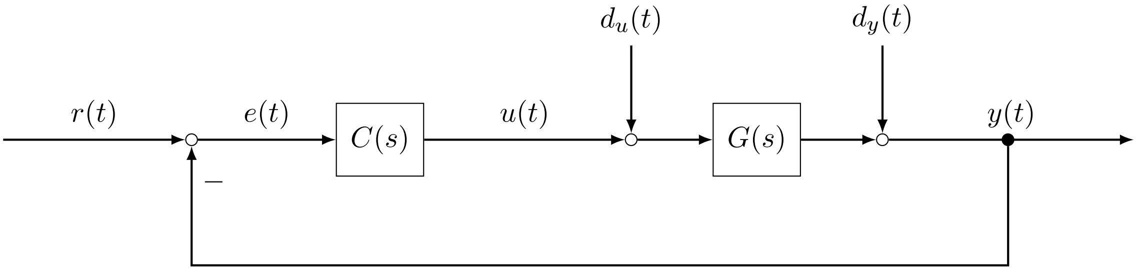

Figure 3.6: Standard control-loop.

According to Figure 3.6, we denote the complementary, output and input sensitivity functions as

$$T(s) = \frac{G(s)C(s)}{1 + G(s)C(s)}, \tag{3.51}$$

$$S_y(s) = \frac{1}{1 + G(s)C(s)} \quad \text{and} \tag{3.52}$$

$$S_u(s) = \frac{G(s)}{1 + G(s)C(s)}. \tag{3.53}$$

In order to investigate the discussed partial pole/zero cancellation, we partition the plant and controller into

$$G(s) = Z_i^k(s)\hat{G}(s) \quad \text{and} \quad C(s) = Q_i^{-k}(s)\hat{C}(s) \tag{3.54}$$

with $i \in \{1, 2\}$, $k \in \{-1, 1\}$ and

$$Z_i^k(s) = X_i^k(s)Q_i^k(s) \tag{3.55}$$

with

$$X_i^k(s) = \prod_{m=1}^{i} X_{z,\alpha}^k(s) \quad \text{and} \quad Q_i^k(s) = \prod_{m=1}^{i} Q_{z,\nu}^k(s).$$

This means, a RHP $z \in \mathbb{R}_+$ is considered for $i = 1$, cf. (3.1) and (3.16). On the other hand, $i = 2$ yields $z, \bar{z} \in \mathbb{C}_+$, see (3.27) and (3.32). It is assumed that Z_i^k contains all RHP poles/transfer zeros of G. Including the partitions for the plant and controller of (3.54) into the sensitivity functions yields

$$T = \frac{Z_i^k \hat{G} Q_i^{-k} \hat{C}}{1 + Z_i^k \hat{G} Q_i^{-k} \hat{C}} \overset{Z_i^k = X_i^k Q_i^k}{=} \frac{X_i^k \hat{G}\hat{C}}{1 + X_i^k \hat{G}\hat{C}} = \frac{\hat{G}\hat{C}}{X_i^{-k} + \hat{G}\hat{C}}, \tag{3.56}$$

$$S_y = \frac{1}{1 + Z_i^k \hat{G} Q_i^{-k} \hat{C}} = \frac{1}{1 + X_i^k \hat{G}\hat{C}} \quad \text{and} \tag{3.57}$$

$$S_u = \frac{Z_i^k \hat{G}}{1 + Z_i^k \hat{G} Q_i^{-k} \hat{C}} = \frac{X_i^k Q_i^k \hat{G}}{1 + X_i^k \hat{G}\hat{C}} = \frac{Q_i^k \hat{G}}{X_i^{-k} + \hat{G}\hat{C}} \tag{3.58}$$

where we omit the variable 's' for clarity reasons. Note that $Z_i^k = X_i^k Q_i^k$ contains all RHP poles/zeros, however all roots of Q_i^k are stable. We can thus conclude: the control loop is internally stable if the fractional-order pseudo polynomial $X_i^{-k} + \hat{G}\hat{C}$ has the roots in the stable region $\mathbb{C}_\alpha$. Note that these roots coincide with the pseudo poles of S_y in (3.57). This conclusion holds for the partial cancellation of stable conjugate complex poles as well, since $\mathcal{X}_{p,\alpha}$ only has stable roots. As it is discussed in Section 2.1.5, the integer-order Oustaloup approximation of fractional-order terms only consist of poles in $\mathbb{C}_-$, therefore the same results can be achieved for the implicit representations $\tilde{Q}_i^k$ and $\tilde{X}_i^k$.

Now, we show the difference between the fractional-order partial cancellation of an unstable pole and the integer-order unstable pole-zero cancellation. Therefore, setting $k = -1$ and $i = 1$ results in the plant $G = Z_1^{-1}\hat{G}$ containing one unstable pole $z \in \mathbb{R}_+$. Thus we have for the integer-order cancellation $C_{\mathrm{IO}} = Z_1 \hat{C}_{\mathrm{IO}}$, which yields

$$T_{\mathrm{IO}} = \frac{Z_1^{-1} \hat{G} Z_1 \hat{C}}{1 + Z_1^{-1} \hat{G} Z_1 \hat{C}} = \frac{\hat{G}\hat{C}}{1 + \hat{G}\hat{C}} \quad \text{and}$$

$$S_{u,\mathrm{IO}} = \frac{Z_1^{-1} \hat{G}}{1 + Z_1^{-1} \hat{G} Z_1 \hat{C}} = \frac{\hat{G}}{Z_1 \left(1 + \hat{G}\hat{C}\right)}.$$

Obviously, although the unstable pole is not part of T_{IO}, the input disturbance sensitivity $S_{u,\mathrm{IO}}$ is unstable. In contrast, considering the partial cancellation, we get

$$T = \frac{\hat{G}\hat{C}}{X_{z,\alpha} + \hat{G}\hat{C}} \quad \text{and}$$

$$S_u = \frac{Q_{z,\nu}^{-1} \hat{G}}{X_{z,\alpha} + \hat{G}\hat{C}} = \frac{\hat{G}}{Q_{z,\nu} \left(X_{z,\alpha} + \hat{G}\hat{C}\right)}.$$

This implies that S_u is stable if and only if T is stable which is in accordance with the relation above.

Note that fractional-order *unstable* partial pole-zero cancellation leads to the same issues as integer-order unstable pole-zero cancellation discussed above, i.e. if we use X_i^{-k} instead of Q_i^{-k} to partially cancel the RHP zero/pole. This becomes evident when considering (3.56) to (3.58) and exchanging X_i^k for Q_i^k. Regarding an unstable pole as before, it leads to e.g.

$$\begin{aligned} T &= \frac{\hat{G}\hat{C}}{Q_{z,\nu} + \hat{G}\hat{C}} \quad \text{and} \\ S_u &= \frac{\hat{G}}{X_{z,\alpha}\left(Q_{z,\nu} + \hat{G}\hat{C}\right)}. \end{aligned}$$

Thus, even if T is stable, S_u contains an unstable pseudo pole.

3.5 Implementation

Having discussed the different fractional-order terms in detail as well as the application to a standard control loop, we now come to the implementation. Recall that the fractional derivative operator needs to be approximated and, for this purpose, different approximation methods are possible, see Section 2.1.5. In this work we use the Oustaloup filter (2.15). This classical Oustaloup approximation method may lead to an erroneous stationary gain, consider for example

$$Q_{z,\alpha}^{-1}(s) = \frac{1}{1 - \left(\frac{s}{z}\right)^{\alpha}} \quad \xrightarrow{s \to 0} \quad 1. \tag{3.59}$$

In contrast, the proposed approximation leads to

$$Q_{z,\alpha}^{-1}(s) \approx \frac{1}{1 - \frac{H_\alpha(s)}{z^\alpha}} \quad \xrightarrow{s \to 0} \quad \frac{1}{1 - \left(\frac{\omega_l}{z}\right)^{\alpha}} \neq 1 \quad \text{for } \omega_l > 0. \tag{3.60}$$

To overcome this problem, we introduce an additional integrator like in e.g. [15, 46], which yields

$$s^{-\alpha} = \frac{s^{1-\alpha}}{s} \approx \frac{H_{1-\alpha}(s)}{s}. \tag{3.61}$$

For the example above, this results in

$$Q_{z,\alpha}^{-1}(s) = \frac{s^{-\alpha}}{s^{-\alpha} - \frac{1}{z^\alpha}} \approx \frac{H_{1-\alpha}(s)}{H_{1-\alpha}(s) + \frac{s}{z^\alpha}} \quad \xrightarrow{s \to 0} \quad 1 \tag{3.62}$$

and the correct stationary gain is recovered.

For the implicit terms, the substitution $\tilde{s} = 1 - \frac{s}{z}$ can be utilized [31] leading to

$$\tilde{Q}^{-1}_{z,\alpha}(s) = \left(1 - \frac{s}{z}\right)^{-\alpha} = \tilde{s}^{-\alpha} \approx \frac{H_{1-\alpha}(\tilde{s})}{\tilde{s}} = \frac{H_{1-\alpha}\left(1 - \frac{s}{z}\right)}{1 - \frac{s}{z}}. \tag{3.63}$$

In order to approximate the implicit second-order terms $\tilde{\mathcal{Q}}_{z,\alpha}$ and $\tilde{\mathcal{X}}_{p,\alpha}$, we would naturally use the substitution $s' = s^2 - 2sr\cos(\varphi) + r^2$. However, acceptable results can only be achieved if we address each conjugate complex root of p and $\bar{p}$ (cf. (3.40)) separately, leading to the conjugate complex approximations $H_{1-\alpha}(\tilde{s}_1)$ and $H_{1-\alpha}(\tilde{s}_2)$:

$$\begin{aligned}\tilde{\mathcal{X}}_{p,\alpha} = \left(1 - \frac{s}{p}\right)^{\alpha}\left(1 - \frac{s}{\bar{p}}\right)^{\alpha} &\underset{\tilde{s}_i := 1 - s/p_i}{=} \tilde{s}_1^{\alpha}\tilde{s}_2^{\alpha} \\ &\approx \frac{\tilde{s}_1\tilde{s}_2}{H_{1-\alpha}(\tilde{s}_1)H_{1-\alpha}(\tilde{s}_2)}.\end{aligned}$$

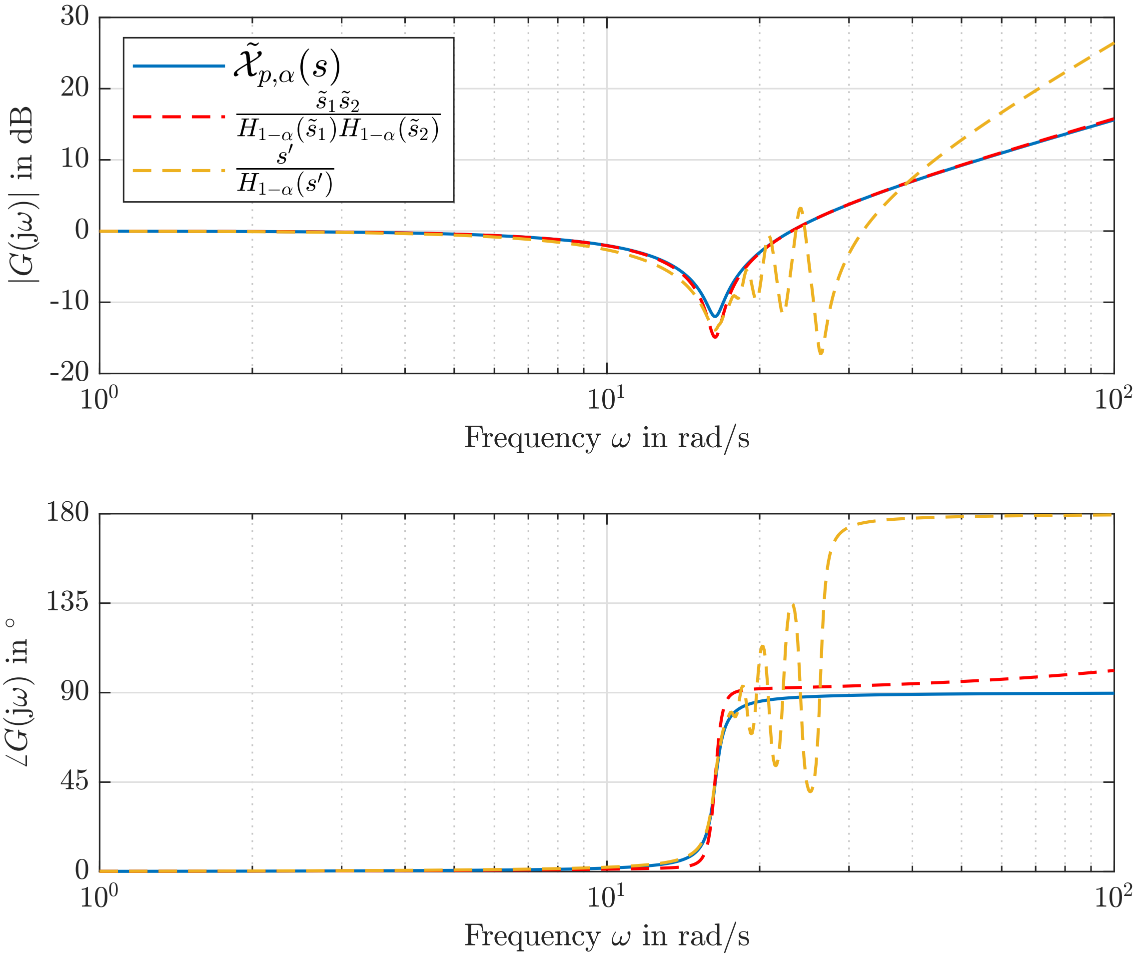

Figure 3.7: Oustaloup approximations of the implicit term $\tilde{\mathcal{X}}_{p,\alpha}$ with $p = -0.514 + \mathrm{j}16.346$, $\alpha = 0.5$ in the frequency range $[\omega_\mathrm{l}, \omega_\mathrm{h}] = [0.5\,\frac{\mathrm{rad}}{\mathrm{s}}, 500\,\frac{\mathrm{rad}}{\mathrm{s}}]$ with $N = 5$.

Figure 3.7 holds an exemplary Bode plot showing the differences of the two approaches. Note that the imaginary part of the complex coefficients of $H_{1-\alpha}(\tilde{s}_1)$ vanishes with $H_{1-\alpha}(\tilde{s}_2)$ leading to an overall approximation with real coefficients only.

3.6 Illustrative Example

In order to illustrate the theoretical results, we consider the transfer function

$$G(s) = \frac{(s-1)}{(1+\frac{s}{2})(1+\frac{s}{3})} \tag{3.64}$$

of a plant that contains a dominant non-minimum phase zero at $z = 1$. Thus we expect a significant undershoot in the step response.

To compare the different compensation and cancellation strategies, four controllers are designed that all consist of classical PI control with time constant $\tau = 2$, but variable proportional gain k_i:

$$\begin{aligned} C_1(s) &= k_1 \frac{\tau s + 1}{\tau s}, & C_2(s) &= k_2 \frac{\tau s + 1}{\tau s} D_1(s), \\ C_3(s) &= k_3 \frac{\tau s + 1}{\tau s} Q_{z,2}(s), & C_4(s) &= k_4 \frac{\tau s + 1}{\tau s} \tilde{Q}_{z,2}(s). \end{aligned}$$

On the one hand, C_1 and C_2 are integer-order controllers where C_1 is a PI controller only, however C_2 pseudo compensates the non-minimum phase zero by means of the mirrored pole D_1, see (3.20). The controllers C_3 and C_4 contain the explicit and implicit fractional-order terms $Q_{z,2}$ of (3.17) and $\tilde{Q}_{z,2}$ of (3.21), respectively. For comparability, the tuning of the proportional gains $[k_1, k_2, k_3, k_4] = [0.68, 0.772, 1.091, 0.7245]$ yields an open-loop crossover frequency of $\omega_\mathrm{c} = 0.54\,\mathrm{rad/s}$ for all controllers. Note that the relatively high value of k_3 is caused by the magnitude drop around $\omega = z$ (see Figure 3.1).

The Bode plot of the open loops $L_i = GC_i$, depicted in Figure 3.8 (next page), reveals the differences between the controllers. As mentioned above, the magnitude of L_3 is higher for low frequencies due to the compensation of the magnitude drop at the non-minimum phase zero. The magnitude slope for high frequencies is very different, as expected from the previous considerations. Considering the phase, we can observe the earlier drop of L_3 compared to the others as well as the general differences between the total phase lag in accordance with the magnitude slope. The gain margin of all loops but L_1 is $A_{\mathrm{r},i} > 3\,\mathrm{dB}$, $i = 2, 3, 4$ and $A_{\mathrm{r},1} = 1.26\,\mathrm{dB}$.

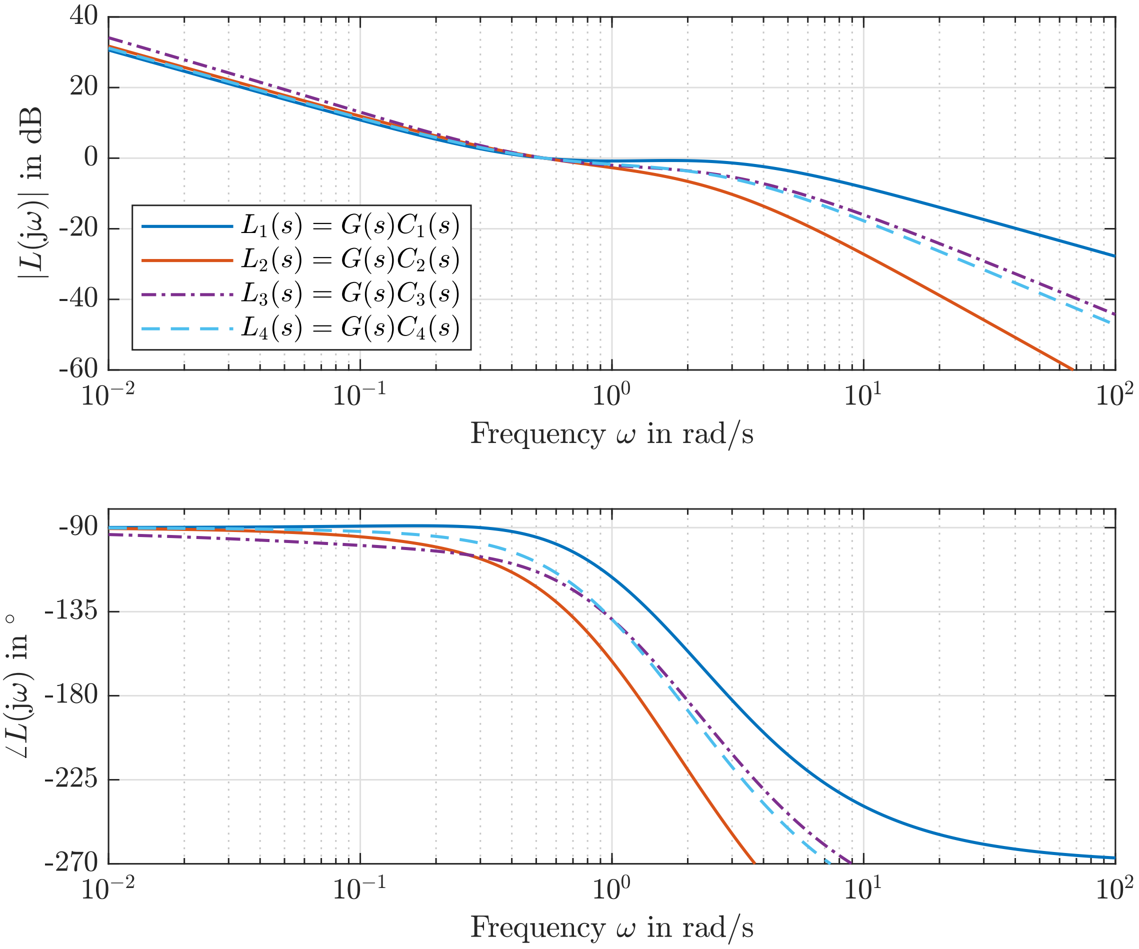

Figure 3.8: Bode plot of $L_i = GC_i$, $i = 1, \ldots, 4$.

The phase margins are $\Phi_{\mathrm{r},i} > 55°$, $i = 1, \ldots, 4$. Thus, we expect all controllers to yield acceptable results apart from C_1.

For time-domain simulations, we approximate the terms $Q_{z,2}$ and $\tilde{Q}_{z,2}$ of non-integer order with an Oustaloup filter in the frequency range $[\omega_\mathrm{l},\, \omega_\mathrm{h}] = [0.001\,\frac{\mathrm{rad}}{\mathrm{s}},\, 1000\,\frac{\mathrm{rad}}{\mathrm{s}}]$ with $N = 5$. The differences are clearly visible in the step response of the closed loops, depicted in Figure 3.9 on the next page. The reference step is given at $t = 0\,\mathrm{s}$ whereas an input disturbance step occurs at $t = 15\,\mathrm{s}$.

Consider the time responses involving the integer-order controllers C_1 and C_2. Obviously, for the present controller tuning, it is necessary to address the non-minimum phase zero, since C_1 leads to unacceptable behavior for both steps. It is evident that better controller tuning would reduce the oscillations. Still, the additional elements yield a significant reduction of both the initial undershoot as well as the oscillations. The integer-order pseudo compensation with C_2 also improves the behavior. In comparison with C_3 and C_4 however, it is significantly slower while only showing

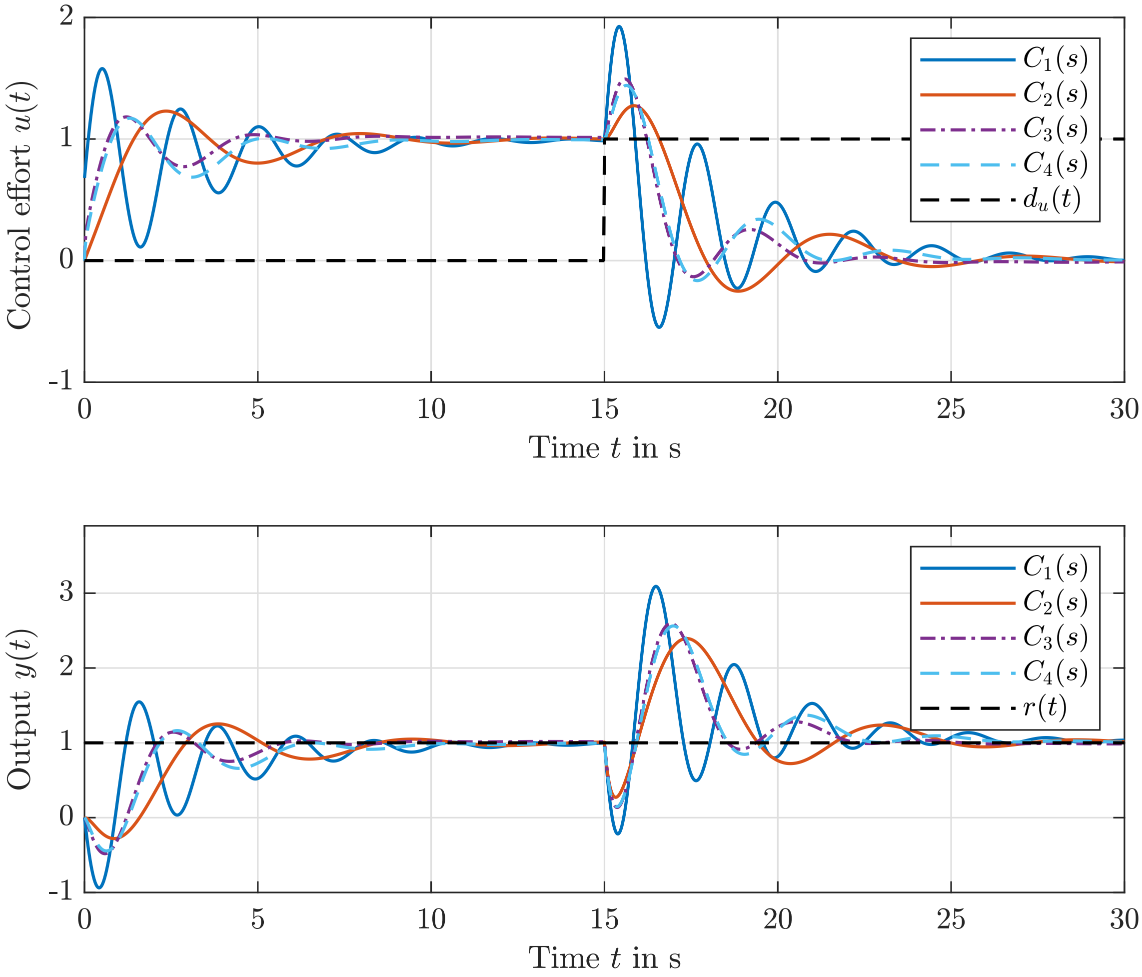

Figure 3.9: Closed-loop time-responses to a step in the reference at $t = 0$ s and the disturbance at $t = 15$ s.

little reduction of the undershoots. The controllers with explicit cancellation C_3 and implicit compensation C_4 show very similar behavior, where C_3 leads to faster convergence for both steps. This is caused by the higher proportional gain to achieve the same crossover frequency ω_c.

4 Modeling of the Two-Mass Oscillator

The laboratory setup of the experiment is investigated in this chapter in order to derive a detailed model for later controller synthesis as well as simulation studies. The considered plant is a two-mass oscillator with non-collocated actuator and measurement as depicted in Figure 4.1 in the laboratory setup. The plant is connected to the power supply and the real-time hardware (SpeedGoat Real-Time Target Baseline-S with IO183 interfacing card [40]) which is used to control the process. Thus, it receives and processes the measurement data in order to send the control signal to the actuator unit and therefore allows to artificially inject a communication delay. It is also connected to the computer for real-time interaction with the plant.

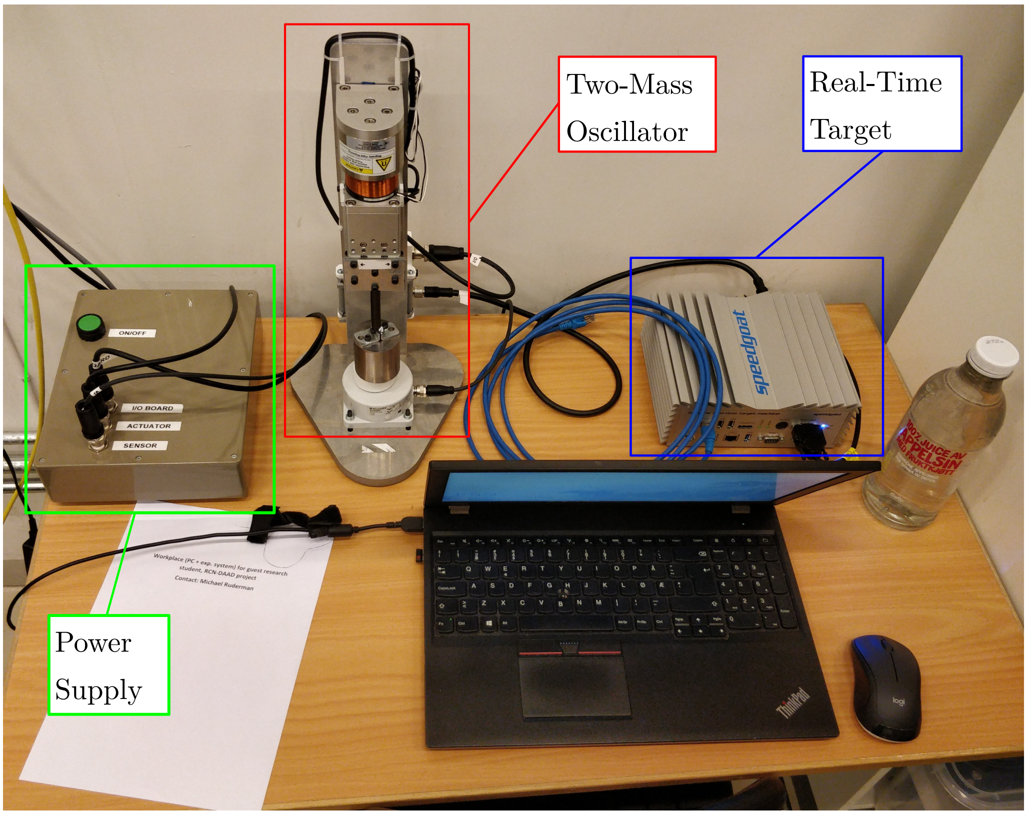

Figure 4.1: Laboratory setup of the experiment consisting of power supply, plant (two-mass oscillator), real-time target (SpeedGoat) and computer.

In the following section a linear model of the plant is derived. In Section 4.2 we identify the stroke-dependent force which is typical for the utilized actuator unit. Afterwards, the process noise is characterized by a normal distribution and two harmonics in Section 4.3. Finally, in Section 4.4, the model for the controller synthesis is presented, i.e. the linear plant model combined with a communication delay.

Parts of this chapter have been submitted to an IFAC conference for possible publication [44].

4.1 Physical Model

A detailed illustration of the plant in the laboratory setting is given in Figure 4.2. The plant consists of two masses m and M that are subjected to gravity $d = -mg$ and $D = -Mg$, respectively, where g is the gravity constant. The active mass m with bounded displacement $x_1(t) \in [0\,\mathrm{mm}, 20\,\mathrm{mm}]$ is controlled by the actuator unit (MGV 52 [1]) that receives the control signal $u(t) \in [0\,\mathrm{V}, 10\,\mathrm{V}]$. A spring with spring constant k connects the active mass with the load (passive mass M). For control we can only utilize the load position $\tilde{x}_3(t)$ which is obtained by contact-less measurement (BAW003K [3]).

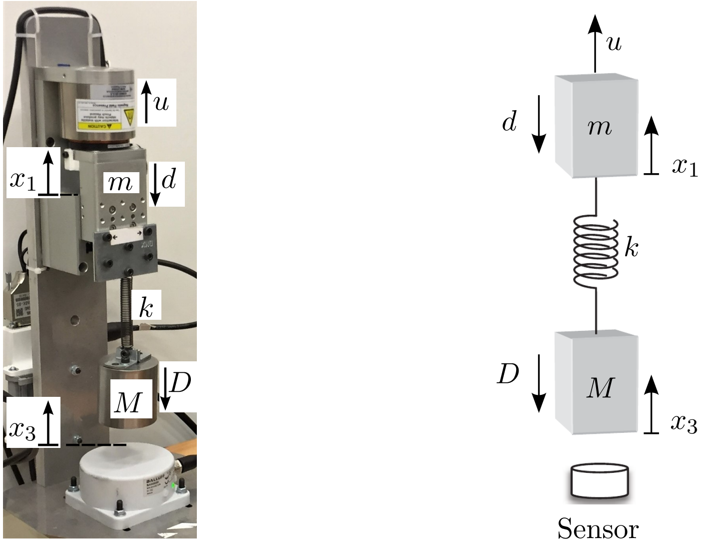

Figure 4.2: Experimental setup of the two-mass oscillator [36, 37] with actuator and contact-less measurement unit.

To derive the physical model of the plant, we use relative coordinates of the load position, i.e. $x_3(t) = \tilde{x}_3(t) - \tilde{x}_{3,0}$, where $\tilde{x}_{3,0}$ is the steady-state measurement for $u = 0$. The current dynamics are neglected, since the inductance of the actuator is relatively small [1]. Similar to [37], this yields

$$m\,\ddot{x}_1 = -\left(\eta + \zeta\right)\dot{x}_1 - k\left(x_1 - x_3\right) + \zeta \dot{x}_3 + d + \frac{\Psi}{R}u\,, \tag{4.1a}$$

$$M\,\ddot{x}_3 = \zeta\left(\dot{x}_1 - \dot{x}_3\right) + k\left(x_1 - x_3\right) + D. \tag{4.1b}$$

Note that the time argument of the control signal $u(t)$ and states $x_i(t)$, $i \in \{1, 3\}$ is omitted for brevity. The damping of the active and the passive mass are denoted as η and ζ with $\zeta \ll \eta$. The actuator is characterized by the resistance R and the back electromotive force (EMF) constant Ψ. The nominal values of the model parameters are summarized in Table 4.1.

Table 4.1: Nominal values of model parameters.

Parameter	**Value**	**Unit**	**Meaning**
k	200	N/m	Spring constant
m	0.6	kg	Active mass
M	0.75	kg	Passive mass (load)
η	200	kg/s	Viscous damping of active mass
ζ	0.02	kg/s	Viscous damping of passive mass
Ψ	17.16	Vs/m	Actuator EMF constant
R	5.23	V/A	Actuator resistance

We can reformulate (4.1) leading to the state space representation

$$\dot{x} = Ax + Bu + E\begin{bmatrix} d \\ D \end{bmatrix}, \quad x(t_0) = x_0\,, \tag{4.2a}$$

$$y = Cx \tag{4.2b}$$

with the state vector $x = [x_1 \;\; x_2 \;\; x_3 \;\; x_4]^\top$ where $x_2 = \dot{x}_1$, $x_4 = \dot{x}_3$ and initial conditions x_0. The system matrix A, input matrix B and disturbance matrix E are given by

$$A = \begin{bmatrix} 0 & 1 & 0 & 0 \\ \frac{-k}{m} & \frac{-1}{m}(\eta+\zeta) & \frac{k}{m} & \frac{\zeta}{m} \\ 0 & 0 & 0 & 1 \\ \frac{k}{M} & \frac{\zeta}{M} & \frac{-k}{M} & \frac{-\zeta}{M} \end{bmatrix}, \quad B = \begin{bmatrix} 0 \\ \frac{\Psi}{Rm} \\ 0 \\ 0 \end{bmatrix} \quad \text{and} \quad E = \begin{bmatrix} 0 & 0 \\ \frac{1}{m} & 0 \\ 0 & 0 \\ 0 & \frac{1}{M} \end{bmatrix},$$

the output matrix is $C = \begin{bmatrix} 0 & 0 & 1 & 0 \end{bmatrix}$.

As we assume the gravitational forces d and D to be constant and known, constant feedforward-action can be applied. For this purpose, consider (4.1) and choose the coordinate system to be located at the equilibrium point with respect to D. Then, we can apply the feed-forward action $u_d = -(d+D)\frac{R}{\Psi} = (m+M)\frac{gR}{\Psi}$ to compensate the gravitational forces. Therefore, it is not necessary to include d and D into further considerations.

For later loop-shaping controller design, it is necessary to describe the input-output behavior in terms of a transfer function. Using the state space realization (4.2) with the nominal parameter values (Table 4.1) yields

$$G_{yu}(s) = C\,(sI - A)^{-1}\,B = \frac{0.14583\,(s + 10^4)}{s\,(s + 332.4)\,(s^2 + 1.027s + 267.4)} \tag{4.3}$$

that consists of a stable fast pole ($p_1 = -332.4$) and zero as well as an integrator ($p_2 = 0$) and a low-damped complex pole-pair at $p_{3,4} = -0.514 \pm \mathrm{j}\,16.346$. The location of the poles in the complex plane is depicted in Figure 4.3.

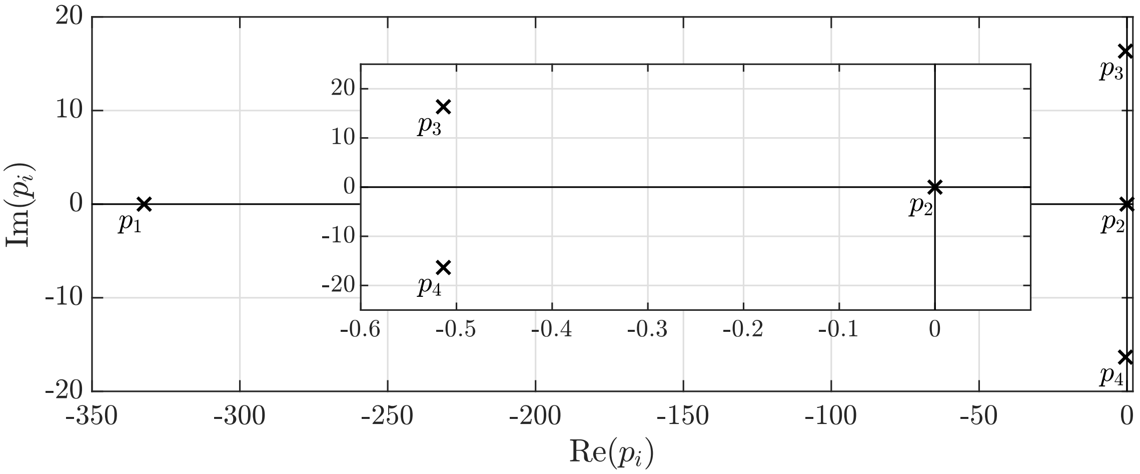

Figure 4.3: Location of the plant poles in the complex plane.

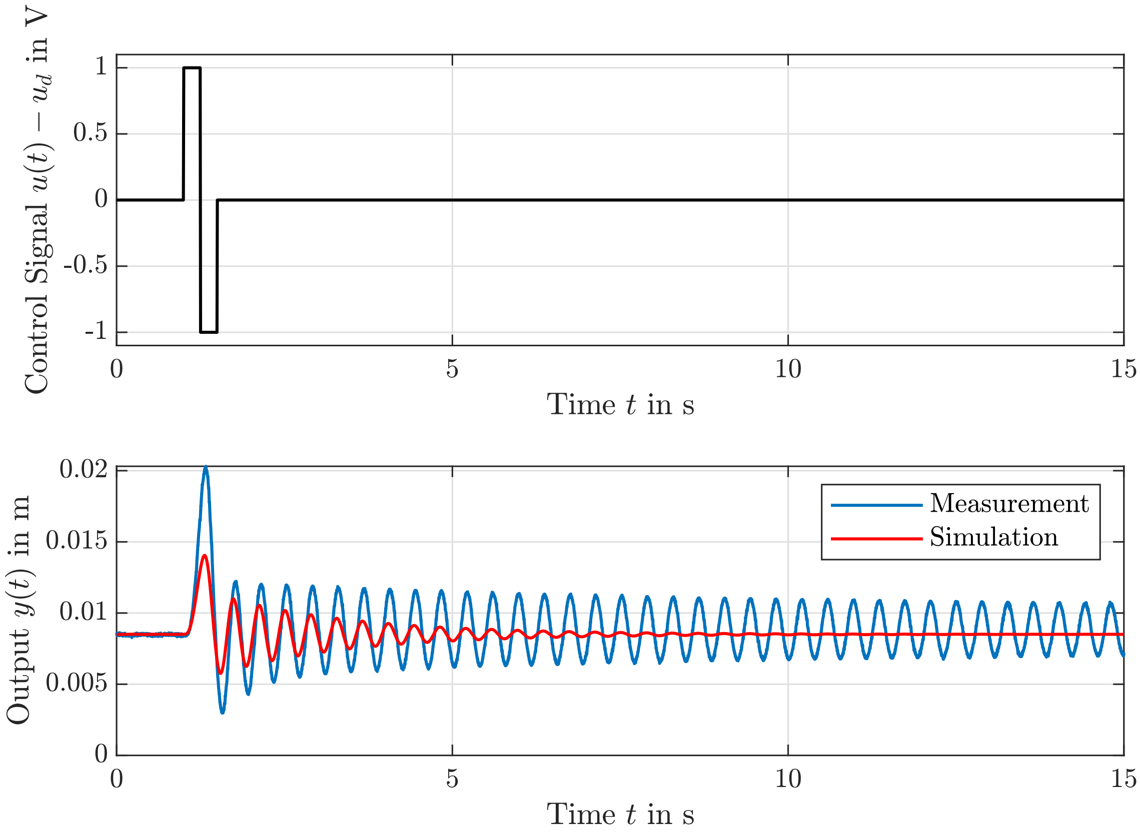

Figure 4.4: Open-loop impulse response of the experiment and the simulation.

Having established a linear model, we can compare the open-loop model response to the behavior of the physical plant in order to gain insight into the accuracy of the model fit. For this purpose, starting from $x_0 \approx [0.0085 \;\; 0 \;\; 0.0085 \;\; 0]^\top$, the open loop is exited with

$$u(t) = u_d + \sigma\left(t - t_1\right) - 2\sigma\left(t - t_1 - T_\mathrm{p}\right) + \sigma\left(t - t_1 - 2T_\mathrm{p}\right)$$

where $\sigma(\cdot)$ denotes the step function, i.e. a zero-mean square pulse starting at $t_1 = 1$ s with pulse width $T_\mathrm{p} = 0.5$ s. Figure 4.4 presents the simulation and experimental results. Apparently, the eigenfrequency $\omega_0 = 16.346\,\mathrm{rad/s}$ of the model and physical process coincides. Still, significant differences can be observed, on the one hand in the transient peaking, in the damping on the other hand. It seems to be not only linear viscous damping. A controller has to compensate for these non-modeled effects, hence has to be robust.

4.2 State-Dependent Input Gain

As it is typical for voice coil motors, a stroke-dependent force of the actuator (AVM60-25 [1]) can be observed. Using a controller that contains an integrator to achieve stationary precision and targeting different reference positions in a closed-loop setup, it becomes visible in terms of a state-dependent input gain. We denote the input gain as $k_u(x_1)$ where x_1 is the position of the active mass. Only the position of the passive mass x_3 can be measured. However, due to the connecting spring, their relative displacement coincides in steady-state: $x_{1,\mathrm{ss}} = x_{3,\mathrm{ss}}$. Hence, for a given steady-state reference position r_ss of the hanging load, the applied steady-state control signal can be seen as dependent on the position of the active mass $u_\mathrm{ss} = u_\mathrm{ss}(x_{1,\mathrm{ss}})$. This allows to identify $k_u(x_1)$ in the described setup. We consider two initial conditions $x_{0,1} = [0 \;\; 0 \;\; 0 \;\; 0]^\top$ and $x_{0,2} = [0.02 \;\; 0 \;\; 0.02 \;\; 0]^\top$, i.e. the lower and the upper limit of the actuator range, and target a grid of reference positions.

Figure 4.5 shows the experimental results as well as the least-squares optimal, second-order polynomial fit

$$u_\mathrm{ss}(x_{1,\mathrm{ss}}) = 2123.20\; x_{1,\mathrm{ss}}^2 - 37.84\; x_{1,\mathrm{ss}} + 4.69. \tag{4.4}$$

Now we make use of the equilibrium of forces between the actuator and the gravitational forces to calculate $k_u(x_1)$, which yields:

$$(m+M)g = k_u(x_1)\; u_\mathrm{ss}(x_1)\; \frac{\Psi}{R} \quad \Longrightarrow \quad k_u(x_1) = \frac{(m+M)gR}{\Psi\; u_\mathrm{ss}(x_1)}. \tag{4.5}$$

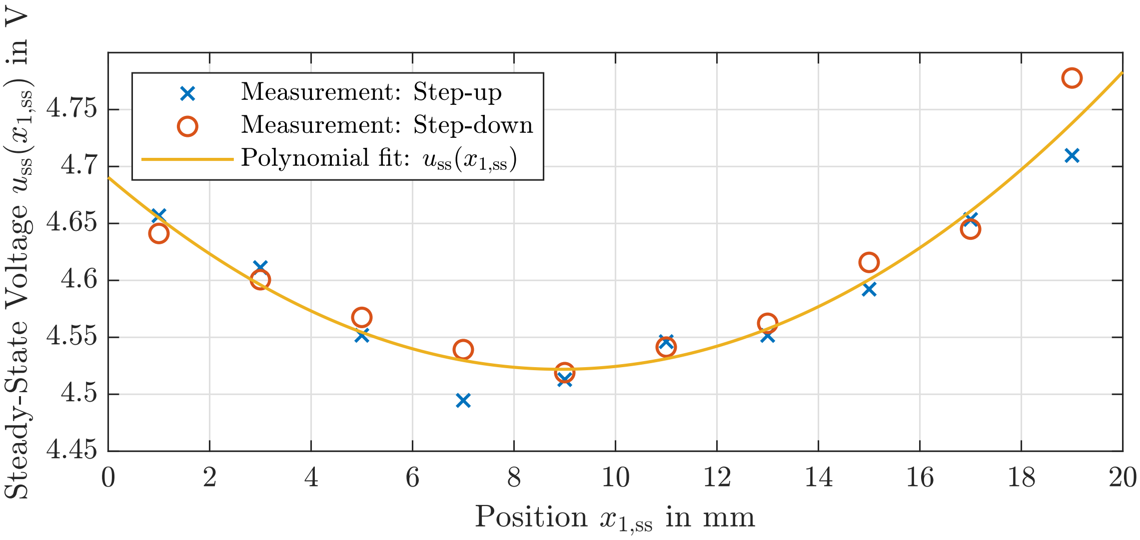

Figure 4.5: Experimental identification of the steady-state input voltage to compensate the gravitational forces. 'Step-up' and 'Step-down' refer to the initial conditions $x_{0,1}$ and $x_{0,2}$, respectively.

For later simulation studies, $k_u(x_1)$ is utilized to improve the model. It is worth mentioning that the inverse of this nonlinearity cannot be used for control purposes since only the position of the hanging load is measured. However, we can use the mean of the inverse input gain $\mu\left(k_u^{-1}\right)$ as a static pre-compensation.

4.3 Process Noise Model

In order to identify a process noise model of the experimental setup, measurements are conducted for the resting masses, i.e. for $u = 0$. The length of an exemplary measurement is 20 min at $f_{\mathrm{s}} = 2$ kHz leading to $2.4 \cdot 10^6$ data points. The power spectrum of the mean-adjusted measurement data is shown in Figure 4.6. Obviously, there are three dominant peaks at $f_0 = \frac{\omega_0}{2\pi} = 2.6$ Hz, $f_1 = 74$ Hz as well as $f_2 = 2f_1 = 148$ Hz. Furthermore, a peak at $f_3 = 3f_1$ and an elevation around $f = 771$ Hz can be observed. However, both are well-damped and the elevation is not present in all measurements. It probably arises due to other active machines that are located near the experimental setup. Thus, the following discussions are restricted to the three dominant peaks.

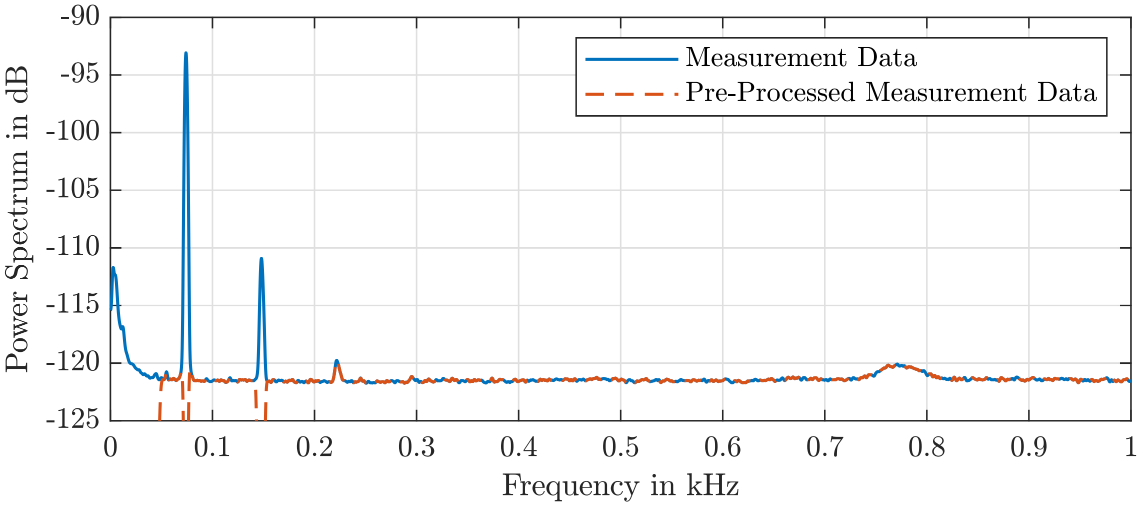

Figure 4.6: Power spectrum of a process noise measurement at $f_s = 2$ kHz.

The derivation of the process noise model is carried out in the following steps:

1. Pre-processing of the measurement data
2. Normal distribution fit
3. Injection of the dominant harmonics

As f_0 corresponds to the mechanical eigenfrequency, the hanging load is not perfectly resting. To ensure that the mechanical oscillations are not part of the noise model, the measurement data is pre-processed with a high-pass filter with passband frequency $f_p = 50$ Hz. The two dominant peaks are addressed by notch-filters with the edge frequencies $[f_{1,\mathrm{l}}, f_{1,\mathrm{h}}] = [71\,\mathrm{Hz}, 77\,\mathrm{Hz}]$ and $[f_{2,\mathrm{l}}, f_{2,\mathrm{h}}] = [143\,\mathrm{Hz}, 152\,\mathrm{Hz}]$. The resulting power spectrum is shown in Figure 4.6.

The histogram of the pre-processed data is depicted in Figure 4.7 and shows a symmetrical bell shape. The normal distribution fit is determined with standard deviation $\sigma_{\mathrm{noise}} = 1.867 \cdot 10^{-5}$ and mean $\mu_{\mathrm{noise}} = 0$, which is part of Figure 4.7 as well. The main characteristics are captured by the noise model. Utilizing this model in simulation studies will thus lead to similar experimental results with respect to noise attenuation. Therefore, this distribution fit is expected to be sufficient.

Finally, the two harmonics β_1 and β_2 are injected to reproduce the noise measurement. The amplitude of each sine wave is determined by the power spectrum, see Figure 4.6, whereas the relative phase shift is used to fit the histogram of the high-pass filtered measurement data, depicted in Figure 4.8.

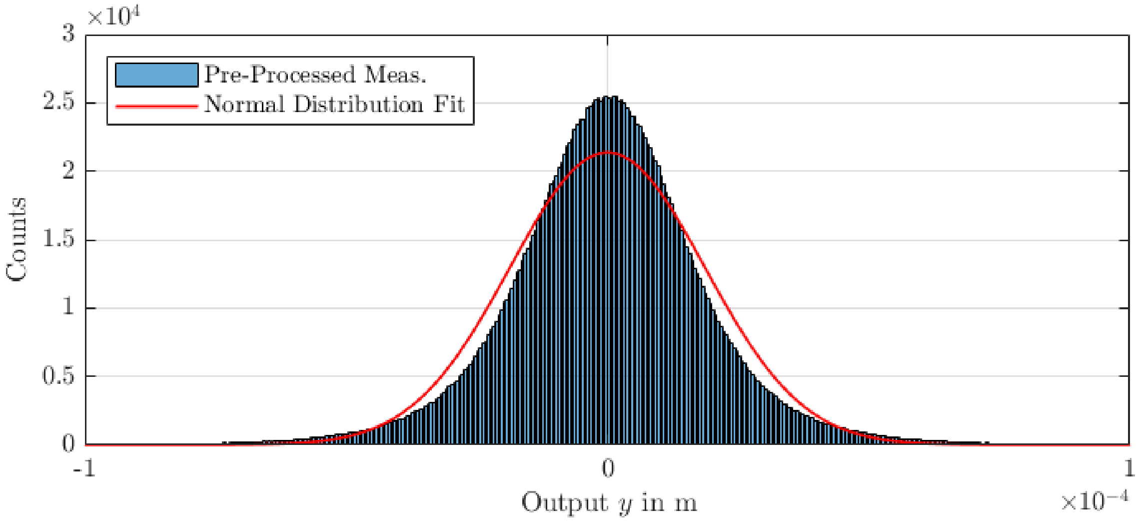

Figure 4.7: Histogram and normal distribution fit of the pre-processed measurement data.

Best results are achieved with

$$\beta_1(t) = 3.166 \cdot 10^{-5} \sin\left(2\pi f_1 t - \frac{\pi}{3}\right) \quad \text{and} \quad \beta_2(t) = 3.986 \cdot 10^{-6} \sin\left(2\pi f_2 t\right). \quad (4.6)$$

The histogram of the simulation results with the process noise model is generated with the above-mentioned normal distribution as well as the two harmonics. The resulting power spectrum is shown in Figure 4.9.

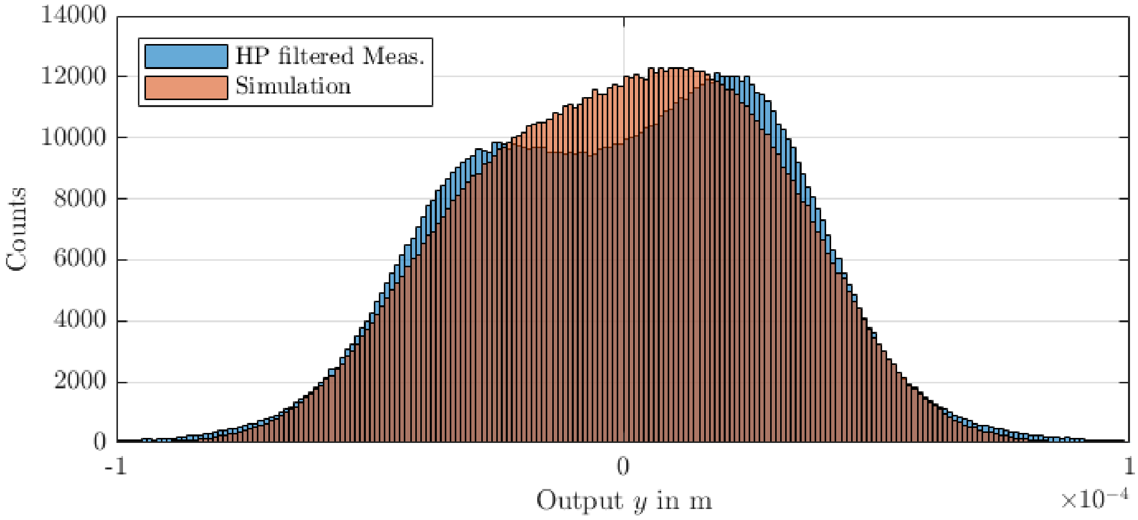

Figure 4.8: Histogram of the high-pass (HP) filtered measurement data and the simulation results with the identified process noise model.

Both the histogram and the power spectrum confirm that the model is able to describe the main process noise characteristics with only little differences in the distribution on the one hand and deviations in the power spectrum on the other hand.

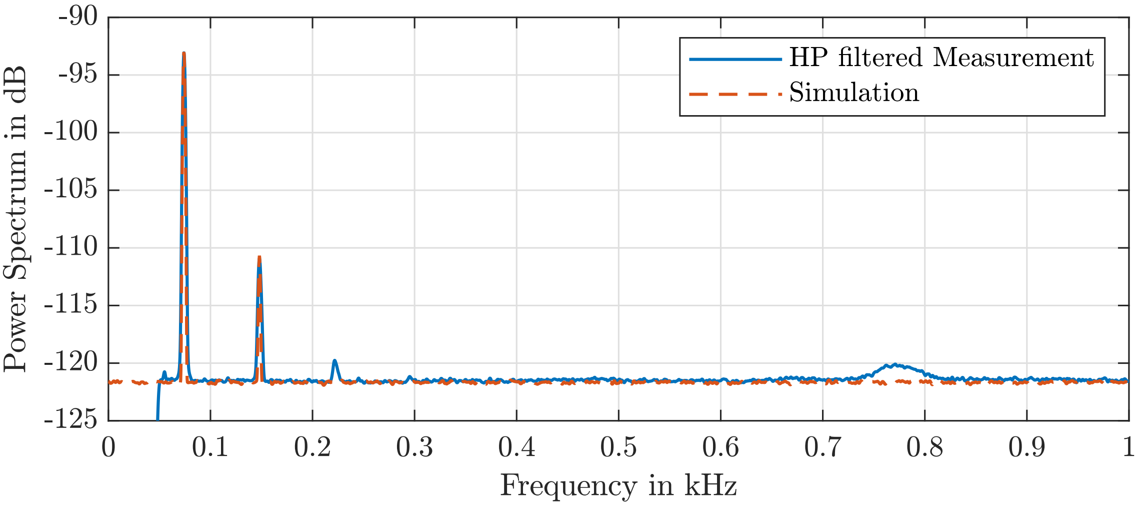

Figure 4.9: Power spectrum of the high-pass filtered measurement data and the simulation results with the identified process noise model.

It is used to improve later simulation studies and the controller synthesis, i.e. the frequencies f_1 and f_2 should be well-damped. Therefore, the model is considered to be sufficient.

An interesting observation is made at measurements of the real-time hardware internal converters, i.e. the measurement unit [3] is turned off. In this case, the dominant peaks are located at $\tilde{f}_1 = 50$ Hz, $\tilde{f}_2 = 2\tilde{f}_1$ and $\tilde{f}_3 = 3\tilde{f}_1$ which coincides with the frequency of the power supply grid. The power spectrum of an exemplary measurement is shown in Figure 4.10 and reveals the origins of the peaks in the power spectra of Figures 4.6 and 4.9. Note that the frequencies are shifted by $\Delta f \approx 24\,\text{Hz}$, i.e. $f_k = k\left(\tilde{f}_1 + \Delta f\right)$ with $k = 1, 2, 3$.

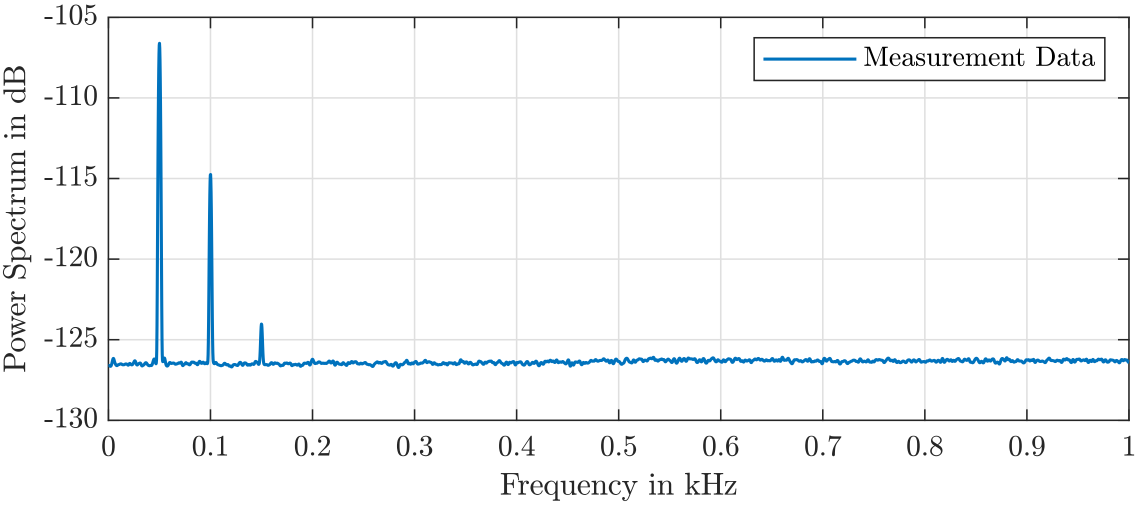

Figure 4.10: Power spectrum of a converter noise measurement at $f_\text{s} = 2$ kHz.

4.4 Communication Delay

The experimental setup allows to artificially inject an input delay τ, e.g. to simulate a communication delay. It can be easily incorporated into the plant model and reads

$$G(s) = G_{yu}(s)\ G_{\mathrm{d}}(s) = \frac{0.14583\,(s+10^4)}{s\,(s+332.4)\,(s^2+1.027s+267.4)} e^{-\tau s}. \tag{4.7}$$

We investigate two cases. On the one hand, a dominant delay with the nominal value $\tau_1 = \frac{2\pi}{\omega_0} = 0.3844\,\mathrm{s}$ is considered. On the other hand, we regard a less significant delay $\tau_2 = \frac{\tau_1}{5} = 0.07688\,\mathrm{s}$.

Model (4.7) is the basis for the controller synthesis in the following chapter, where both cases are considered.

5 Controller Design

In this chapter, two different synthesis methods are utilized to design controllers for the plant model $G(s)$, provided in (4.7), including the communication delay τ. On the one hand, $\mathcal{H}_\infty$ controller synthesis methods are used to design a reference controller in Section 5.1. On the other hand, fractional-order loop-shaping with classical feed-forward is utilized as described in Section 5.2. Having discussed the general design procedures, the design parameters and resulting controllers for two different delays are presented afterwards. For a fair comparison, the controllers are designed to have a similar order n, open-loop crossover frequency ω_c and gain for low frequencies. For good tracking performance two-degree of freedom (2DOF) control structures are used.

The Padé-approximation $R_j(s)$ of (2.24) is utilized to account for the time delay in the $\mathcal{H}_\infty$ framework. The order j depends on the dominance of the delay, i.e.

$$G_\mathrm{d}(s) = e^{-\tau s} \approx R_j(s), \quad j \in \{1, 2\} \tag{5.1}$$

$$\tilde{G}(s) = G_{yu}(s)\ R_j(s) \tag{5.2}$$

where we use the nominal value of the delay τ_i, $i \in \{1, 2\}$ for the controller design in each case. Note that $G_{yu}(s)$ contains an integrator already, thus the additional phase lag of low-order approximations (compare Figure 2.4b) is considered sufficient for controller design. To ensure a fair comparison of the resulting controllers, $\tilde{G}(s)$ is also used for the fractional-order loop-shaping, where the first-order approximation turns out to be sufficient. We expect the controllers to achieve a minimum phase margin of 30° to allow for delay uncertainties.

Parts of this chapter have been submitted to an IFAC conference for possible publication [44].

5.1 Two Degree of Freedom $\mathcal{H}_\infty$ Control

As we consider two nominal values for the communication delay separately, the next section only presents the design procedure that is used in both cases. Afterwards, the resulting controllers are given together with the corresponding open-loop Bode plots. It follows a short discussion and justification for the chosen design structure.

5.1.1 Design Procedure

The 2DOF control structure of Figure 5.1, inspired by [12], is used to achieve better tracking performance.

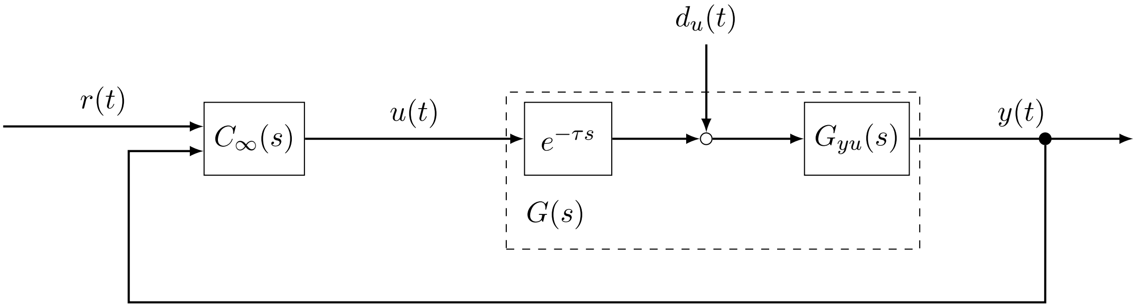

Figure 5.1: Two degree of freedom control structure.

Besides, disturbance attenuation of input disturbances is considered relevant. To directly account for these disturbances, we extend the external input to $w = [r \;\; d_u]^\top$. The elements of the performance output $v = [v_1 \;\; v_2]^\top$ are weighted with W_i and chosen as

$$v_1 = W_1(y - r) \quad \text{and} \quad v_2 = W_2 u. \tag{5.3}$$

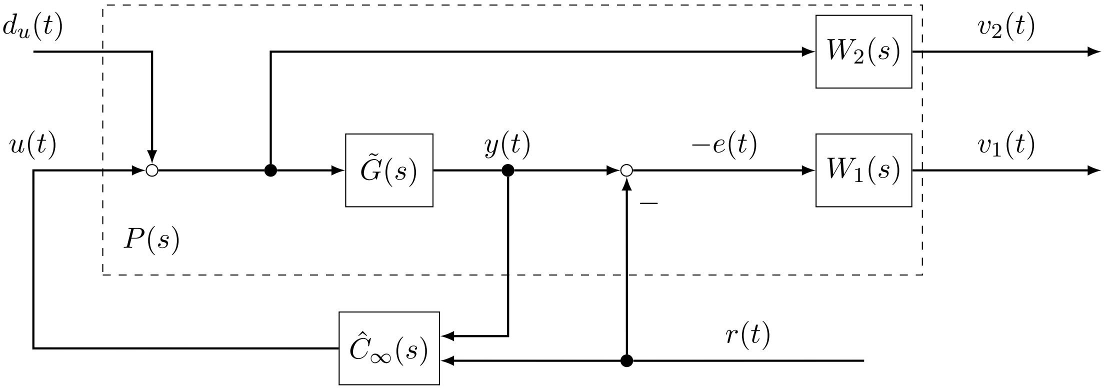

Figure 5.2: Structure of the extended plant $P(s)$ used for the $\mathcal{H}_\infty$ controller synthesis.

Thus, W_1 considers the control error $e = r - y$ and is therefore chosen as a low-pass filter. A high gain for low frequencies yields an almost integrating behavior with a pole at $-\epsilon$. By weight W_2, the control signal including the input disturbance d_u is considered. Choosing it as a high-pass filter limits the tracking performance, however ensures noise reduction by limiting the bandwidth of u. These considerations lead to the weight functions proposed by [39]

$$W_1(s) = \frac{0.01(s + z_{1,i})}{s + p_{1,i}} \quad \text{and} \quad W_2(s) = \frac{0.95(s + z_{2,i})}{s + p_{2,i}} \tag{5.4}$$

with $p_{1,i} \ll z_{1,i}$, $p_{2,i} \gg z_{2,i}$ for $i \in \{1, 2\}$ corresponding to the dominant and less dominant communication delay τ_1 and τ_2, respectively.

An illustration of the resulting generalized plant is depicted in Figure 5.2. The transfer matrix reads

$$P(s) = \left[\begin{array}{cc:c} -W_1(s) & W_1(s)\tilde{G}(s) & W_1(s)\tilde{G}(s) \\ 0 & W_2(s) & W_2(s) \\ \hdashline 1 & 0 & 0 \\ 0 & \tilde{G}(s) & \tilde{G}(s) \end{array}\right] \quad \text{with} \quad \begin{bmatrix} V_1(s) \\ V_2(s) \\ R(s) \\ Y(s) \end{bmatrix} = P(s) \begin{bmatrix} R(s) \\ D_u(s) \\ U(s) \end{bmatrix} \tag{5.5}$$

where the capital letters denote the Laplace transforms for zero initial conditions, e.g $V_1(s) = \mathcal{L}\{v_1(t)\}(s)$ is the Laplace transform of v_1.

As already described in Section 2.2.3, the MATLAB Robust Control Toolbox routine `hinfsyn` (based on [8, 11]) can be used to synthesize a sub-optimal stabilizing 2DOF controller $\hat{C}_\infty$ determining

$$\left\| P_{11} + P_{12}\hat{C}_\infty \left(I - P_{22}\hat{C}_\infty\right)^{-1} P_{21} \right\|_\infty = \left\| \mathcal{F}_l\left(P, \hat{C}_\infty\right) \right\|_\infty < \gamma < 1 \tag{5.6}$$

with $\gamma = 0.96$ (i.e. the transfer function from the external input w to the performance output v). Since $\hat{C}_\infty$ contains a pole at $-\epsilon$ with $\epsilon < 2 \cdot 10^{-3}$, integrating behavior can be stressed to achieve stationary precision:

$$\hat{C}_\infty(s) = \frac{1}{\epsilon + s}\tilde{C}_\infty(s) \approx \frac{1}{s}\tilde{C}_\infty(s) \equiv C'_\infty(s). \tag{5.7}$$

Finally, we use a balanced truncation algorithm (`balred` based on [42]) on C'_∞ to reduce the controller order resulting in C_∞ of order $n_\infty \leq 7$.

Table 5.1: Parameters of the weight functions $W_1(s)$ and $W_2(s)$ in (5.4) for the nominal communication delays τ_1 and τ_2.

i	Nominal Communication Delay τ_i	$p_{1,i}$	$z_{1,i}$	$p_{2,i}$	$z_{2,i}$
1	0.3844 s	0.0015	15	2850	3
2	0.07688 s	0.003	30	4750	5

5.1.2 Dominant Communication Delay τ_1

Considering the dominant communication delay $\tau_1 = 0.3844\,\text{s}$, it turns out to be necessary making use of the second-order Padé-term $R_2(s)$ in (5.2). The weight function parameters are chosen according to Table 5.1.

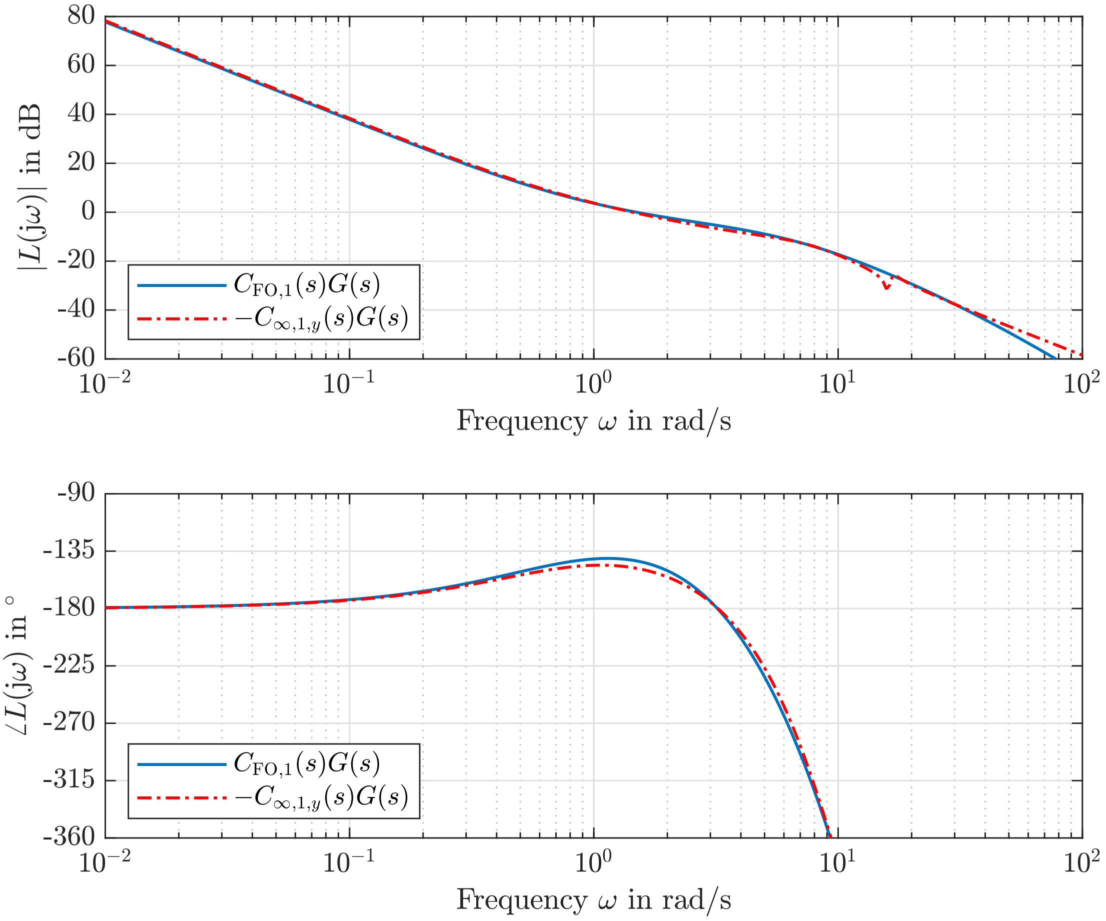

Figure 5.3: Bode plot of the open-loop transfer functions for the dominant communication delay τ_1 with $C_{\mathrm{FO},1}$ and $C_{\infty,1,y}$, respectively.

With the above-described procedure the resulting controller reads

$$C_{\infty,1}(s) = \begin{bmatrix} C_{\infty,1,r}(s) & C_{\infty,1,y}(s) \end{bmatrix} \quad \text{with} \tag{5.8a}$$

$$C_{\infty,1,r}(s) = \frac{-0.030643(s-538.6)(s+31.93)(s+8.538)}{s(s+507.2)(s+72.68)} \cdot \frac{(s^2-32.18s+1.846\cdot 10^4)(s^2-314s+1.923\cdot 10^5)}{(s^2+9.086s+63.62)(s^2+307.9s+1.36\cdot 10^5)}, \tag{5.8b}$$

$$C_{\infty,1,y}(s) = \frac{-3.3043(s-3.893\cdot 10^4)(s-1534)(s+62.69)}{s(s+507.2)(s+72.68)} \cdot \frac{(s+7.822)(s+0.6413)(s^2+0.5762s+257.6)}{(s^2+9.086s+63.62)(s^2+307.9s+1.36\cdot 10^5)} \tag{5.8c}$$

where $C_{\infty,1,r}$ and $C_{\infty,1,y}$ correspond to the reference r and the output y, respectively. Figure 5.3 shows a Bode plot of the open loop $L_{\infty,1} = -C_{\infty,1,y}G$ for $r = 0$. The crossover frequency of $\omega_{\mathrm{c},\infty,1} = 1.44$ rad/s, phase margin of $\Phi_{\mathrm{r},\infty,1} = 32.09°$ and gain margin of $A_{\mathrm{r},\infty,1} = 2.18$ are determined numerically.

The frequency response of the feedforward path $F_{\infty,1} = C_{\infty,1,r}$ from reference r to control signal u, depicted in Figure 5.4, shows integrating behavior for low frequencies. On the other hand, high frequencies of the reference signal are damped.

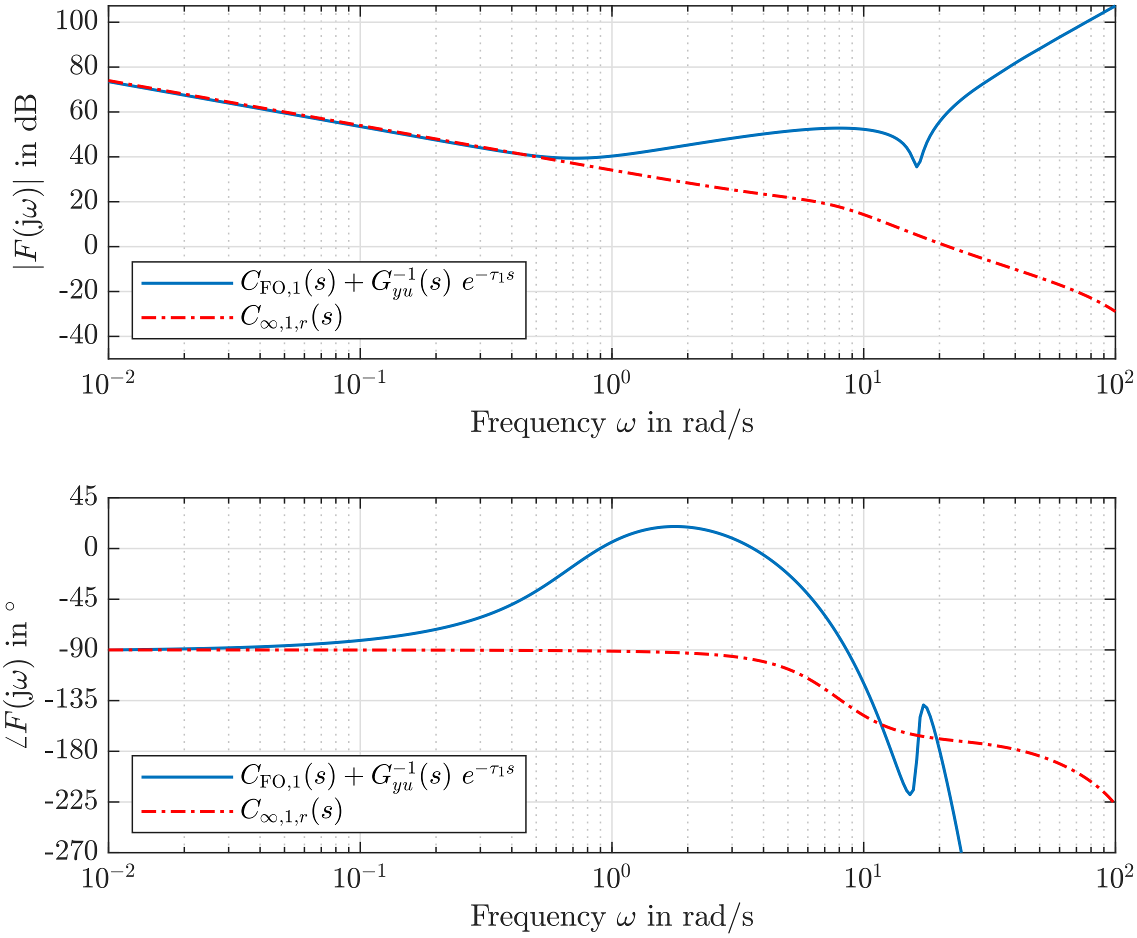

Figure 5.4: Bode plot of the feedforward paths for the dominant delay τ_1 from r to u for both control structures.

5.1.3 Small Communication Delay τ_2

The weight function parameters for the small delay $\tau_2 = 0.07688\,\mathrm{s}$ are part of Table 5.1. In this case, the first-order Padé-approximation of the time delay (2.24a) is sufficient, since the resulting zero and pole are at higher frequencies.

This leads to the controller

$$C_{\infty,2}(s) = \begin{bmatrix} C_{\infty,2,r}(s) & C_{\infty,2,y}(s) \end{bmatrix} \quad \text{with} \tag{5.9a}$$

$$C_{\infty,2,r}(s) = \frac{10.4903(s+70.34)(s^2-139.5s+1.889\cdot 10^5)(s^2-1063s+1\cdot 10^6)}{s(s+9.152)(s^2+1078s+3.334\cdot 10^5)(s^2+441.1s+2.903\cdot 10^5)}, \tag{5.9b}$$

$$C_{\infty,2,y}(s) = \frac{-7.1364\cdot 10^5(s+2065)(s+340.2)(s+1.081)(s^2+1.569s+257.6)}{s(s+9.152)(s^2+1078s+3.334\cdot 10^5)(s^2+441.1s+2.903\cdot 10^5)}. \tag{5.9c}$$

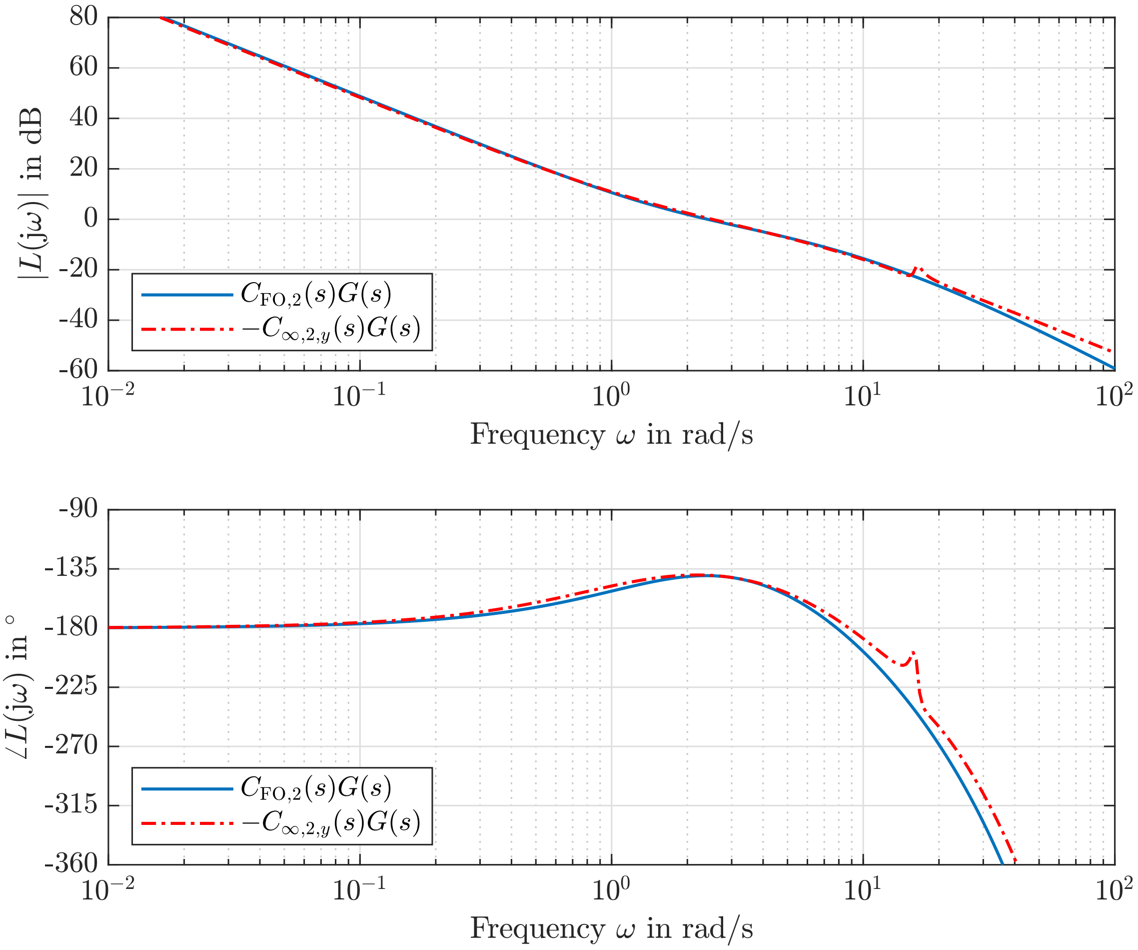

Figure 5.5: Bode plot of the open-loop transfer functions for the small communication delay τ_2 with $C_{\mathrm{FO},2}$ and $C_{\infty,2,y}$, respectively.

Figures 5.5 and 5.6 show the Bode plots of the open loop $L_{\infty,2} = -C_{\infty,2,y}G$ for $r = 0$ as well as the feedforward path $F_{\infty,2} = C_{\infty,2,r}$, respectively. In comparison with the dominant delay, the feedforward action is very similar, however shifted towards higher frequencies. The Bode plot of the open loop reveals that a crossover frequency of $\omega_{\mathrm{c},\infty,2} = 2.51$ rad/s, a phase margin of $\Phi_{\mathrm{r},\infty,2} = 40.03°$ and a gain margin of $A_{\mathrm{r},\infty,2} = 5.20$ are achieved. This highlights the effect of the non-minimum phase zero on the achievable bandwidth, as controller $C_{\infty,2}$ leads to a higher crossover frequency and larger margins due to the significantly smaller communication delay and hence faster non-minimum phase zero of the Padé-approximation (compare (2.24a)).

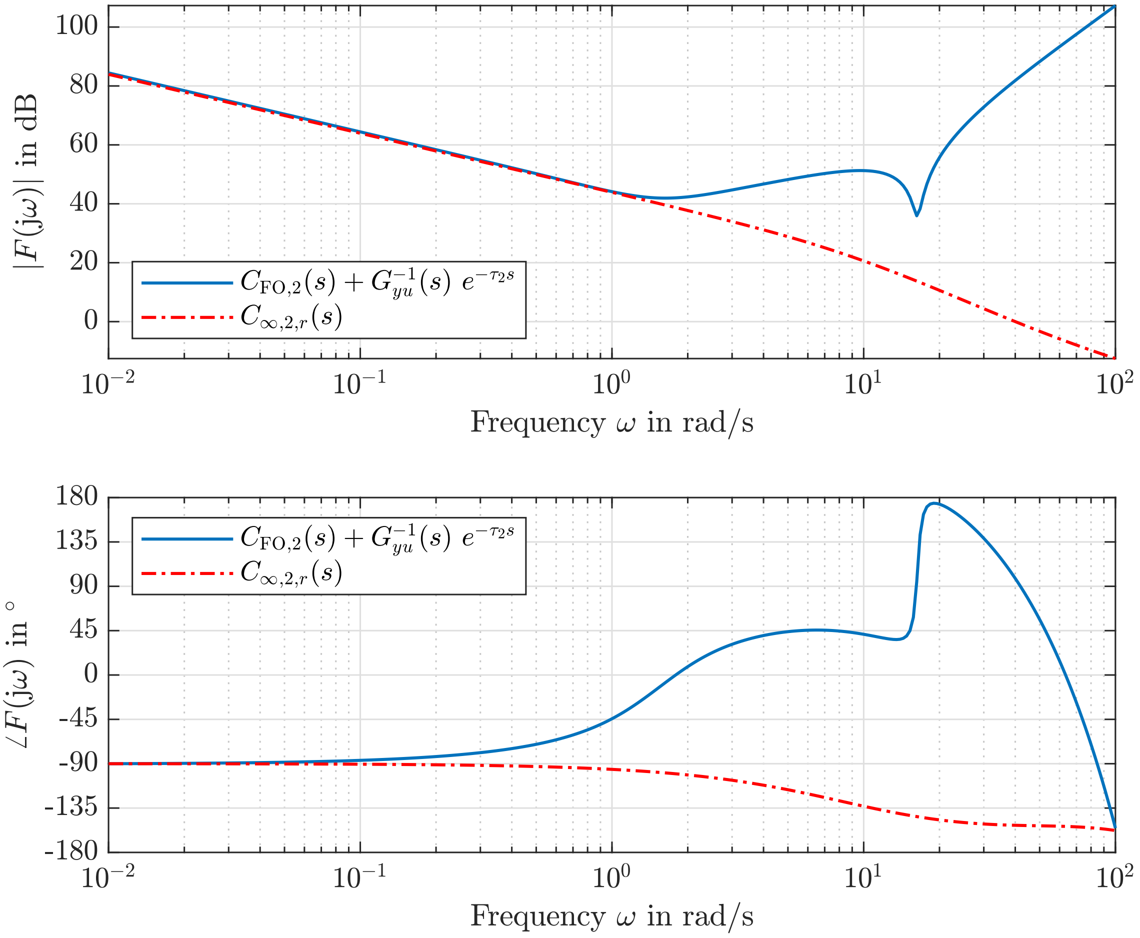

Figure 5.6: Bode plot of the feedforward paths for the small delay τ_2 from r to u for both control structures.

5.1.4 Discussion

It is worth mentioning that $\mathcal{H}_\infty$ control of systems involving a time delay is a broadly discussed topic with different proposed methods and solutions, see for example [28] and the references therein. Many propositions are predictor-based, e.g. [19, 25, 51], where some are suitable for unstable plants as well, utilizing a modified Smith predictor. Still, given a plant with fast stable eigenvalues, the modified Smith predictor may lead to numerical issues [51, p. 154]. To overcome this problem, a unified Smith predictor is proposed where further research is needed to solve the corresponding $\mathcal{H}_\infty$ problem [51].

Note that this thesis focuses on fractional-order partial pole-zero cancellation, its application to a physical experiment and comparison to a suitable reference controller. Therefore, the reference controller, i.e. the $\mathcal{H}_\infty$ controller, is chosen to be designed based on the standard $\mathcal{H}_\infty$ problem described in Section 2.2 using a rational approximation of the time delay. For comparability, the same model structure is utilized in the fractional-order loop-shaping design procedure.

Since the standard S/T- or S/CS-mixed-sensitivity $\mathcal{H}_\infty$ controller synthesis methods [39] did not lead to sufficient results with respect to tracking performance, the proposed 2DOF control structure is used, inspired by [12]. To keep the controller order low, low-order weight functions and Padé-approximations are chosen.

As stated above, the input of the generalized plant is extended with d_u to increase the disturbance attenuation capabilities of the controller. However, as the $\mathcal{H}_\infty$ controller ensures $\left\|\mathcal{F}_\mathrm{l}\left(P, \hat{C}_\infty\right)\right\|_\infty < \gamma$, the input extension leads to an injected lower bound for γ. To see this, consider the relevant sensitivities:

$$T_{v_1 r,\infty} = W_1 \left(\frac{G\hat{C}_{\infty,r}}{1 - G\hat{C}_{\infty,y}} - 1\right) = W_1\,\tilde{S}_y, \qquad T_{v_1 d_u,\infty} = W_1 \frac{G}{1 - G\hat{C}_{\infty,y}} = W_1\,S_u, \tag{5.10a}$$

$$T_{v_2 r,\infty} = W_2 \frac{\hat{C}_{\infty,r}}{1 - G\hat{C}_{\infty,y}} = W_2\,\hat{C}_{\infty,r}\;S_y \quad \text{and} \quad T_{v_2 d_u,\infty} = W_2 \frac{1}{1 - G\hat{C}_{\infty,y}} = W_2\,S_y. \tag{5.10b}$$

Note that, due to the 2DOF control structure, $\tilde{S}_y$ does not coincide with S_y of (3.57), its amplitude response approaches, however, zero for low and one for high frequencies (see e.g. the Bode plots in Figures 5.3 to 5.6). Thus, it is natural to choose W_1 as a low-pass filter for $T_{v_1 r,\infty}$ and $T_{v_1 d_u,\infty}$ in order to stress an (almost) integrating behavior. The sensitivity $T_{v_2 r,\infty}$ shows the bandwidth-limiting effect of the high-pass filter W_2. Finally, consider $T_{v_2 d_u,\infty}$ where W_2 is combined with S_y leading to

$$\lim_{\omega\to\infty} |W_2(\mathrm{j}\omega)\,S_y(\mathrm{j}\omega)| \overset{|S_y(\mathrm{j}\omega)| \xrightarrow{\omega\to\infty} 1}{=} \lim_{\omega\to\infty} |W_2(\mathrm{j}\omega)| \overset{(5.4)}{=} 0.95 \le \gamma.$$

We can thus conclude

$$0.95 \le \left\|\mathcal{F}_\mathrm{l}\left(P, \hat{C}_\infty\right)\right\|_\infty < \gamma. \tag{5.11}$$

Still, W_2 dominates W_1 for high frequencies and can be used successfully to tune a robust controller as the results show in the next chapter.

The balanced-truncation order-reduction algorithm `balred` (based on [42]) is not only used to keep the controller order low but also to ensure that all poles of the

controllers satisfy $10|p_i| < 2\pi f_\mathrm{s}$ where $f_\mathrm{s} = 5\,\mathrm{kHz}$ is the sampling frequency. In the present cases, it does not affect the $\mathcal{H}_\infty$ norm.
Note that little notches can be observed around $\omega = \omega_0$ in the open-loop Bode plots in Figures 5.3 and 5.5. These result from the order-reduction and are not caused by the $\mathcal{H}_\infty$ controller synthesis.

5.2 Fractional-Order Loop-Shaping with Classical Feedforward

Having designed the reference controllers, now we consider the classical PI-Lead controller design that is enhanced with partial cancellation of the non-minimum phase zero of $\tilde{G}(s)$. Furthermore, the complex pole-pair at $\omega_0 = 16.346\,\mathrm{rad/s}$ is subjected to an integer-order compensation. For comparability, the 2DOF control structure of Figure 5.7 is utilized.

Since the design procedure equals for both delays, it is presented first. Afterwards the classical feedforwad action based on the model-inverse is discussed. It follows a description of the resulting controllers for both nominal delays and this section concludes with a short discussion on alternative approaches.

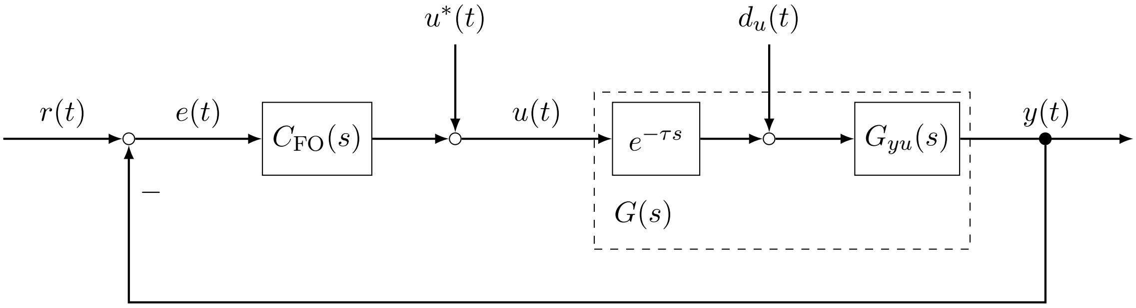

Figure 5.7: Control structure with feedforward action $u^*(t)$.

5.2.1 Fractional-Order Loop-Shaping

Consider the communication delay $\tau_i, i \in \{1, 2\}$ that results in a non-minimum phase zero in $\tilde{G}(s)$ due to the Padé-approximation (2.24a). This is close to the desired crossover frequency ω_c, see (5.2) and Figures 5.3 and 5.5. Recall that partial cancellation of a non-minimum phase zero can effectively reduce the phase lag, compared to an integer-order pseudo compensation by its mirrored pole. Chapter 3 further states that, in case of phase limitations, the *implicit* partial cancellation yields less phase loss. Therefore, the non-minimum phase zero of the Padé-approximation at $z = 2/\tau_i$ is partially compensated with the *implicit* term $\tilde{Q}_{z,\nu}$ of (3.21). The order $\nu = \alpha^{-1} = 2$ is chosen such that the phase lag is minimized and some magnitude slope is preserved to help keeping the magnitude low at ω_0. The Bode plots of the resulting $\tilde{Q}_{2/\tau_i,2}$ are presented in Figures 5.8 and 5.9.

It turns out that a PI controller design for $\tilde{Q}_{2/\tau_i,2}\tilde{G}$ aiming at similar crossover frequencies as $\omega_{\mathrm{c},\infty,i}$ is difficult for two reasons. On the one hand, despite the minimum order $\nu = 2$, the applicable proportional gain is bounded due to the necessary damping of the magnitude peak at ω_0. Recall that the model damping is overestimated (see the open-loop time-response in Figure 4.4), it is therefore necessary to further address the magnitude peak. For this purpose, we make use of the integer-order filter

$$F_{\mathrm{pp}}(s) = \frac{0.034\,(s^2 + 1.027s + 267.4)}{s + 9} \tag{5.12}$$

that compensates the stable pole-pair. The frequency response is part of Figure 5.8. Although F_{pp} is non-proper, the combination of all elements results in overall proper controllers $C_{\mathrm{FO},i}$, see (5.17) and (5.20). The pole is chosen to satisfy $\omega_0 < |p| < \omega_{\mathrm{c}}$, such that the damping at ω_0 is further increased with only little phase loss around ω_{c}.

However, even more positive phase is needed to achieve acceptable phase margins. Therefore, a lead-element is added to the PI-controllers resulting in $K_{\mathrm{PIL},i}$.

In order to use the controllers

$$\tilde{C}_{\mathrm{FO},i}(s) = K_{\mathrm{PIL},i}(s)\,F_{\mathrm{pp}}(s)\,\tilde{Q}^{-1}_{2/\tau_i,2}(s) \tag{5.13}$$

with fractional-order elements in a real-time experimental setup, an integer-order approximation of the fractional-order terms $\tilde{Q}_{2/\tau_i,2}$ is necessary, see Section 2.1.5. We therefore make use of the Oustaloup approximation described in Section 3.5. Aiming at controller orders similar to the $\mathcal{H}_\infty$ controllers, a low-order approximation is necessary. By restricting us to the relevant frequency range $[\omega_{\mathrm{l},i},\, \omega_{\mathrm{h},i}]$, even approximations with $N = 1$, leading to an order $N_{\mathrm{oust}} = 3$, achieve acceptable results in the crossover region. This can be observed in Figures 5.8 and 5.9.

5.2.2 Feedforward Action

As a second-degree of freedom the classical feedforward action [16]

$$u^*(t) = \frac{-CA^3x^*(t) + r^{(3)}(t-\tau_i)}{CA^2B} \tag{5.14}$$

is applied, where the matrices A, B and C correspond to the model equations in (4.2) and $x^*(t)$ denotes the state fitting the desired trajectory. Note that the third-order derivative of the reference trajectory $r(t)$ is necessary, which can be calculated offline since function $r(t)$ is known a priori.

We use the Laplace transform $\mathcal{L}\{\cdot\}(s)$ for zero initial conditions in order to calculate the feedforward path $F_{\text{FO},i}$ from the reference r to the control signal u, which reads

$$\mathcal{L}\left\{u^*(t)\right\} = \frac{-CA^3\mathcal{L}\left\{x^*(t)\right\} + s^3\mathcal{L}\left\{r(t-\tau_i)\right\}}{CA^2B}$$

with

$$\mathcal{L}\left\{x^*(t)\right\} = (sI-A)^{-1}B\ \mathcal{L}\left\{u^*(t)\right\}.$$

By denoting $U^*(s) = \mathcal{L}\left\{u^*(t)\right\}$ and $R(s) = \mathcal{L}\left\{r(t)\right\}$ (as used in (5.5)), we get

$$\begin{aligned}\frac{U^*(s)}{R(s)} &= \frac{s^3e^{-\tau_i s}}{CA^2B + CA^3(sI-A)^{-1}B} \\ &= G_{yu}^{-1}(s)\ e^{-\tau_i s}\end{aligned}$$

that is the inverse of the plant model shifted in time. The overall feedforward path therefore leads to the non-proper

$$F_{\text{FO},i}(s) = C_{\text{FO},i}(s) + G_{yu}^{-1}(s)\ e^{-\tau_i s}. \tag{5.15}$$

Recall that the reference signal is known a priori, hence no feasibility problems are encountered.

5.2.3 Dominant Communication Delay τ_1

The described procedure leads to the PI-Lead controller

$$K_{\text{PIL},1}(s) = \frac{213\,(s+2)\left(s+\frac{2}{3}\right)}{s\,(s+6)} \tag{5.16}$$

for the dominant delay τ_1. The Bode plot is shown in Figure 5.8.

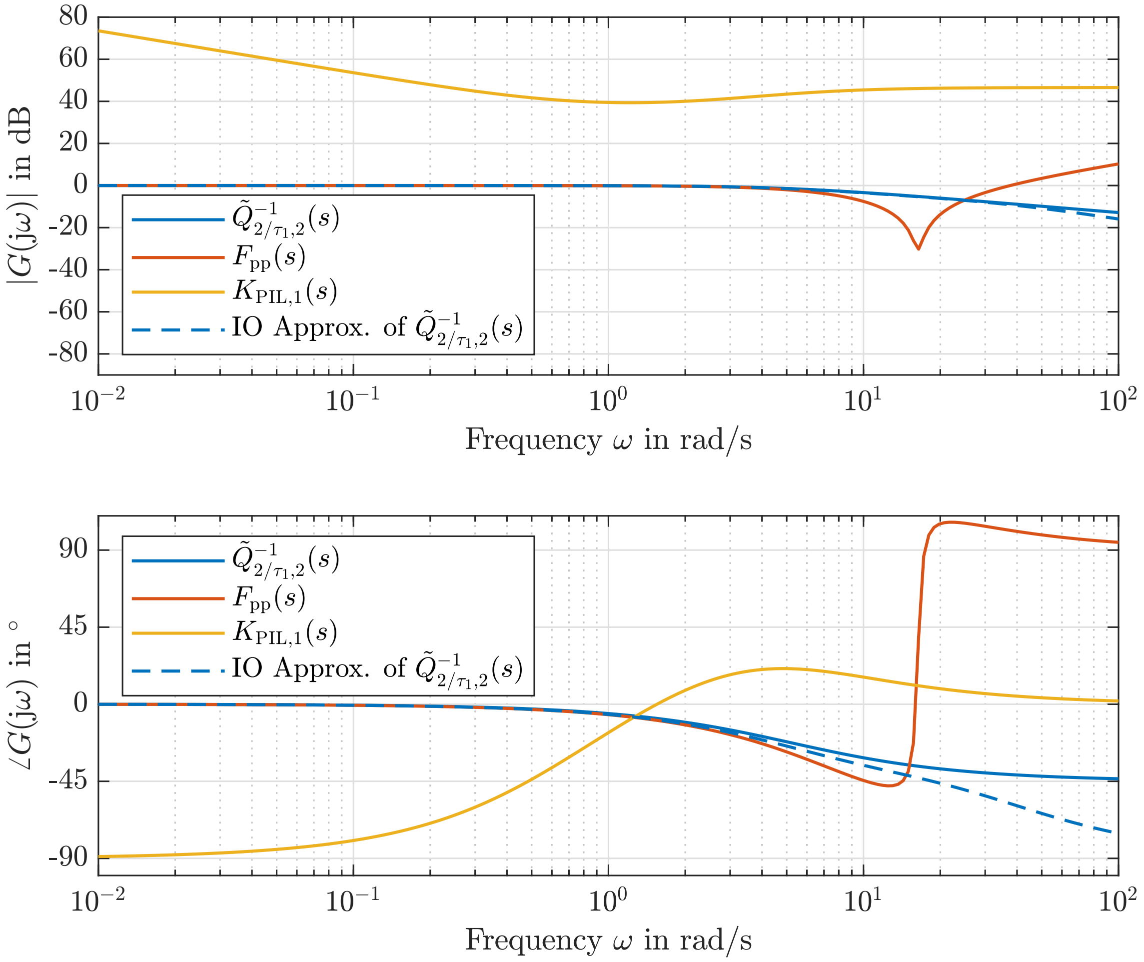

Figure 5.8: Bode plot of the controller elements for $C_{\mathrm{FO},1}$.

The fractional-order term $\tilde{Q}_{2/\tau_1,2}$ to partially compensate the non-minimum phase zero is depicted in Figure 5.8 alongside with its integer-order approximation in the frequency range $[\omega_{\mathrm{l},1},\, \omega_{\mathrm{h},1}] = \left[0.05\,\frac{\mathrm{rad}}{\mathrm{s}},\, 50\,\frac{\mathrm{rad}}{\mathrm{s}}\right]$.

Including the approximation, the overall controller for the dominant delay reads

$$C_{\mathrm{FO},1}(s) = \frac{120.2(s+14.09)(s+6.092)(s+5.292)(s+2)(s+0.6667)}{s(s+6)(s+5.484)(s+5.203)(s+8.015)} \cdot \frac{(s^2+1.027s+267.4)}{(s+9)(s+33.32)}. \quad (5.17)$$

The same controller order as $C_{\infty,1}(s)$ of (5.8) is achieved with $n_{\mathrm{FO},1} = n_{\infty,1} = 7$. The frequency characteristics of the open-loop $L_{\mathrm{FO},1} = C_{\mathrm{FO},1}G$ is shown in Figure 5.3 opposite to the $\mathcal{H}_\infty$ controller. An open-loop crossover frequency of $\omega_{\mathrm{c,FO},1} = 1.49$ rad/s, phase margin of $\Phi_{\mathrm{r,FO},1} = 37.36°$ and gain margin of $A_{\mathrm{r,FO},1} = 1.81$ can be obtained.

The feedforward action, depicted in Figure 5.4, consists of two parts, where $C_{\mathrm{FO},1}$ dominates at low frequencies and G_{yu}^{-1} at high frequencies. We can observe a continuously increasing phase lag due to the time-shift and the magnitude plot shows the characteristic notch of the model-inverse.

5.2.4 Small Communication Delay τ_2

Considering the small delay τ_2, the PI-Lead controller design results in

$$K_{\mathrm{PIL},2}(s) = \frac{160\,(s+2)\,\left(s+\frac{5}{3}\right)}{s\,(s+3.2)} \tag{5.18}$$

with the frequency response given in Figure 5.9. Note that, although the phase-lift caused by the lead element is not obvious, $K_{\mathrm{PIL},2}$ cannot be reduced to a PI controller only. Consider for example

$$K_{\mathrm{PI}}(s) = \frac{160\,(s+1.048)}{s} \tag{5.19}$$

that reasonably matches the asymptotic frequency response of $K_{\mathrm{PIL},2}$. Still, $K_{\mathrm{PIL},2}$ shows less phase lag in the relevant region, as it can be seen in a Bode plot in Figure A.3. It is assumed however that the lead element is not crucial in this case and a similar frequency response could be determined by making use of the remaining degrees of freedom, e.g. the pole of F_{pp} in combination with the zero of the PI controller. Furthermore, such a combined design of all elements would lead to a lower-order controller.

The integer-order approximation of the implicit fractional-order term $\tilde{Q}_{2/\tau_2,2}$ is determined for $[\omega_{\mathrm{l},2},\, \omega_{\mathrm{h},2}] = \left[0.5\,\frac{\mathrm{rad}}{\mathrm{s}},\, 500\,\frac{\mathrm{rad}}{\mathrm{s}}\right]$ and is part of Figure 5.9. The resulting overall controller is given by

$$\begin{aligned} C_{\mathrm{FO},2}(s) = {} & \frac{622.09(s+26.9)(s+34.91)(s+114.9)(s+2)(s+1.667)}{s(s+3.2)(s+9)(s+26.01)(s+28.83)} \\ & \cdot \frac{(s^2+1.027s+267.4)}{(s+54.13)(s+307.2)} \end{aligned} \tag{5.20}$$

and leads to the open-loop behavior and feedforward action depicted in Figures 5.5 and 5.6, respectively. The open-loop crossover frequency is $\omega_{\mathrm{c,FO},2} = 2.41$ rad/s, the phase and gain margins are $\Phi_{\mathrm{r,FO},1} = 39.85°$ and $A_{\mathrm{r,FO},1} = 4.16$, respectively.

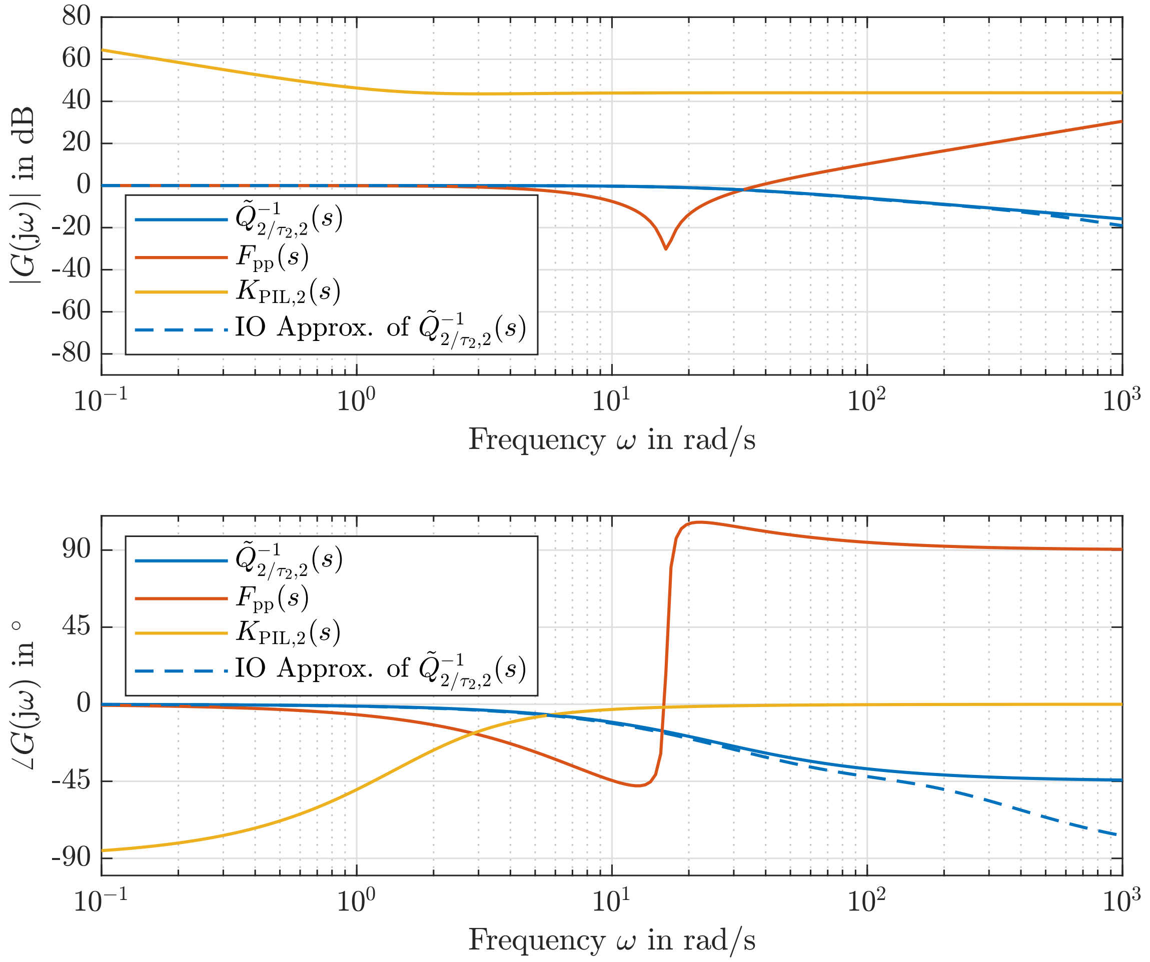

Figure 5.9: Bode plot of the controller elements for $C_{\mathrm{FO},2}$.

5.2.5 Discussion

There are a few things to mention considering the proposed design procedure that leads to an open-loop frequency response of $L_{\mathrm{FO},i}$ is similar to $L_{\infty,i}$, see Figures 5.3 and 5.5.

First, the time delay approximation in (5.1) has a stable pole that could be compensated as well. However, this would significantly reduce the magnitude slope, hence the damping of the magnitude peak. Furthermore, not enough positive phase is injected into the crossover region which does not yield similar results. Therefore, the pole is not compensated.

Second, having not enough phase margin with the integer-order PI controller, it would be natural in the scope of fractional-order controller design to make use of a fractional-order integrator, i.e. a PI$^{\mu}$ controller with $\mu \in (0, 1)$ [29], see Section 2.1.4. Following this idea, we may encounter two issues. In comparison with the $\mathcal{H}_\infty$ controller, the resulting open-loop shows less magnitude slope for low frequencies and thus violates the design specifications. Furthermore, the step response to an input disturbance shows slow convergence only, even if the fractional-order term is approximated in a small frequency range, see Figure A.6. An exemplary controller design and further results are part of Appendix A.2.

Having discussed the partial cancellation of stable conjugate complex poles in Section 3.3, it could be used instead of the integer-order cancellation of the pole pair. However, the main difficulty caused by the pole pair is the amplitude peak at ω_0, which is only partially compensated using the implicit representation. Further damping could be introduced by explicit partial cancellation, see Figure 3.4. However, this leads to a significantly earlier phase drop. Thus, the integer-order cancellation is preferred in this case, only the dominant non-minimum phase zero is subjected to partial cancellation.

5.3 Comparison

For both values of the nominal communication delay, the controllers of similar order show very similar open-loop frequency characteristics for $r = 0$ with $\omega_{\mathrm{c},\infty,i} \approx \omega_{\mathrm{c,FO},i}$, $i \in \{1, 2\}$. However, differences in the feedforward paths can be observed, see Figures 5.3 to 5.6. In comparison with $C_{\infty,i}$, the classical feedforward control is expected to act faster and more aggressive.

In order to investigate the robustness against input disturbances d_u, the disturbance sensitivity function

$$S_{yd}(s) = \frac{G_{yu}(s)}{1 + C(s)G_{\mathrm{d}}(s)G_{yu}(s)} \tag{5.21}$$

is depicted in Figure 5.10 for the nominal time delays τ_i, where $C_{\mathrm{FO},i}$ and $-C_{\infty,i,y}$ correspond to the fractional-order loop-shaping and the 2DOF $\mathcal{H}_\infty$ control, respectively. Obviously, there are only slight differences in the crossover region for τ_1 and around ω_0 for τ_2 leading to

$$\left\|S_{yd,\mathrm{FO},1}\right\|_\infty = 0.0173, \qquad \left\|S_{yd,\infty,1}\right\|_\infty = 0.0203, \tag{5.22a}$$

$$\left\|S_{yd,\mathrm{FO},2}\right\|_\infty = 0.0164 \quad \text{and} \qquad \left\|S_{yd,\infty,2}\right\|_\infty = 0.0178. \tag{5.22b}$$

In order to find the reason for the differences in the feedforward paths, we consider the weighted sensitivities in (5.10) and the feedforward action based on the model-inverse in (5.14). These can be combined to the weighted sensitivities for the

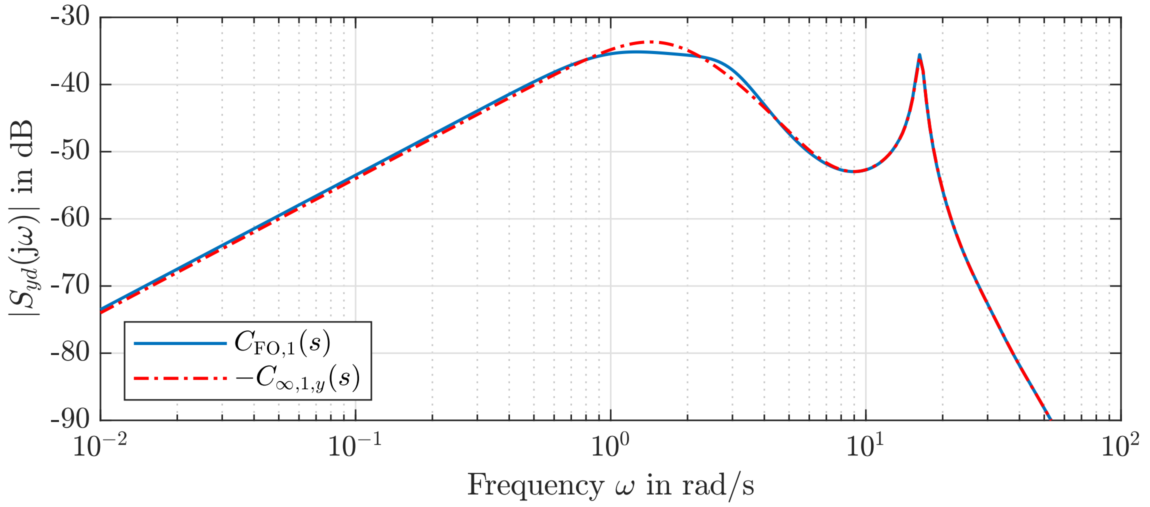

(a) Dominant communication delay τ_1.

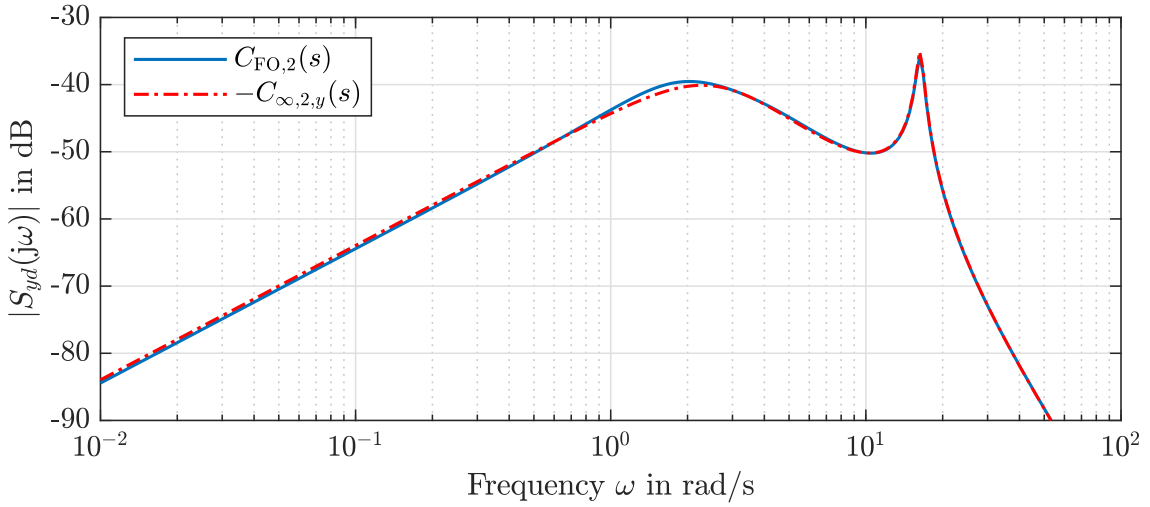

(b) Small communication delay τ_2.

Figure 5.10: Magnitude plot of the input disturbance sensitivity function for both controllers and communication delays.

fractional-order loop-shaping controller

$$T_{v_1 r,\mathrm{FO}} = W_1 \left(\frac{G F_{\mathrm{FO}}}{1 - G C_{\mathrm{FO}}} - 1 \right), \qquad T_{v_1 d_u,\mathrm{FO}} = W_1 \frac{G}{1 - G C_{\mathrm{FO}}}, \tag{5.23a}$$

$$T_{v_2 r,\mathrm{FO}} = W_2 \frac{F_{\mathrm{FO}}}{1 - G C_{\mathrm{FO}}} \quad \text{and} \qquad T_{v_2 d_u,\mathrm{FO}} = W_2 \frac{1}{1 - G C_{\mathrm{FO}}} \tag{5.23b}$$

where index $i \in \{1, 2\}$ and argument 's' are omitted for clarity. As described in Section 5.1.4, W_2 limits the bandwidth. Being interested in the feedforward action, we need to have a closer look at $T_{v_2 r,\mathrm{FO}} = W_2 S_y F_{\mathrm{FO}}$. Knowing that F_{FO} is non-proper and

$$\lim_{\omega \to \infty} \left(W_2(\mathrm{j}\omega) \right) = 0.95, \quad \lim_{\omega \to \infty} \left(S_y(\mathrm{j}\omega) \right) = 1,$$

we can conclude that

$$\lim_{\omega \to \infty} \left(T_{v_2 r,\mathrm{FO}}(\mathrm{j}\omega) \right) = \infty,$$

hence $\left\| T_{v_2 r,\mathrm{FO}} \right\|_\infty$ is unbounded. This obviously violates the constraint for the upper bound γ and, thus, cannot be achieved within the chosen $\mathcal{H}_\infty$ controller synthesis framework.

The $\mathcal{H}_\infty$ norms of the remaining weighted sensitivities in (5.23) with the weight functions W_i of (5.4) and the corresponding parameters in Table 5.1 are summarized in Table 5.2. The fractional-order loop-shaping controller $C_{\mathrm{FO},i}$ with feedforward path $F_{\mathrm{FO},i}$ already contains the Oustaloup approximation of the fractional-order elements. For comparison, the $\mathcal{H}_\infty$ norms of the weighted sensitivities (5.10) using the 2DOF $\mathcal{H}_\infty$ controller $C_{\infty,i}$ are presented as well. As discussed in Section 5.1.4, we have $\|T_{v_2 d_u}\|_\infty = 0.95$ in all cases due to the structure of the generalized plant P and the weight W_2. The sensitivities $T_{v_1 r}$ and $T_{v_1 d_u}$ consider the effect of the reference and input disturbance on the weighted error, i.e. the performance output v_1 (cf. (5.3)). The feedforward action based on the model-inverse leads to a significant reduction of $\|T_{v_1 r}\|_\infty$ for the fractional-order controllers. However, the performance of the $\mathcal{H}_\infty$ controllers is slightly better regarding input disturbances in terms of $\|T_{v_1 d_u}\|_\infty$. Since the weight functions are designed for each nominal value of the time delay separately, we do not generally expect better performance values for the smaller delay τ_2 by means of the $\mathcal{H}_\infty$ norms in Table 5.2.

Table 5.2: $\mathcal{H}_\infty$ norms of the weighted sensitivities (5.10) and (5.23) based on the first-order Padé-approximation of the nominal time delays τ_i, $i \in \{1, 2\}$.

Controller	$\|\boldsymbol{T_{v_1 r}}\|_\infty$	$\|\boldsymbol{T_{v_1 d_u}}\|_\infty$	$\|\boldsymbol{T_{v_2 r}}\|_\infty$	$\|\boldsymbol{T_{v_2 d_u}}\|_\infty$
$C_{\infty,1}$	0.2340	0.0030	0.0701	0.9500
$C_{\mathrm{FO},1}$	0.1218	0.0032	∞	0.9500
$C_{\infty,2}$	0.2762	0.0019	0.0993	0.9500
$C_{\mathrm{FO},2}$	0.0526	0.0020	∞	0.9500

Having designed and compared the different controllers for the two nominal values of the communication delay, the next section describes the results if we apply these controllers to the simulation model and experimental setup.

6 Simulation and Experimental Results

The evaluation considers two main objectives: the disturbance attenuation and the tracking performance. For the simulation studies, the model derived in Chapter 4 is utilized. It contains the linear part of the plant, see (4.2), the state-dependent input gain $k_u(x_1)$ of (4.5), the process noise model of Section 4.3 and the communication delay τ. In practice, a communication delay is expected to be hardly constant and well-estimated. Thus, the robustness of the controllers against delay uncertainties is of special interest. The artificially injected delay therefore varies by $\pm 10\,\%$, that is $\tau = \tau_i(1 \pm 0.1)$, $i \in \{1, 2\}$.

The laboratory setup of the two-mass oscillator is shown in Figures 4.1 and 4.2. Closed-loop experiments show a sticking phenomenon of the actuator similar to static friction. To counteract this phenomenon, a low-amplitude, however high-frequency jitter signal can be injected on top of the control signal, as suggested in other fields [13, 14]. A square wave with the amplitude $A_\mathrm{j} = 0.4$ V and the frequency $\omega_\mathrm{j} = 450$ rad/s yields best results. To estimate the effect of the jitter signal on the output, consider the disturbance sensitivity function S_{yd} in Figure 5.10. The frequency ω_j is not explicitly represented. Still, the magnitude is very small for high frequencies $|S_{yd}(\mathrm{j}\omega)| < -100$ dB $\forall \omega > 100$ rad/s leading to the expectation of a sufficient damping despite the non-vanishing amplitude A_j. Furthermore, a necessary adjustment of the input gain by $k_m = 1.3$ is revealed. This can be handled with the static pre-compensation k_m^{-1}.

Parts of this chapter have been submitted to an IFAC conference for possible publication [44].

6.1 Disturbance Attenuation

Regarding input disturbances, the largest effect on the output is expected for frequencies $\omega \in \Omega_\mathrm{d} = \left[0.1\,\frac{\mathrm{rad}}{\mathrm{s}}, 20\,\frac{\mathrm{rad}}{\mathrm{s}}\right]$ in both cases, i.e. $\tau = \tau_1$ and $\tau = \tau_2$ (see Figure 5.10). In order to construct a disturbance $d_u(t)$ of this frequency range with limited amplitude, band-limited white noise is used via inverse Fourier transformation and normalization. This keeps the actuator output and states in the feasible range (see Section 4.1).

A short period of exemplary time responses to the input disturbance is shown in Figure 6.1 for the nominal value of the dominant communication delay $\tau = \tau_1$. The disturbance injection starts at $t = 2$ s. To be in the middle of the actuator range, the

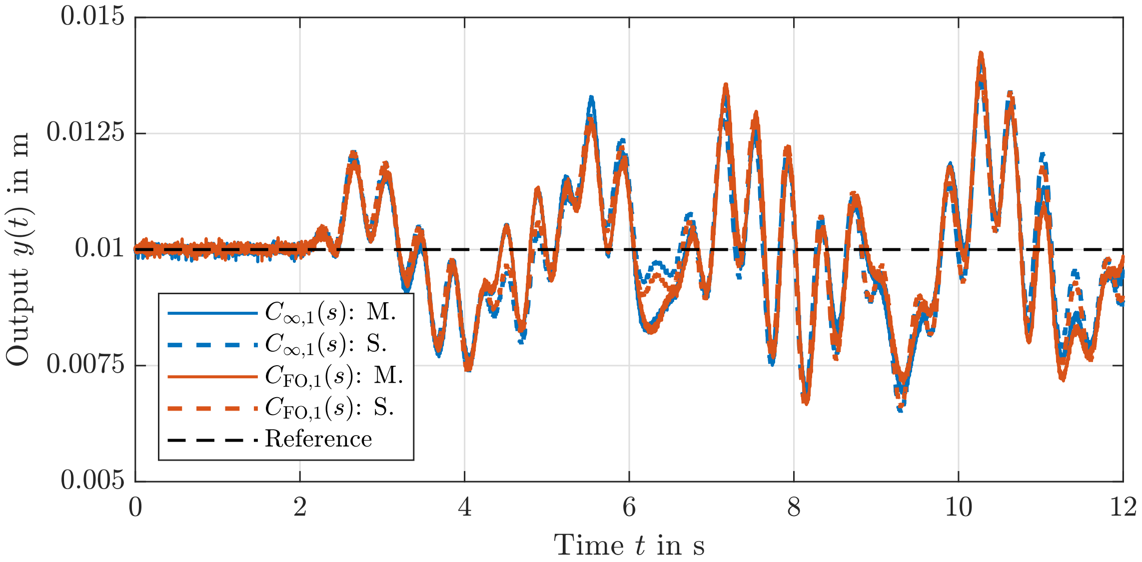

Figure 6.1: Exemplary time responses to the input disturbance for both controllers with the nominal value of the dominant time delay $\tau = \tau_1$. Measurement and simulation are abbreviated by 'M.' and 'S.', respectively.

initial conditions are chosen as $x_{0,\mathrm{d}} = [0.01 \;\; 0 \;\; 0.01 \;\; 0]^\top$. Analogue time responses for the small communication delay are depicted in Figure A.7 in Appendix A.3.1. The similarity of the controllers in terms of their input disturbance sensitivity functions (cf. Figure 5.10) is clearly visible in the time responses. Furthermore, apart from only short-time deviations, e.g. around $t = 6.3\,\mathrm{s}$, the detailed simulation model precisely captures the plant dynamics.

To evaluate the experimental and simulation results, we utilize several metrics. On the one hand, the root-mean-square (RMS) error

$$e_{\mathrm{RMS}} = \sqrt{\frac{1}{N}\sum_{n=1}^{N} e_n^2} \tag{6.1}$$

is considered, where $e_n = e(nT_\mathrm{s})$ with sample time $T_\mathrm{s} = 2 \cdot 10^{-4}\,\mathrm{s}$. On the other hand, the maximum absolute error and control effort

$$|e_{\max}| = \max_{1\le n\le N} |e_n| \quad \text{and} \quad |u_{\max}| = \max_{1\le n\le N} |u_n| \tag{6.2}$$

are determined (with $u_n = u(nT_\mathrm{s})$).

The results are summarized in Table 6.1. First, consider the experimental results for the dominant communication delay τ_1 in Table 6.2a. Obviously, the best performance is achieved with $C_{\infty,1}$ for the reduced communication delay $\tau = 0.9\,\tau_1$. Focusing on the absolute values $|e_{\max}|$ and $|u_{\max}|$, it outperforms $C_{\mathrm{FO},1}$.

Table 6.1: Disturbance attenuation simulations and experiments for both communication delays: e in mm and u in V. Green indicates the best value of the considered metric and nominal communication delay, whereas orange highlights the worst performance.

(a) Dominant communication delay $\tau_1 = 0.3844\,\mathrm{s}$.

Controller	**Metric**	**Experiments**			**Simulations**		
		$\tau = 0.9\tau_1$	$\tau = \tau_1$	$\tau = 1.1\tau_1$	$\tau = 0.9\tau_1$	$\tau = \tau_1$	$\tau = 1.1\tau_1$
$C_{\infty,1}$	e_{RMS}	1.624	1.702	1.729	1.595	1.669	1.743
	$\lvert e_{\max}\rvert$	7.603	7.986	8.511	6.130	6.501	6.849
	$\lvert u_{\max}\rvert$	4.942	4.974	5.080	4.384	4.396	4.418
$C_{\mathrm{FO},1}$	e_{RMS}	1.637	1.632	1.692	1.576	1.641	1.703
	$\lvert e_{\max}\rvert$	8.812	8.781	8.683	5.800	6.039	6.346
	$\lvert u_{\max}\rvert$	5.031	5.010	5.114	4.384	4.397	4.408

(b) Small communication delay $\tau_2 = 0.07688\,\mathrm{s}$.

Controller	**Metric**	**Experiments**			**Simulations**		
		$\tau = 0.9\tau_2$	$\tau = \tau_2$	$\tau = 1.1\tau_2$	$\tau = 0.9\tau_2$	$\tau = \tau_2$	$\tau = 1.1\tau_2$
$C_{\infty,2}$	e_{RMS}	1.318	1.343	1.381	1.328	1.332	1.336
	$\lvert e_{\max}\rvert$	5.787	6.015	6.495	5.305	5.357	5.409
	$\lvert u_{\max}\rvert$	5.116	5.253	5.234	4.523	4.828	4.778
$C_{\mathrm{FO},2}$	e_{RMS}	1.303	1.359	1.431	1.314	1.318	1.324
	$\lvert e_{\max}\rvert$	5.991	7.234	6.852	5.325	5.375	5.426
	$\lvert u_{\max}\rvert$	4.889	5.088	4.929	4.431	4.743	4.444

However, the $\mathcal{H}_\infty$ controller shows more variations for a change in τ than $C_{\mathrm{FO},1}$, especially for the root-mean-square (RMS) error e_{RMS}. The metrics for the simulation results are similar to the experiments, as expected from the time response in Figure 6.1. However, even if the simulation model is detailed, there are still unmodeled effects, see e.g. Figure 4.4. Therefore small deviations between the simulation and experimental results can be observed. In the present case, the $\mathcal{H}_\infty$ controller shows the worst values in all metrics. It outperforms $C_{\mathrm{FO},1}$ only once, where the difference between the two controllers is very little (fourth digit of $\lvert u_{\max}\rvert$ for $\tau = 0.9\,\tau_1$). All simulations with $\tau = 1.1\,\tau_1$ show the worst behavior for both controllers, as it is naturally expected for the increased dominant time delay, hence reduced phase margins.

Second, consider the simulation and experimental results for the small communication delay in Table 6.2b. Regarding the best values, the simulations and experiments coincide principally. The RMS error is dependent on the delay, also for the small nominal value τ_2. The maximum values, however, do not show a consistent trend.

All evaluation metrics are generally better for the small communication delay. This is in accordance with the greater margins of the corresponding controllers, see Sections 5.1.3 and 5.2.4, and the smaller $\mathcal{H}_\infty$ norms of the input disturbance sensitivity functions in (5.22). In both cases the deviations between experiment and simulation are sufficiently small. Hereafter we thus focus on the experimental results only.

Apart from the RMS and maximum values, we are interested in a characterization of the disturbances impact on the energy of the control error and control effort. The total energy of a signal $u(t)$ is given by [9]

$$\|u\|_2^2 = \int_{-\infty}^{\infty} u(t)^2 \mathrm{d}t. \tag{6.3}$$

In order to compare the signal energy of experiments with different duration, it can be normalized by the energy of the input (disturbance d_u). For this purpose, we make use of the signal-to-noise ratio (SNR)

$$e_{\mathrm{SNR}} = \frac{\sum_{n=1}^{N} e_n^2}{\sum_{n=1}^{N} d_{u,n}^2} \quad \text{and} \quad u_{\mathrm{SNR}} = \frac{\sum_{n=1}^{N} \left(u_n - u_{\mathrm{ss}}\right)^2}{\sum_{n=1}^{N} d_{u,n}^2} \tag{6.4}$$

for the control error and control effort, respectively, with $d_{u,n} = d_u(nT_\mathrm{s})$. Note that we subtract the stationary part u_ss from the control signal which is necessary to keep the load in the middle of the actuator range ($x_{0,\mathrm{d}}$).

Table 6.3: Signal-to-noise ratios in dB to characterize the effect of the disturbance on the signal energy, i.e. control error e and control signal u.

		Dominant Delay τ_1			**Small Delay τ_2**		
Contr.	**Metric**	$\tau = 0.9\tau_1$	$\tau = \tau_1$	$\tau = 1.1\tau_1$	$\tau = 0.9\tau_2$	$\tau = \tau_2$	$\tau = 1.1\tau_2$
$C_{\infty,i}$	e_{SNR}	−48.604	−48.182	−48.031	−50.405	−50.233	−49.993
	u_{SNR}	−12.046	−11.318	−11.155	−9.761	−9.710	−9.469
$C_{\mathrm{FO},i}$	e_{SNR}	−48.534	−48.553	−48.192	−50.497	−50.144	−49.690
	u_{SNR}	−11.512	−11.319	−10.789	−11.576	−11.249	−10.410

The results are summarized in Table 6.3. Obviously, u_{SNR} is significantly larger than e_{SNR} which is natural since it is used to counteract the disturbance. The differences between the controllers are rather small for each case of τ_i, $i \in \{1,2\}$, there are however visible deviations between the two cases. As expected for the error metric, it decreases for smaller delays. This is not necessarily the case for the impact of the disturbance on the input, which can be seen at u_{SNR} for the nominal values $\tau = \tau_i$. To sum up, in the case of the dominant delay τ_1 the controller $C_{\infty,1}$ performs the best in terms of the control effort energy, whereas $C_{\mathrm{FO},2}$ yields the best results for the small delay τ_2.

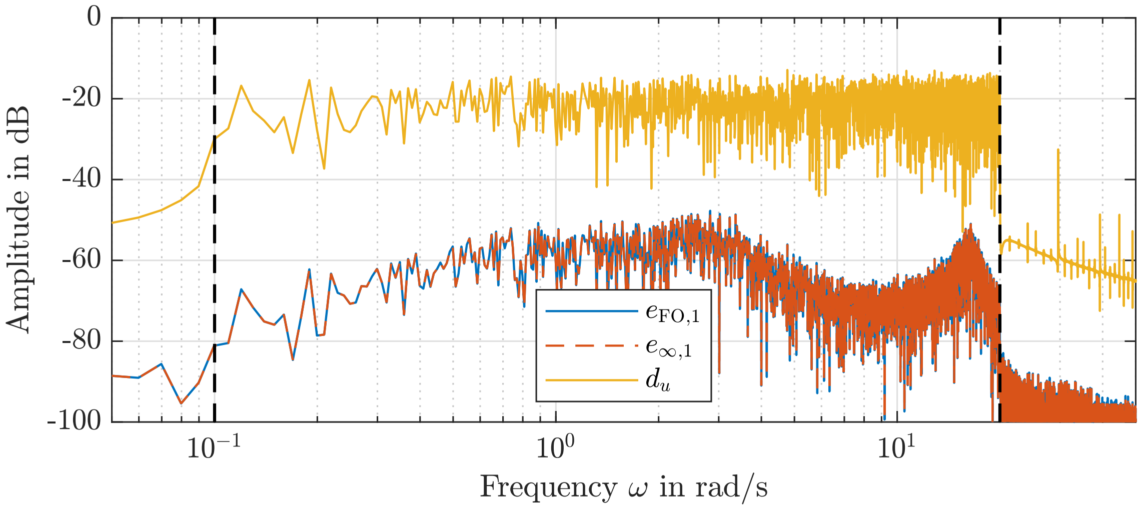

Figure 6.2: Frequency spectra of the input disturbance and the control errors for experiments with both controllers $C_{\mathrm{FO},1}$ and $C_{\infty,1}$ and the nominal value of the dominant communication delay $\tau = \tau_1$. The dashed black lines indicate the frequency spectrum of the input disturbance Ω_{d} which is used to calculate the metrics in Table A.3.

Finally, consider the frequency spectrum of the disturbance in Figure 6.2. As stated above, it is restricted to the frequency range $\omega \in \Omega_{\mathrm{d}}$ and has a constant amplitude. The applied jitter-signal has a significantly higher frequency and is therefore not visible in this figure. It can be seen in Figure A.8 in Appendix A.3.1, where the frequency spectra for the small delay are shown as well (see Figures A.9a and A.9b).

Using the disturbance d_u, we can qualitatively reproduce the magnitude plot of the input sensitivity in Figure 5.10. The error spectra can be utilized to characterize further evaluation metrics in terms of the maximum $\max_\omega |e(\omega)|$, mean $\mu(|e(\omega)|)$ and minimum $\min\limits_{\omega} |e(\omega)|$ for $\omega \in \Omega_{\mathrm{d}}$. These lead to similar results as the SNRs above and thus can be found in Table A.3 in Appendix A.3.1.

6.2 Tracking Performance

In order to evaluate the tracking performance, sufficiently smooth set-point changes from r_0 to r_1 are considered in terms of the transition polynomial

$$r(t) = r_0 + (r_1 - r_0) \left(\sum_{k=4}^{7} \frac{840\,(-1)^{k-2}}{k\,(k-2)!\,(7-k)!} \left(\frac{t}{T_{\mathrm{t}}} \right)^{k} \right) \tag{6.5}$$

with transition time $T_{\mathrm{t}} = 2\,\mathrm{s}$. The seventh order polynomial yields vanishing derivatives at the boundaries for up to order three.

To make use of the whole actuator range, the four set-point changes in Table 6.4 are considered, where `l`, `m` and `h` abbreviate the positions *low* (5 mm), *middle* (10 mm) and *high* (15 mm), respectively.

Table 6.4: Set-point changes with r_0 and r_1 used in the transition polynomial (6.5).

r_i in mm	`mh`	`hm`	`ml`	`lm`
r_0	10	15	10	5
r_1	15	10	5	10

In order to allow quantitative evaluations, each set-point change is repeated three times leading to the time responses depicted in Figure 6.3. It can be seen that the set-point response differs between the directions, however the results seem reproducible.

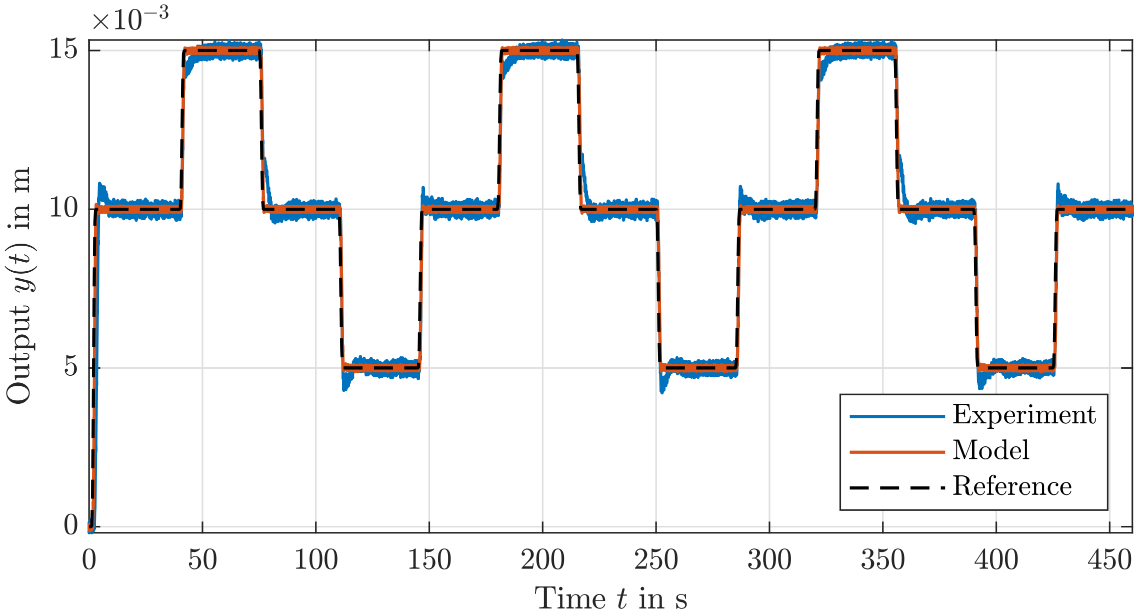

Figure 6.3: Exemplary experimental and simulation results using $C_{\mathrm{FO},1}$ for the nominal value of the dominant communication delay $\tau = \tau_1$.

The following discussions are structured as follows. First, we consider the set-point change `lm` to exemplary evaluate the tracking performance of the different controllers for both cases of the nominal communication delay τ_i. The evaluation addresses deviations from the nominal delay. Second, we look at the differences between the set-point changes. For clarity reasons, the communication delay variations are not considered.

6.2.1 The Set-Point Change `lm`

Figure 6.4 presents exemplary simulation and experimental results for the set-point change `lm`, i.e. from $r_0 = 5\,\mathrm{mm}$ to $r_1 = 10\,\mathrm{mm}$ using both controllers for the dominant delay τ_1. Due to little variations in the simulation results only, these are restricted to the nominal case $\tau = \tau_1$ (red dashed line). The overshooting of the 2DOF $\mathcal{H}_\infty$ controller $C_{\infty,1}$ of (5.8) does not change for a variation of the communication delay. Hence, it is robust against delay uncertainties, however significantly slower. Thanks to the more aggressive feedforward pat (5.15) of the fractional-order controller $C_{\mathrm{FO},1}$ of (5.17), it outperforms the $\mathcal{H}_\infty$ controller.

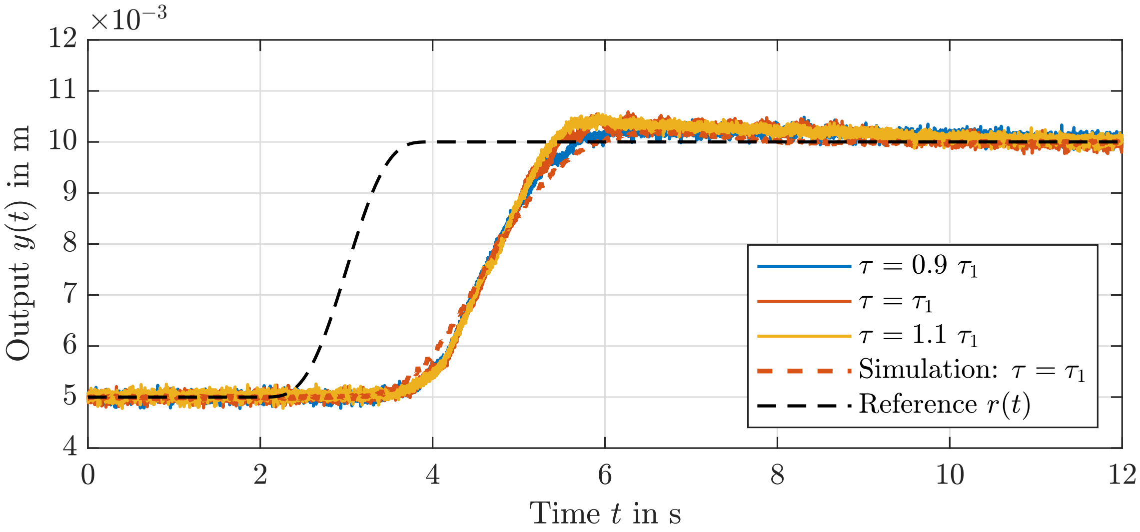

(a) Closed-loop response using $C_{\infty,1}$ (5.8).

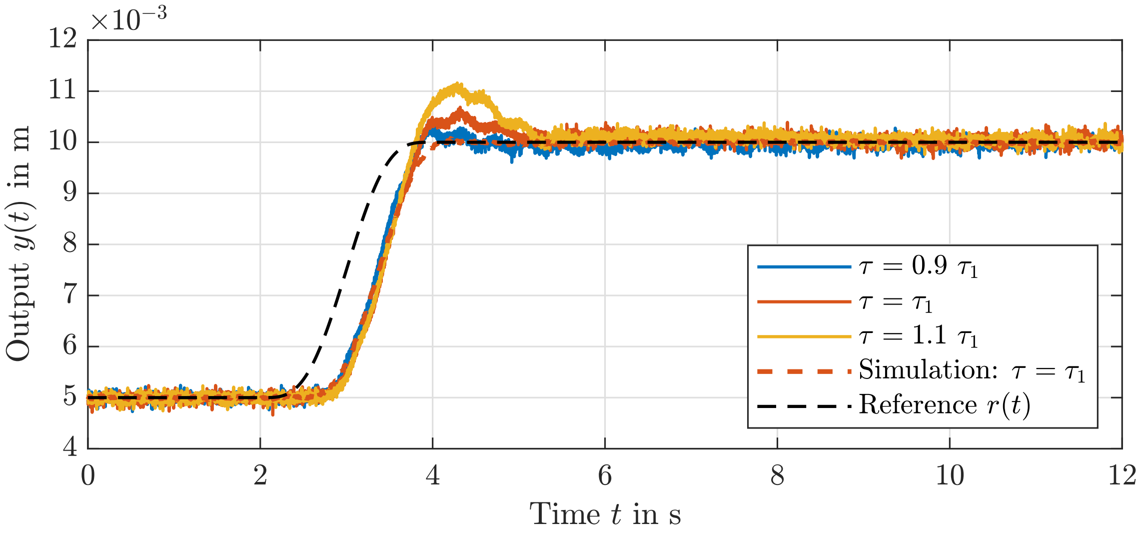

(b) Closed-loop response using $C_{\mathrm{FO},1}$ (5.17) with prefilter (5.14).

Figure 6.4: Time responses to the set-point change for both controllers and the dominant delay τ_1 with initial conditions $x_{0,\mathrm{t}} = \begin{bmatrix} 0.005 & 0 & 0.005 & 0 \end{bmatrix}^\top$ and a variation of the communication delay by $\pm 10\,\%$.

The sensitivity to delay variations is naturally caused by the explicit time-shift of the reference signal in $u^*(t)$ (see (5.14)). This confirms the expectations from the different feedforward paths (see Figure 5.4) discussed in Section 5.3.

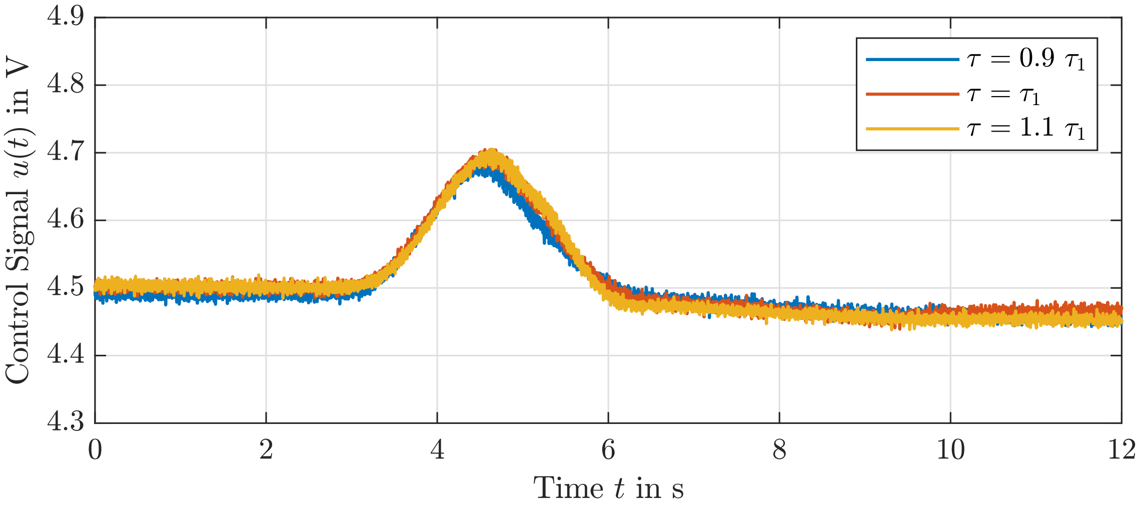

(a) Control signal of $C_{\infty,1}$ for the response in Figure 6.4a.

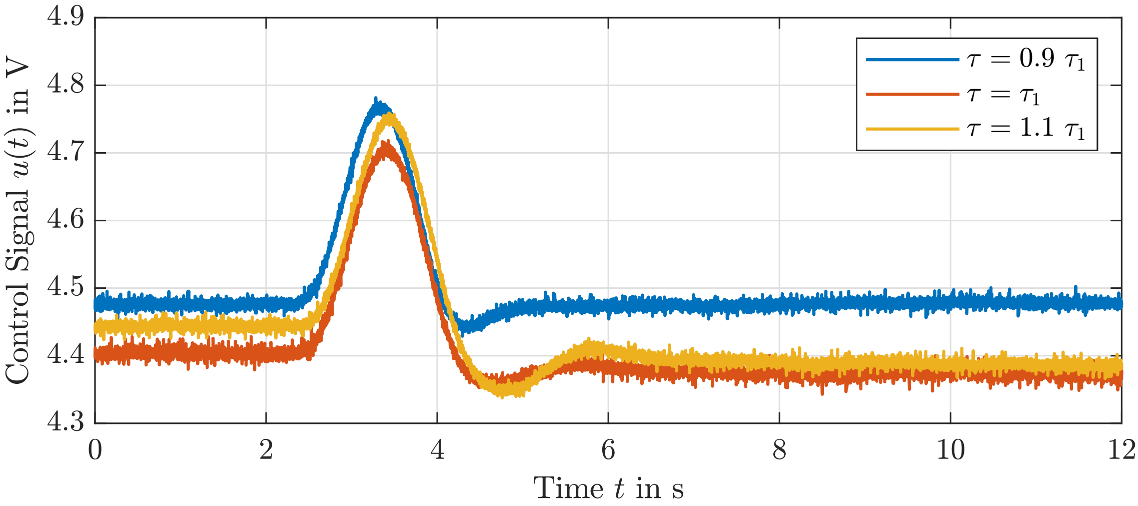

(b) Control signal of $C_{\mathrm{FO},1}$ for the response in Figure 6.4b.

Figure 6.5: Control signals applied for the outputs in Figure 6.4 with the dominant communication delay τ_1.

Figure 6.5 presents the control signals leading to the outputs of Figure 6.4. The slow, however robust action of the $\mathcal{H}_\infty$ controller is clearly visible in Figure 6.5a. The more direct and aggressive feedforward action of the fractional-order controller, as well as the sensitivity to time delay uncertainties can be seen in Figure 6.5b.

If we consider the results for the small communication delay τ_2 in Figure A.10, the same qualitative conclusions can be drawn. Due to the higher bandwidth, the control signals are significantly more affected by noise (see Figure A.11). Still, both the output as well as the control action are less affected by time delay variations, as it is expected for the less dominant delay.

For the quantitative evaluation we utilize the metrics defined in (6.1) and (6.2), averaged over three set-point changes. Furthermore, we make use of the integral of time-multiplied absolute error (ITAE) [50] in its discrete version

$$e_{\text{ITAE}} = \sum_{n=1}^{N_T} t_n \, |e_n| \tag{6.6}$$

with $t_n = nT_s$. This metric highlights the speed of convergence, hence significantly greater values are expected for $C_{\infty,i}$. A time horizon of 20 s is used for the evaluation metrics e_{RMS}, e_{ITAE}, $|e_{\max}|$ and $|u_{\max}|$. Finally, we are interested in the settling time T_{IAE} and use the integral of absolute error (IAE) [50] for $t < T_{\text{IAE}}$:

$$e_{\text{IAE}} = \sum_{n=1}^{N_T} |\tilde{e}_n| \tag{6.7}$$

with $N_T = \frac{T_{\text{IAE}}}{T_s}$, $\tilde{e}_n = \tilde{e}(nT_s)$ and $|\tilde{e}(t)| < 0.25\,\text{mm}\ \forall t > T_{\text{IAE}}$. The maximum deviation of 0.25 mm corresponds to 5 % of the step-size $\Delta r = |r_1 - r_0|$. Due to the upper bound on the absolute error, this metric is sensitive to outliers. Thereore, the control error e is processed with a three-point moving-median filter resulting in $\tilde{e}$.

Table 6.5: Quantitative evaluation of the tracking experiments.

		Dominant Delay τ_1			**Small Delay τ_2**		
Contr.	**Metric**	$\tau = 0.9\tau_1$	$\tau = \tau_1$	$\tau = 1.1\tau_1$	$\tau = 0.9\tau_2$	$\tau = \tau_2$	$\tau = 1.1\tau_2$
$C_{\infty,i}$	e_{RMS}	1.220	1.215	1.214	0.780	0.787	0.792
	e_{ITAE}	138.994	133.097	152.730	68.983	66.144	70.730
	e_{IAE}	45.853	45.004	46.139	22.874	22.662	22.820
	T_{IAE}	8.007	7.192	8.708	2.785	2.670	2.690
	$\lvert e_{\max}\rvert$	4.911	4.934	4.907	3.790	3.932	3.963
	$\lvert u_{\max}\rvert$	5.030	5.047	5.061	5.240	5.248	5.252
$C_{\text{FO},i}$	e_{RMS}	0.104	0.149	0.221	0.089	0.083	0.098
	e_{ITAE}	85.912	64.560	64.295	37.195	37.444	39.710
	e_{IAE}	5.563	4.630	6.486	1.584	1.564	1.852
	T_{IAE}	15.394	4.203	3.826	1.711	1.871	1.857
	$\lvert e_{\max}\rvert$	0.474	0.784	1.205	0.647	0.582	0.712
	$\lvert u_{\max}\rvert$	4.947	4.789	4.813	5.272	5.248	5.267

The results are summarized in Table 6.5 where the values for e_{RMS} and $|e_{\max}|$ are given in mm, $|u_{\max}|$ in V and T_{IAE} in s. The calculation of the remaining metrics e_{ITAE} and e_{IAE} is based on e_n in m and t_n in s. At first glance, in accordance with the time plots, $C_{\text{FO},i}$ with prefilter (5.14) outperforms the 2DOF $\mathcal{H}_\infty$ controller in almost all metrics. This is mainly caused by the different feedforward actions as discussed in Section 5.3. For a structured evaluation, we shortly discuss each metric separately:

e_{RMS} The RMS error for the first 20 s after each set-point change yields similar conclusions as the time responses in Figures 6.4 and A.10. That is, the error using $C_{\infty,i}$ is an order of magnitude greater compared to $C_{\mathrm{FO},i}$. However the deviations are smaller for a variation of the communication delay.

e_{ITAE} As stated above, this metric highlights the speed of convergence, therefore significant differences can be observed between the controllers and between the nominal delays τ_i. Due to the weight t the overshoot has only a little impact, as it can be seen at $C_{\mathrm{FO},1}$. Even if the RMS error is minimal for this controller and $\tau = 0.9\,\tau_1$, it shows a significantly worse ITAE indicating long-term deviations.

e_{IAE} and T_{IAE} The combination of the settling time with the IAE yields interesting conclusions, as fast convergence does not necessarily result in a small IAE. This can be seen at $C_{\mathrm{FO},1}$ for $\tau = 1.1\,\tau_1$. As suggested by the time response, the overshoot leads to a large error even for the minimal settling time. Next, consider the significantly increased highlighted value. Thus, in accordance with the high value of e_{ITAE}, the control error persists for a long duration. Looking at e_{IAE}, it can be seen that the best values are achieved for the nominal delay $\tau = \tau_i$ for all controllers.

$|e_{\mathrm{max}}|$ The maximum absolute error of the $\mathcal{H}_\infty$ controller is large however robust against time delay variations. This is not the case for $C_{\mathrm{FO},i}$ where it significantly increases for an increasing time delay.

$|u_{\mathrm{max}}|$ As expected from the explicit time shift of the reference signal in $u^*(t)$ of (5.14) and the slower feedback control C_{FO}, the maximum control effort increases for any deviation from the nominal time delay τ_i. The $\mathcal{H}_\infty$ controller, in contrast, only shows small deviations and the best performance for the smallest communication delay.

Finally, consider the time responses to a step-like reference signal in Figure 6.6, i.e. a transition time of $T_{\mathrm{t}} = 0.2$ s. Obviously, the aggressive feedforward action based on the model-inverse (see (5.15)) leads to a saturation of the control signal, which is not the case for the $\mathcal{H}_\infty$ controller. This further highlights the differences between the two controllers in the feedforward path. For this simulation, the nominal value of the dominant communication delay $\tau = \tau_1$ is used. However, similar results can be obtained for $\tau = \tau_2$.

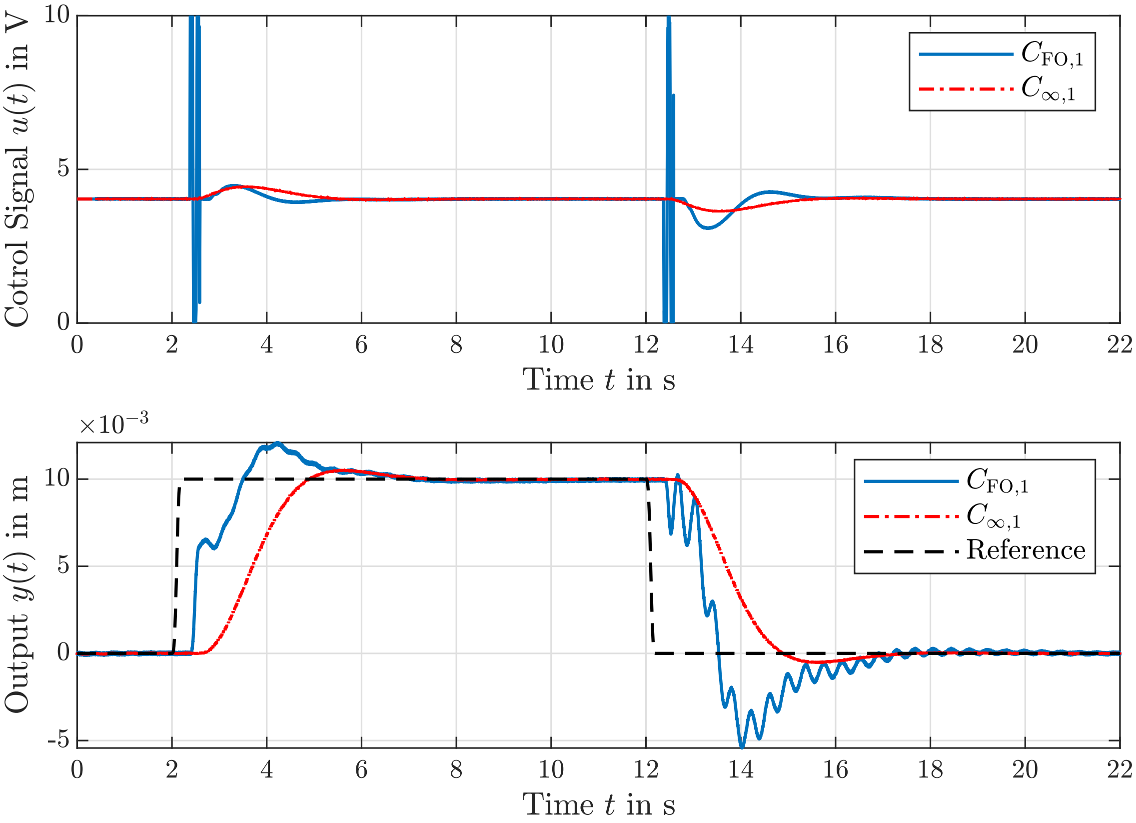

Figure 6.6: Simulation results for a step-like reference signal, i.e. a transition with transition time $T_{\mathrm{t}} = 0.2$ s.

6.2.2 Entire Experiment

After having discussed the single set-point change `lm` for communication delay variations, we now consider the nominal values of the delays only, i.e. $\tau = \tau_i$, $i \in \{1, 2\}$. Furthermore, we restrict the following discussion to the RMS error, as it is a broadly used and an intuitive evaluation metric. Similar results can be derived for the remaining evaluation metrics, see Appendix A.3.2.

Figure 6.3 at the beginning of this section shows differences between the set-point changes described in Table 6.4. The RMS error e_{RMS} is utilized to characterize these differences leading to the histograms in Figure 6.7. As discussed in the previous subsection, there are significant differences between the two controllers $C_{\mathrm{FO},i}$ and $C_{\infty,i}$. Furthermore, the impact of the communication delay τ_i is clearly visible in the histograms. Finally, it can be seen that the differences between the set-point changes are systematic and the previously considered set-point change `lm` yields the best overall performance. In contrast, the largest error using $C_{\mathrm{FO},i}$ with classical feedforward is observed for `hm` ($r_0 = 15\,\mathrm{mm}$), followed by the opposite set-point change `mh`. This is not the case using the 2DOF $\mathcal{H}_\infty$ controller. Therefore, it is

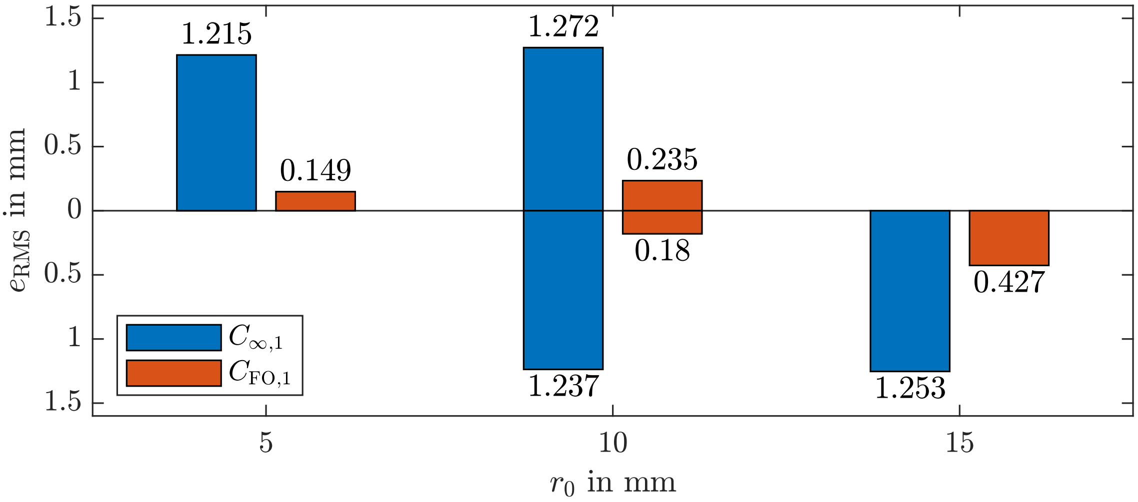

(a) Dominant communication delay $\tau = \tau_1$.

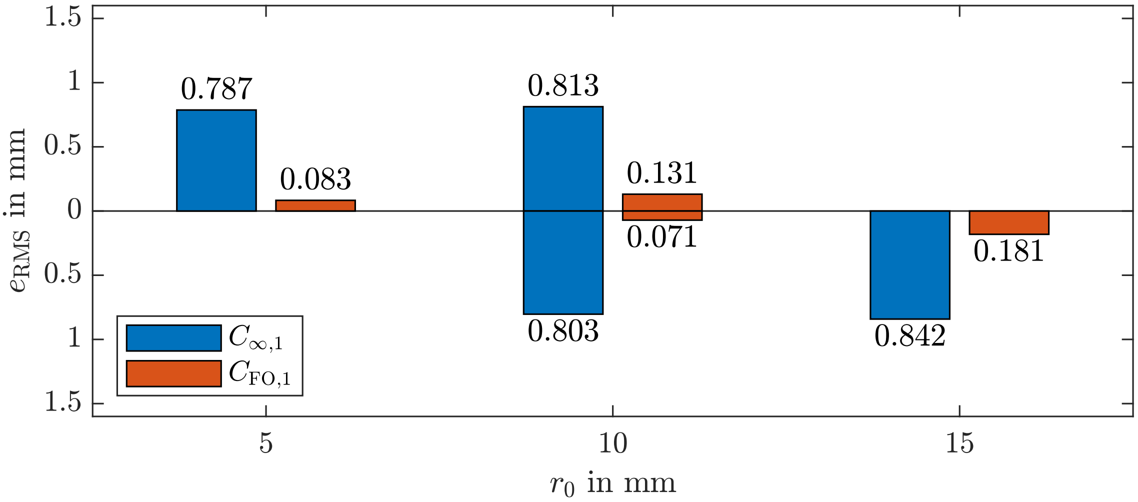

(b) Small communication delay $\tau = \tau_2$.

Figure 6.7: Histogram of the RMS error e_{RMS} for $\tau = \tau_i$ and both controllers. The bar orientation shows the direction of the set-point changes, e.g. the bars at the left-hand side ($r_0 = 5\,\mathrm{mm}$) correspond to the above-discussed set-point change `lm`.

most likely caused by the aggressive feedforward action based on the model-inverse and the model fit is expected to be better in the lower range.

Furthermore, an analysis of the control signal u reveals a systematic change of the system parameters which may arise over time and use of the experimental setup. For this purpose consider Figure 6.8. It shows the necessary steady-state input voltage to compensate the gravitational forces, which obviously differs from the identification procedure in Section 4.2 and would lead to a change of the state-dependent input gain $k_u(x_1)$. Note that these changes are not caused by the necessary model gain adjustment of $k_m = 1.3$, since it is pre-compensated with k_m^{-1}.

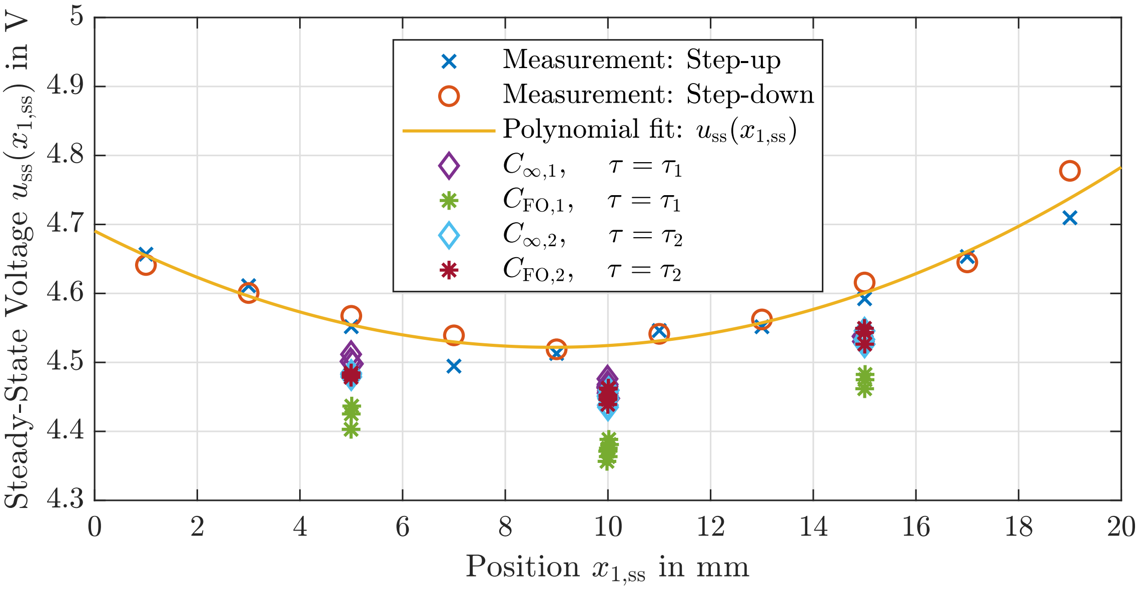

Figure 6.8: Recalculation of the steady-state input voltage to compensate the gravitational forces based on the tracking experiments for the nominal values of the communication delay τ_i.

6.3 Further Remarks

At the end of this chapter, two interesting observations are mentioned. First, consider the applied jitter-signal, i.e. a square wave with frequency $\omega_j = 450$ rad/s. This frequency almost coincides with the fundamental frequency of the process noise $f_1 = 74\,\text{Hz}$, i.e. $\omega_{\text{noise}} = 2\pi f_1 = 464.96\,\text{rad/s} \approx 450$ rad/s $= \omega_j$.

Second, we consider the disturbance attenuation experiments. Before having found the necessary jitter-signal to overcome the stiction-like phenomenon, few experiments went unstable. This only applies to the large delay τ_1, as the margins for both controllers are significantly higher for the small delay. It happens more often using the fractional-order loop-shaping controller $C_{FO,1}$. Comparing the maximum control effort $|u_{\max}|$ of both controllers for the dominant delay, $C_{FO,1}$ shows larger values in each case of τ, see Table 6.2a, which explains this observation. The instability occurs at $t_{\max} \approx 218\,\text{s}$ where $d_u(t_{\max}) = 0.663\,\text{V} = \max_t |d_u(t)|$. Exemplary results are depicted in Figure 6.9 (next page). It shows the high value of the disturbance that renders the process unstable, in combination with the large control signal at this moment. Since the actuator position is not measured, the stiction-like phenomenon cannot be shown here. However during the experiments it is clearly visible and most likely the reason for the instability. The significantly better fit of the simulation and experimental results with jitter-signal supports this assumption, see e.g. Figures 6.1 and A.7.

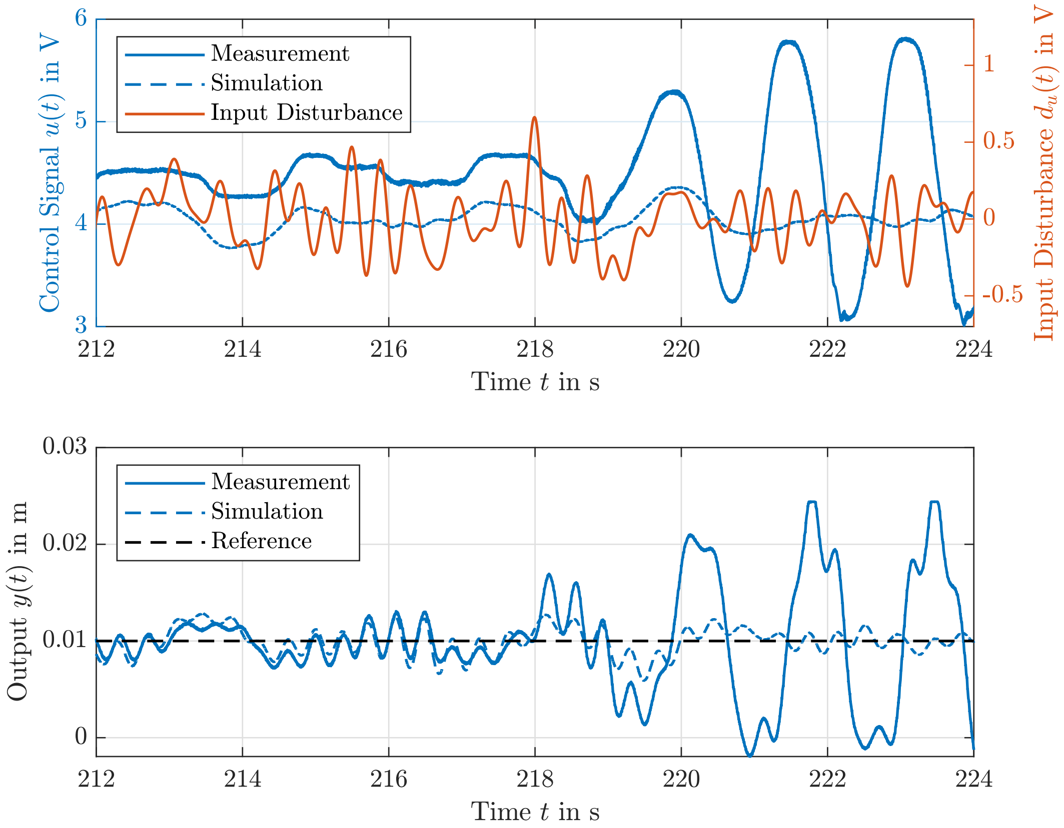

Figure 6.9: Unstable disturbance attenuation experiment without jitter-signal using $C_{\mathrm{FO},1}$ for $\tau = 0.9\ \tau_1$.

7 Conclusions and Perspectives

In this work, the partial pole-zero cancellation of integer-order right-half plane zeros and poles is investigated and applied within a loop-shaping controller design procedure. We start with a detailed analysis of fractional-order pseudo poles and zeros in the frequency domain, as these remain from partial cancellation. Furthermore, the fractional-order cancellation terms itself are considered and it is shown that these only consist of stable roots and therefore do not affect the overall systems stability. The concept to partially cancel a single integer-order zero/pole is extended to a pair of conjugate complex zeros or poles. Here, we do not restrict us to those located in the right-half plane, but also investigate partially canceled stable, however low-damped poles.

Apart from classical (i.e. *explicit*) pseudo zeros and poles, the concept is extended to their *implicit* counterparts (as a part of the fractional-order lead-lag compensator). A comparison of these strategies within the above-mentioned scope reveals mainly two significant differences. On the one hand, the amplitude response of an explicit pseudo zero drops around the transitional frequency, which does not apply to the implicit term. On the other hand, the phase drop of the explicit pseudo zero occurs at lower frequencies already. Hence, for partial cancellation of an integer-order non-minimum phase zero, which yields a lower-order (implicit) pseudo zero, the implicit cancellation is preferred. Compared to an integer-order pseudo compensation by the mirrored pole, we significantly reduce the phase lag as well as the loss of magnitude slope with both strategies.
Considering a pair of stable poles, we show that the explicit cancellation of the principal roots, i.e. the pseudo poles closest to the stability border, entirely erases the oscillatory part. This applies to both the peak in the frequency response as well as an overshooting in the time-domain. However, the implicit cancellation only reduces these effects.

An analysis of the relevant sensitivity functions in a standard control loop confirms that partial cancellation of right-half plane poles does not violate the internal stability, in contrast to the integer-order unstable pole-zero cancellation. Exemplary simulation results show that partial cancellation of non-minimum phase zeros can significantly reduce the step-response undershoot.

Therefore, the proposed concept can be applied as a tool for intuitive loop-shaping, which is used in the second part of this thesis. We consider a two-mass oscillator with non-collocated actuation and measurement and derive a linear time-invariant fourth-order model, which overestimates the damping. In addition to that, the nonlinearity of the actuator is identified in terms of a state-dependent input gain and a process noise model is determined. To simulate a possible essential communication delay, we artificially inject a time delay and investigate two cases of different dominance.

We design and compare, for each of these cases, two robust controllers including feedforward action. On the one hand, fractional-order loop-shaping with classical feedforward (i.e. based on the mode-inverse) is used to design a PI-lead based controller. The Padé-approximation of the time delay leads to a non-minimum phase zero that is addressed by implicit partial cancellation. On the other hand, $\mathcal{H}_\infty$ controller synthesis methods are used to determine a reference controller. For comparibility, the controllers are designed to yield a similar open-loop crossover frequency, gain for low frequencies as well as controller order.

To evaluate the robust controllers, disturbance attenuation and tracking experiments as well as simulations are conducted with uncertainties in the communication delay. We achieve comparable results, where the simulations only show minor deviations from the measurements. Considering the nominal delays, the disturbance attenuation capabilities are very similar for both control structures, as expected from the corresponding sensitivity functions. However, the $\mathcal{H}_\infty$ controller is more robust to delay uncertainties. The tracking experiments reveal major differences between the controllers, where the loop-shaping based controller outperforms the $\mathcal{H}_\infty$ controller in all relevant cases. This is caused by the differences in the feedforward paths, i.e. the feedforward-action based on the model-inverse is more aggressive. Comparing the weighted sensitivities of the controllers reveals that these results cannot be achieved with the $\mathcal{H}_\infty$ control structure in the present case. However, it shows to be less sensitive to delay uncertainties.

Future Work

The future work can be categorized into three parts. The theoretical derivations in this thesis are restricted to a partial cancellation of non-integer order $\alpha = \nu^{-1}$ where ν is a positive integer. Investigations for any rational $\alpha = \mu/\nu \in (0, 1)$, $\mu, \nu \in \mathbb{N}$ might be interesting, since in these cases we do not cancel everything but the principal ν-th root and possibly reduce the phase lag. Similar to the case of stable, low-damped poles, it might be sufficient to cancel only those pseudo zeros/poles closest to the stability limit, i.e. those $z_i \in \mathbb{C}_+$ in the sector $\alpha\,\frac{\pi}{2} < |\arg(z_i)| < \alpha\,\pi$. Furthermore, considering a conjugate complex pair of stable poles, a fractional-order notch filter might enhance an intuitive fractional-order loop-shaping controller design. In the scope of this thesis, we only apply partial cancellation, however the relative damping as a further degree of freedom may be promising. Finally, it may be effective to incorporate the partial cancellation terms into controller tuning strategies based on optimization problems resulting in an optimal order of partial cancellation.

This leads to the second part, the plant model and controller design. It might be interesting and effective for control to model or estimate the stiction-like phenomenon of the actuator. To enhance the performance of the $\mathcal{H}_\infty$ controller, different design procedures may be applied, e.g. $\mathcal{H}_\infty$ loop-shaping [39] or predictor-based approaches [51]. Regarding the fractional-order loop-shaping controller, more robustness is expected if we incorporate for instance a disturbance observer [17] into the control structure.

Finally, note that the proposed partial cancellation is applied to the Padé-approximation of a time delay, where the delay is artificially injected. An application to a plant that naturally contains a right-half plane zero/pole or low-damped poles might be interesting, e.g. an inverted pendulum.

Bibliography

[1] Akribis. *Voice Coil Motor User Manual.* 2018.

[2] K. Åström. “Limitations on Control System Performance”. In: *European Journal of Control*, Vol. 6, No. 1 (2000), pp. 2–20.

[3] BALLUFF. *Datasheet BAW003K.* BAW MKK-050.19-S4. 2021.

[4] I. N. Bronštejn and K. A. Semendjajew. *Taschenbuch der Mathematik.* Harri Deutsch, 1985.

[5] Y. Chen, I. Petras, and D. Xue. “Fractional order control - A tutorial”. In: *American Control Conference.* 2009, pp. 1397–1411.

[6] R. Y. Chiang and M. G. Safonov. “H_∞ robust control synthesis for an undamped, non-colocated spring-mass system”. In: *American Control Conference.* 1990, pp. 966–967.

[7] S. Das. *Functional fractional calculus.* Springer, 2011.

[8] J. Doyle, K. Glover, P. Khargonekar, and B. Francis. “State-space solutions to standard H_2 and H_∞ control problems”. In: *IEEE Transactions on Automatic Control*, Vol. 34, No. 8 (1989), pp. 831–847.

[9] J. Doyle, B. Francis, and A. Tannenbaum. *Feedback Control Theory.* Macmillan Publishing, 1990.

[10] O. Föllinger. *Regelungstechnik: Einführung in die Methoden und ihre Anwendung.* Hüthig, 1994.

[11] K. Glover and J. C. Doyle. “State-space formulae for all stabilizing controllers that satisfy an H_∞-norm bound and relations to relations to risk sensitivity”. In: *Systems & Control Letters*, Vol. 11, No. 3 (1988), pp. 167–172.

[12] D.-W. Gu, P. H. Petkov, and M. M. Konstantinov. *Robust Control Design with MATLAB®.* 2005.

[13] T. Hägglund. “A friction compensator for pneumatic control valves”. In: *Journal of Process Control*, Vol. 12, No. 8 (2002), pp. 897–904.

[14] M. Hofer and R. D’Andrea. “Design, Modeling and Control of a Soft Robotic Arm”. In: *IEEE/RSJ International Conference on Intelligent Robots and Systems.* 2018, pp. 1456–1463.

[15] S. HosseinNia. “Fractional hybrid control systems: Modeling, analysis and applications to mobile robotics and mechatronics”. In: *Ph. D. dissertation.* Universidad de Extremadura, 2013.

[16] A. Isidori. *Nonlinear Control Systems.* Springer, 2013.

[17] N. H. Jo, H. Shim, and Y. I. Son. “Disturbance observer for non-minimum phase linear systems”. In: *International Journal of Control, Automation and Systems*, Vol. 8, No. 5 (2010), pp. 994–1002.

[18] H. Koivo and J. Tanttu. “Tuning of PID conrollers: Survey of SISO and MIMO techniques”. In: *Intelligent tuning and adaptive control.* Elsevier, 1991, pp. 75–80.

[19] A. Kojima and S. Ishijima. “Robust controller design for delay systems in the gap-metric”. In: *IEEE Transactions on Automatic Control*, Vol. 40, No. 2 (1995), pp. 370–374.

[20] E. C. Levy. “Complex-curve fitting”. In: *IRE Transactions on Automatic Control*, Vol. 4, No. 1 (1959), pp. 37–43.

[21] R. Magin. “Fractional Calculus in Bioengineering”. In: *Critical Reviews™ in Biomedical Engineering*, Vol. 32, No. 1–4 (2004).

[22] N. K. Z. Mahani, A. K. Sedigh, and F. M. Bayat. “Performance evaluation of non-minimum phase linear control systems with fractional order partial pole-zero cancellation”. In: *Asian Control Conference.* 2013, pp. 1–4.

[23] F. Mainardi and R. Gorenflo. “On Mittag-Leffler-type functions in fractional evolution processes”. In: *Journal of Computational and Applied Mathematics*, Vol. 118, No. 1-2 (2000), pp. 283–299.

[24] D. Matignon. “Stability Results For Fractional Differential Equations With Applications To Control Processing”. In: *Computational Engineering in Systems Applications.* 1996, pp. 963–968.

[25] G. Meinsma and H. Zwart. “On $\mathcal{H}_\infty$ control for dead-time systems”. In: *IEEE Transactions on Automatic Control*, Vol. 45, No. 2 (2000), pp. 272–285.

[26] F. Merrikh Bayat and F. Bayat. “Method for Undershoot-Less Control of Non-Minimum Phase Plants Based on Partial Cancellation of the Non-Minimum Phase Zero: Application to Flexible-Link Robots”. In: *arXiv:1401.0106* (2013).

[27] F. Merrikh-Bayat. “Fractional-order unstable pole-zero cancellation in linear feedback systems”. In: *Journal of Process Control*, Vol. 23, No. 6 (2013), pp. 817–825.

[28] L. Mirkin and G. Tadmor. “H_∞ Control of System With I/O Delay: A Review of Some Problem-Oriented Methods”. In: *IMA Journal of Mathematical Control and Information*, Vol. 19, No. 1–2 (2002), pp. 185–199.

[29] C. A. Monje, Y. Chen, B. M. Vinagre, D. Xue, and V. Feliu. *Fractional-order Systems and Controls.* Springer, 2010.

[30] A. Oustaloup, P. Melchior, P. Lanusse, O. Cois, and F. Dancla. “The CRONE toolbox for Matlab”. In: *IEEE International Symposium on Computer-Aided Control System Design.* 2000, pp. 190–195.

[31] A. Oustaloup, F. Levron, B. Mathieu, and F. M. Nanot. “Frequency-band complex noninteger differentiator: characterization and synthesis”. In: *IEEE Transactions on Circuits and Systems I: Fundamental Theory and Applications*, Vol. 47, No. 1 (2000), pp. 25–39.

[32] H. Padé. “Sur la représentation approchée d’une fonction par des fractions rationnelles”. In: *Annales scientifiques de l’École normale supérieure*, Vol. 9 (1892), pp. 3–93.

[33] I. Podlubny. *Fractional Differential Equations: An Introduction to Fractional Derivatives, Fractional Differential Equations, to Methods of Their Solution and Some of Their Applications.* Acad. Press, 1999.

[34] V. Pommier-Budinger, Y. Janat, D. Nelson-Gruel, P. Lanusse, and A. Oustaloup. “Fractional robust control with ISO-damping property”. In: *American Control Conference.* 2008, pp. 4954–4959.

[35] H.-F. Raynaud and A. Zergaïnoh. “State-space representation for fractional order controllers”. In: *Automatica*, Vol. 36, No. 7 (2000), pp. 1017–1021.

[36] M. Ruderman. “One-parameter robust global frequency estimator for slowly varying amplitude and noisy oscillations”. In: *Mechanical Systems and Signal Processing*, Vol. 170 (2022), p. 108756.

[37] M. Ruderman. “Robust output feedback control of non-collocated low-damped oscillating load”. In: *Mediterranean Conference on Control and Automation.* 2021, pp. 639–644.

[38] S. Seyedtabaii. “A Modified FOPID Versus H_∞ and μ-Synthesis Controllers: Robustness Study”. In: *International Journal of Control, Automation and Systems*, Vol. 17, No. 3 (2019), pp. 639–646.

[39] S. Skogestad and I. Postlethwaite. *Multivariable Feedback Control.* John Wiley & Sons, 2001.

[40] Speedgoat. *Baseline real-time target machine.* Last Visited 02/24/2022. URL: `https://www.speedgoat.com/products-services/speedgoat-real-time-target-machines/baseline`.

[41] A. Tepljakov, E. Petlenkov, and J. Belikov. “FOMCON toolbox for modeling, design and implementation of fractional-order control systems”. In: *Applications in Control.* De Gruyter, 2019, pp. 211–236.

[42] A. Varga. “Balancing free square-root algorithm for computing singular perturbation approximations”. In: *IEEE Conference on Decision and Control.* 1991, pp. 1062–1065.

[43] B. M. Vinagre, I. Podlubny, and V. Feliu. “Some approximations of fractional order operators used in control theory and applications”. In: *Journal of Fractional Calculus and Applied Analysis*, Vol. 3, No. 3 (2000), pp. 231–248.

[44] B. Voß, M. Ruderman, C. Weise, and J. Reger. “Comparison of Fractional-Order and Integer-Order $\mathcal{H}_\infty$ Control of a Non-Collocated Two-Mass Oscillator”. In: *IFAC Symposium on Robust Control Design.* 2022, [submitted].

[45] B. Voß, C. Weise, M. Ruderman, and J. Reger. “Fractional-Order Partial Cancellation of Right-Half Plane Poles and Zeros”. In: *IFAC Symposium on Robust Control Design*. 2022, [submitted].

[46] C. Weise, K. Wulff, and J. Reger. “Extended Fractional-Order Memory Reset Control for Integer-Order LTI Systems and Experimental Demonstration”. In: *IFAC-PapersOnLine*, Vol. 53, No. 2 (2020), pp. 7683–7690.

[47] B. Wie and D. S. Bernstein. “Benchmark problems for robust control design”. In: *Journal of Guidance, Control, and Dynamics*, Vol. 15, No. 5 (1992), pp. 1057–1059.

[48] D. Xue. *Fractional-order control systems : fundamentals and numerical implementations*. De Gruyter, 2017.

[49] S. Yamamoto and I. Hasimoto. “Present status and future needs: the view form Japanese industry”. In: *International Conference on Chemical Process Control*. 1991, pp. 1–28.

[50] S. Zacher and M. Reuter. *Regelungstechnik für Ingenieure*. Springer, 2022.

[51] Q.-C. Zhong. *Robust control of time-delay systems*. Springer, 2006.

[52] K. Zhou. *Robust and optimal control*. Prentice Hall, 1996.

Declaration of Primary Authorship

I hereby declare and confirm that this thesis

Fractional-Order Controller Design with Partial Pole-Zero Cancellation

has been written only by me and without any assistance from third parties. Furthermore, I confirm that no sources have been used in the preparation of this thesis other than those indicated in the thesis itself.

Benjamin Voß

Ilmenau, March 01, 2022

Appendix

A.1 Pseudo Zeros and Pseudo Poles: Calculations and Bode Plots

This part of the appendix covers the necessary calculations leading to the results in Chapter 3. Furthermore, Bode plots are shown for a RHP pseudo pole and a pair of conjugate complex RHP pseudo zeros.

A.1.1 Pseudo Zeros and Poles

The Bode plot of a single pseudo pole for both representations is depicted in Figure A.1.

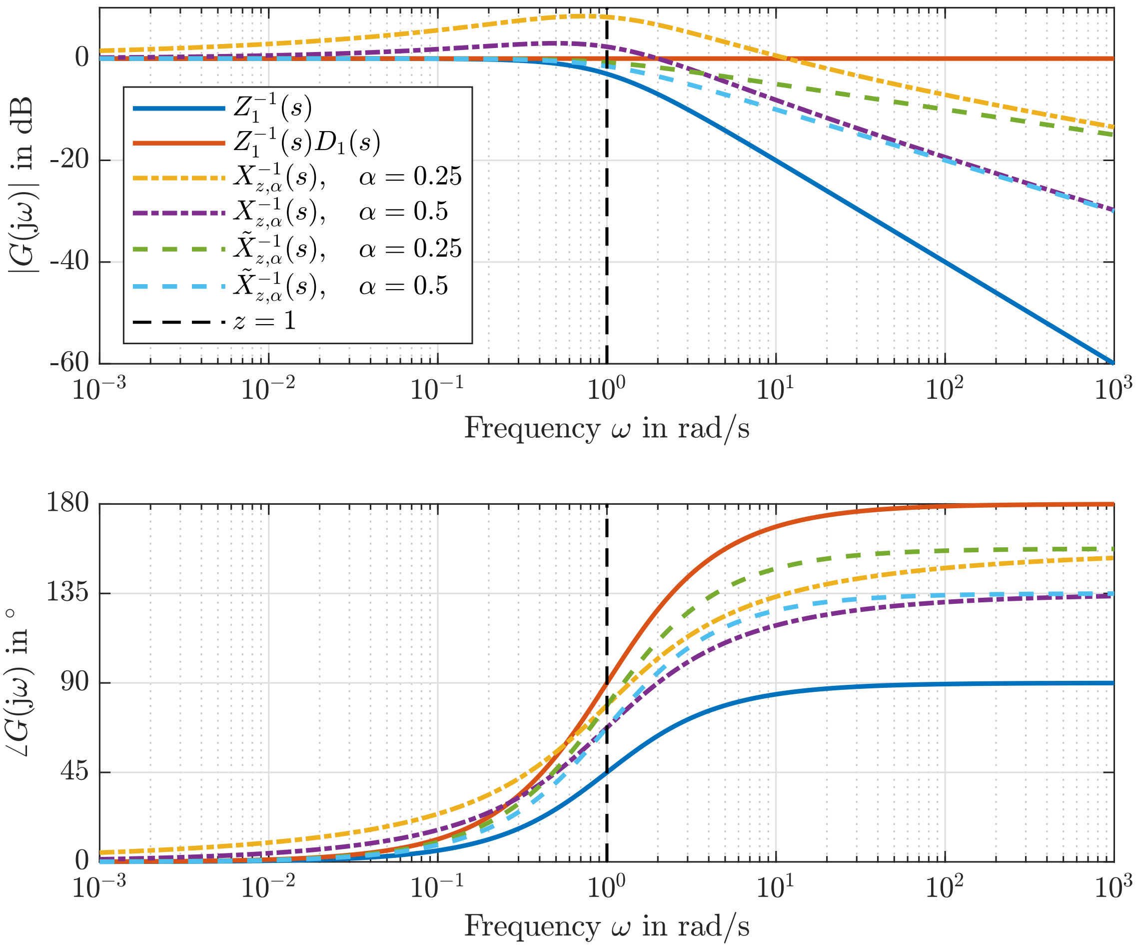

Figure A.1: Bode plot of $X_{z,\alpha}^{-1}$ and $\tilde{X}_{z,\alpha}^{-1}$ for $z = 1$ and $\alpha \in \{0.25, 0.5\}$ opposite to the integer-order term Z_1^{-1} and its pseudo compensation $Z_1^{-1}D_1$.

The phase of a single explicit pseudo zero/pole at the frequency $\omega_{\min}$ can be calculated as

$$\begin{aligned}
\angle\, X^k_{z,\alpha}(\mathrm{j}\omega)\Big|_{\omega_{\min}} &= k\ \arctan\left(\frac{-\left(\frac{\omega}{z}\right)^\alpha \sin\left(\frac{\pi\alpha}{2}\right)}{1-\left(\frac{\omega}{z}\right)^\alpha \cos\left(\frac{\pi\alpha}{2}\right)}\right)\Bigg|_{\omega=\omega_{\min}} , \quad \omega_{\min} = z\left(\cos\left(\frac{\pi\alpha}{2}\right)\right)^{\frac{1}{\alpha}} \\
&= k\ \arctan\left(\frac{-\cos\left(\frac{\pi\alpha}{2}\right)\sin\left(\frac{\pi\alpha}{2}\right)}{1-\cos^2\left(\frac{\pi\alpha}{2}\right)}\right) , \quad 1-\cos^2(x) = \sin^2(x) \\
&= k\ \arctan\left(\frac{-\cos\left(\frac{\pi\alpha}{2}\right)}{\sin\left(\frac{\pi\alpha}{2}\right)}\right) , \quad \frac{-\cos(x)}{\sin(x)} = -\cot(x) = \cot(-x) \\
&= k\ \arctan\left(\cot\left(-\frac{\pi\alpha}{2}\right)\right), \cot(x) = -\tan\left(x+\frac{\pi}{2}\right) = \tan\left(-x-\frac{\pi}{2}\right) \\
&= k\ \arctan\left(\tan\left(\frac{\pi\alpha}{2}-\frac{\pi}{2}\right)\right) \\
&= k\ \frac{\pi}{2}\left(\alpha-1\right)
\end{aligned}$$

and thus results in (3.9) for $k = 1$.

The magnitude at $\omega = z$ in (3.14) can be calculated as

$$\begin{aligned}
\left|X^1_{z,\alpha}(\mathrm{j}\omega)\right|_z &= \sqrt{2-2\cos\left(\frac{\pi\alpha}{2}\right)} = 2\sqrt{\frac{1-\cos\left(\frac{\pi\alpha}{2}\right)}{2}} , \quad \sqrt{\frac{1-\cos(x)}{2}} = \sin\left(\frac{x}{2}\right) \\
&= 2\sin\left(\frac{\pi\alpha}{4}\right)
\end{aligned}$$

and the phase in (3.15) can be found by the following calculations:

$$\begin{aligned}
\angle\, X^k_{z,\alpha}(\mathrm{j}\omega)\Big|_z &= k\ \arctan\left(\frac{-\sin\left(\frac{\pi\alpha}{2}\right)}{1-\cos\left(\frac{\pi\alpha}{2}\right)}\right) \\
&= k\ \arctan\left(\frac{-\sin\left(2\frac{\pi\alpha}{4}\right)}{1-\cos\left(2\frac{\pi\alpha}{4}\right)}\right) , \quad \begin{aligned} \sin(2x) &= 2\sin(x)\cos(x), \\ \cos(2x) &= 1-2\sin^2(x) \end{aligned} \\
&= k\ \arctan\left(\frac{-2\sin\left(\frac{\pi\alpha}{4}\right)\cos\left(\frac{\pi\alpha}{4}\right)}{1-\left(1-2\sin^2\left(\frac{\pi\alpha}{4}\right)\right)}\right) \\
&= k\ \arctan\left(\frac{-\cos\left(\frac{\pi\alpha}{4}\right)}{\sin\left(\frac{\pi\alpha}{4}\right)}\right) , \quad \frac{-\cos(x)}{\sin(x)} = -\cot(x) = \cot(-x) \\
&= k\ \arctan\left(\cot\left(\frac{-\pi\alpha}{4}\right)\right), \cot(x) = -\tan\left(x+\frac{\pi}{2}\right) = \tan\left(-x-\frac{\pi}{2}\right) \\
&= k\ \arctan\left(\tan\left(\frac{\pi\alpha}{4}-\frac{\pi}{2}\right)\right) \\
&= k\ \frac{\pi}{2}\left(\frac{\alpha}{2}-1\right).
\end{aligned}$$

A.1.2 Implicit Pseudo Zeros and Poles

In order to calculate the magnitude and phase of the implicit terms $\tilde{Q}^k_{z,\nu}$ and $\tilde{X}^k_{z,\alpha}$ for $z = \omega_0 e^{\mathrm{j}\varphi}$, $z \in \mathbb{C}_+$, without loss of generality consider

$$\begin{aligned}
\tilde{Q}^k_{z,\nu}(\mathrm{j}\omega) &= \left(1 + \frac{\mathrm{j}\omega}{z}\right)^{k\frac{\nu-1}{\nu}} = \left(1 + \frac{\mathrm{j}\omega}{\omega_0 e^{\mathrm{j}\varphi}}\right)^{k\frac{\nu-1}{\nu}} \\
&= \left(1 + \frac{\omega}{\omega_0} e^{\mathrm{j}(\pi-\varphi)}\right)^{k\frac{\nu-1}{\nu}} = \left(1 + \frac{\omega}{\omega_0}\left[\cos(\pi-\varphi) + \mathrm{j}\sin(\pi-\varphi)\right]\right)^{k\frac{\nu-1}{\nu}} \\
&= \left(1 + \frac{\omega}{\omega_0}\left[-\cos(\varphi) + \mathrm{j}\sin(\varphi)\right]\right)^{k\frac{\nu-1}{\nu}}
\end{aligned}$$

leading to

$$\begin{aligned}
\left|\tilde{Q}^k_{z,\nu}(\mathrm{j}\omega)\right|^2 &= \left(1 - 2\frac{\omega}{\omega_0}\cos(\varphi) + \left(\frac{\omega}{\omega_0}\right)^2\right)^{k\frac{\nu-1}{\nu}} \qquad \text{and} \\
\angle\tilde{Q}^k_{z,\nu}(\mathrm{j}\omega) &= k\frac{\nu-1}{\nu}\ \arctan\left(\frac{\frac{\omega}{\omega_0}\sin(\varphi)}{1 - \frac{\omega}{\omega_0}\cos(\varphi)}\right).
\end{aligned}$$

Note that $|\varphi| < \pi$, therefore $\cos(\varphi) < 0$ and thus $\left|\tilde{Q}^k_{z,\nu}(\mathrm{j}\omega)\right|^2 > 0\ \forall\omega \in \mathbb{R}_+ \cup \{0\}$. Analogue calculations lead to the analytic formulations for $\tilde{X}^k_{z,\alpha}(\mathrm{j}\omega)$.

A.1.3 Conjugate Complex Pair of Pseudo Zeros or Poles

The result in (3.27) can be found by the following calculations, where the zero-pair is $z = \omega_0 e^{\mathrm{j}\varphi}$ and $\bar{z} = \omega_0 e^{-\mathrm{j}\varphi}$:

$$\begin{aligned}
X_{z,\alpha}(s)X_{\bar{z},\alpha}(s) &= \left(1 - \left(\frac{s}{z}\right)^\alpha\right)\left(1 - \left(\frac{s}{\bar{z}}\right)^\alpha\right) \\
&= \frac{1}{z^\alpha \bar{z}^\alpha}\left(z^\alpha - s^\alpha\right)\left(\bar{z}^\alpha - s^\alpha\right) \\
&= \frac{1}{\left(\omega_0^2 e^{\mathrm{j}(\varphi-\varphi)}\right)^\alpha}\left(\left(\omega_0^2 e^{\mathrm{j}(\varphi-\varphi)}\right)^\alpha - s^\alpha\left(\omega_0^\alpha e^{\mathrm{j}\varphi\alpha} + \omega_0^\alpha e^{-\mathrm{j}\varphi\alpha}\right) + s^{2\alpha}\right) \\
&= \frac{1}{\omega_0^{2\alpha}}\left(s^{2\alpha} - s^\alpha\omega_0^\alpha\left(e^{\mathrm{j}\varphi\alpha} + e^{-\mathrm{j}\varphi\alpha}\right) + \omega_0^{2\alpha}\right), \quad \cos(\psi) = \frac{e^{\mathrm{j}\psi} + e^{-\mathrm{j}\psi}}{2} \\
&= \frac{1}{\omega_0^{2\alpha}}\left(s^{2\alpha} - 2\left(s\omega_0\right)^\alpha\cos(\varphi\alpha) + \omega_0^{2\alpha}\right).
\end{aligned}$$

The analysis of $X_{z,\alpha}(\mathrm{j}\omega)X_{\bar{z},\alpha}(\mathrm{j}\omega)$ leads to

$$\begin{aligned}
X_{z,\alpha}(\mathrm{j}\omega)X_{\bar{z},\alpha}(\mathrm{j}\omega) &= \frac{1}{\omega_0^{2\alpha}}\left((\mathrm{j}\omega)^{2\alpha} - 2\left(\mathrm{j}\omega\omega_0\right)^{\alpha}\cos\left(\varphi\alpha\right) + \omega_0^{2\alpha}\right) \\
&= 1 - 2e^{\mathrm{j}\frac{\pi\alpha}{2}}\left(\frac{\omega}{\omega_0}\right)^{\alpha}\cos\left(\varphi\alpha\right) + e^{\mathrm{j}\pi\alpha}\left(\frac{\omega}{\omega_0}\right)^{2\alpha} \\
&= 1 - 2\left(\frac{\omega}{\omega_0}\right)^{\alpha}\cos\left(\varphi\alpha\right)\left[\cos\left(\frac{\pi\alpha}{2}\right) + \mathrm{j}\sin\left(\frac{\pi\alpha}{2}\right)\right] \\
&\quad + \left(\frac{\omega}{\omega_0}\right)^{2\alpha}\left[\cos\left(\pi\alpha\right) + \mathrm{j}\sin\left(\pi\alpha\right)\right] \\
&= 1 - 2\left(\frac{\omega}{\omega_0}\right)^{\alpha}\cos\left(\varphi\alpha\right)\cos\left(\frac{\pi\alpha}{2}\right) + \left(\frac{\omega}{\omega_0}\right)^{2\alpha}\cos\left(\pi\alpha\right) \\
&\quad + \mathrm{j}\left[\left(\frac{\omega}{\omega_0}\right)^{2\alpha}\sin\left(\pi\alpha\right) - 2\left(\frac{\omega}{\omega_0}\right)^{\alpha}\cos\left(\varphi\alpha\right)\sin\left(\frac{\pi\alpha}{2}\right)\right]
\end{aligned}$$

and thus the magnitude and phase can be calculated. As this is straight forward and does not disclose further insights, this task is left to the diligent reader. Another possibility is to directly use (3.2) and (3.3) for z and $\bar{z}$, as they are suitable for complex zeros.

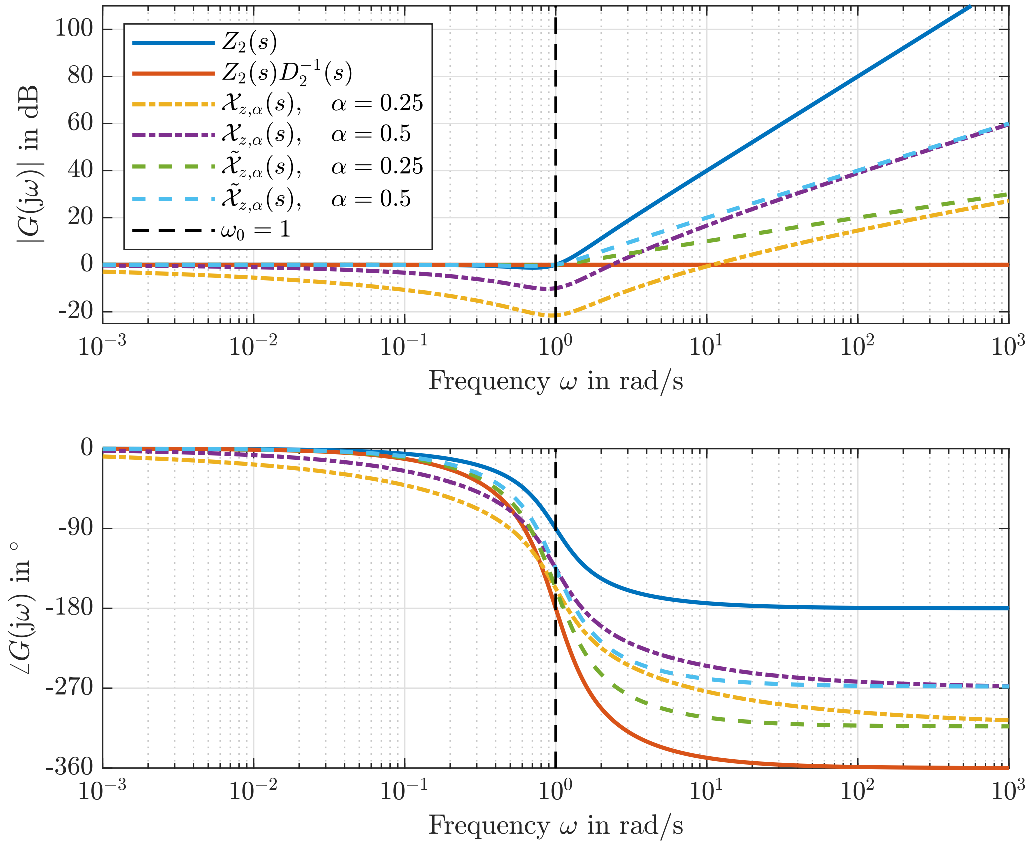

Figure A.2: Bode plot of $\mathcal{X}_{z,\alpha}$ and $\tilde{\mathcal{X}}_{z,\alpha}$ for $z = 1e^{\mathrm{j}\frac{\pi}{3}}$ and $\alpha \in \{0.25, 0.5\}$ opposite to the integer-order term Z_2 and its pseudo compensation $Z_2D_2^{-1}$.

The Bode plot of a pair of pseudo zeros is shown in Figure A.2.

A.2 Controller Design

This section covers the relevant background for the statements of Section 5.2. First, the differences between the designed PI-lead controller and a similar PI controller are considered (Section 5.2.4). It follows a brief derivation of the PI$^{\mu}$ controller design which is mentioned in Section 5.2.5.

A.2.1 Small Communication Delay τ_2

Figure A.3 shows a Bode plot of the PI-Lead controller of (5.18) and the similar PI controller of (5.19). The asymptotic fit is clearly visible, however differences in the crossover region ($\omega_{\mathrm{c,FO},2} = 2.41$ rad/s) can be observed as well.

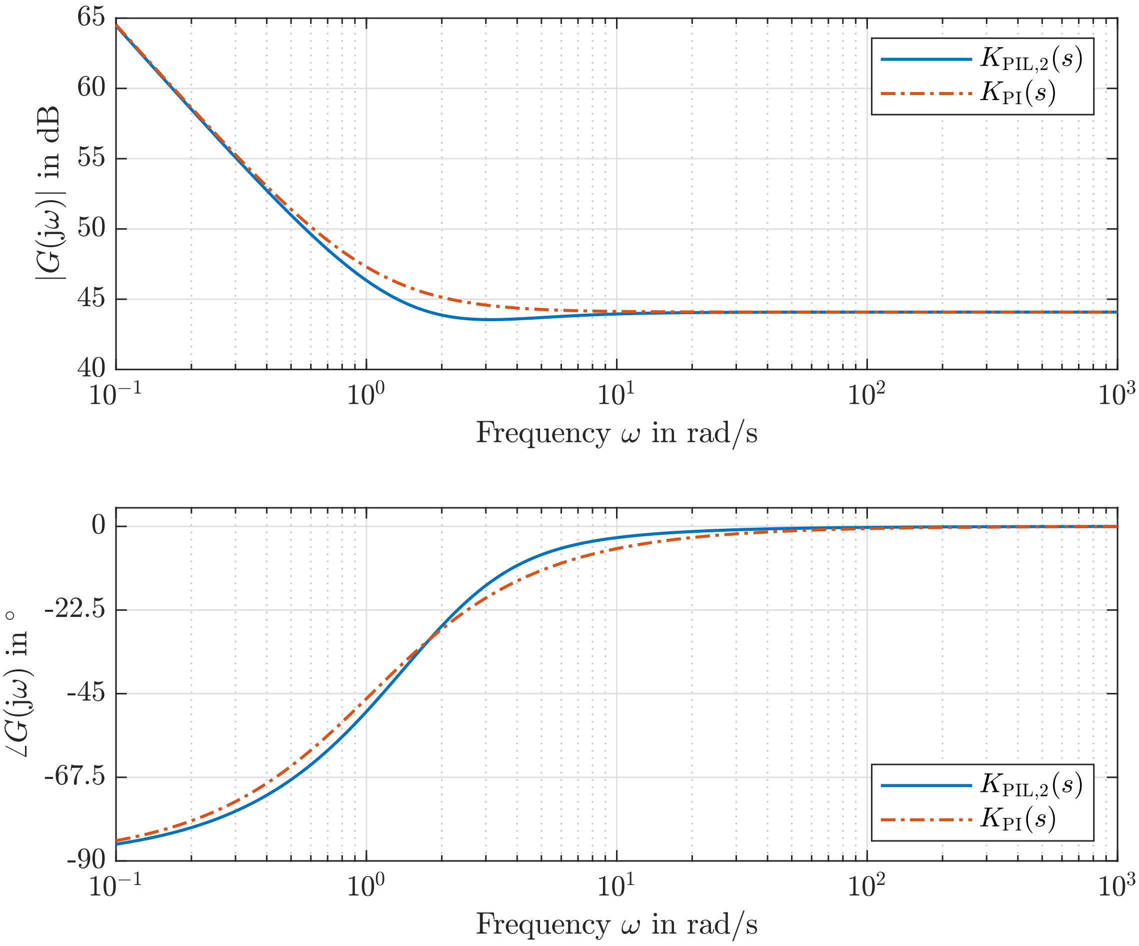

Figure A.3: Bode plot of the PI-Lead controller $K_{\mathrm{PIL},2}$ of (5.18) opposite to a similar PI controller K_{PI} of (5.19).

A.2.2 PI$^\mu$ Controller Design for the Dominant Delay τ_1

A natural way to enlarge the phase margin in the scope of fractional-order controller design is to use an integrator of non-integer order. As discussed in Section 2.1.4, it reduces the phase lag to $-\mu\,90°$ regarding the fractional-order integrator $s^{-\mu}$, $\mu \in (0,1]$. We present such a controller for the dominant communication delay and simulation results in this section.

Table A.1: Elements of a PI$^\mu$ controller for the dominant delay $\tau_1 = 0.3844\,\mathrm{s}$.

Element	**(FO) Transfer Function**	**Parameter Values**
PI$^\mu$ Controller	$K_{\mathrm{PI}^\mu}(s) = k_\mathrm{p} \frac{T_\mathrm{i} s^\mu + 1}{T_\mathrm{i} s^\mu}$	$k_\mathrm{p} = 45$, $T_\mathrm{i} = 0.9$, $\mu = \frac{1}{8}$
Part. Comp. Padé-zero	$\tilde{Q}_{\mathrm{z},2}(s) = \left(1 + \frac{s}{z}\right)^{\frac{1}{\nu}}$	$z = \frac{\tau_1}{2}$, $\nu = 2$
Part. Comp. Pole-Pair	$\tilde{\mathcal{X}}_{p,\alpha}(s) = \frac{1}{\omega_0^{2\alpha}} \left(s^2 - 2s\omega_0 \cos(\varphi) + \omega_0^2\right)^\alpha$	$\omega_0 = 16.346\,\mathrm{rad/s}$, $\varphi = 91.8°$, $\alpha = 0.5$
Compensation Padé-pole	$Q_p(s) = 1 - \frac{s}{p}$	$p = -\frac{\tau_1}{2}$
Additional Damping at ω_0	$Q_\mathrm{n}(s) = 1 - \frac{s}{p_\mathrm{n}}$	$p_\mathrm{n} = -10$

Aiming at a crossover frequency similar to $\omega_{\mathrm{c,FO},1} = 1.48$ rad/s, a PI$^\mu$ controller is determined that consists of the elements summarized in Table A.1. The overall fractional-order controller is thus given by

$$C_{\mathrm{PI}^\mu}(s) = \frac{K_{\mathrm{PI}^\mu}(s)\tilde{\mathcal{X}}_{p,\alpha(s)} Q_p(s)}{\tilde{Q}_{\mathrm{z},2}(s) Q_\mathrm{n}(s)}.$$

In contrast to the controller design of Section 5.2, here the stable pole of the first-order Padé-term is addressed, but the resonance peak is only partially compensated using the implicit term. Note that the integer-order approximations of the fractional-order PI$^\mu$ controller yield proper transfer functions The corresponding approximation parameters are summarized in Table A.2. To illustrate the effect of the approximation range, two cases are considered for the approximation of the PI$^\mu$ controller element.

Table A.2: Oustaloup approximation (2.15) parameters for the fractional-order elements of C_{PI^μ}.

FO Term	$\boldsymbol{\omega_\mathrm{l}}$ **in rad/s**	$\boldsymbol{\omega_\mathrm{h}}$ **in rad/s**	$\boldsymbol{N}$
$K_{\mathrm{PI}^\mu,1}(s)$	0.1	10	1
$K_{\mathrm{PI}^\mu,2}(s)$	0.01	10	1
$\tilde{Q}_{\mathrm{z},2}(s)$	0.05	50	1
$\tilde{\mathcal{X}}_{p,\alpha}(s)$	0.5	500	1

First, the controller $C_{\mathrm{PI}^\mu,1}$ is determined by using the Oustaloup approximation of $K_{\mathrm{PI}^\mu,1}$. In the second case, the lower limit is extended to $\omega_{\mathrm{l},2} = 0.01\,\mathrm{rad/s}$ leading to the controller $C_{\mathrm{PI}^\mu,2}$. This is the only difference between these controllers.

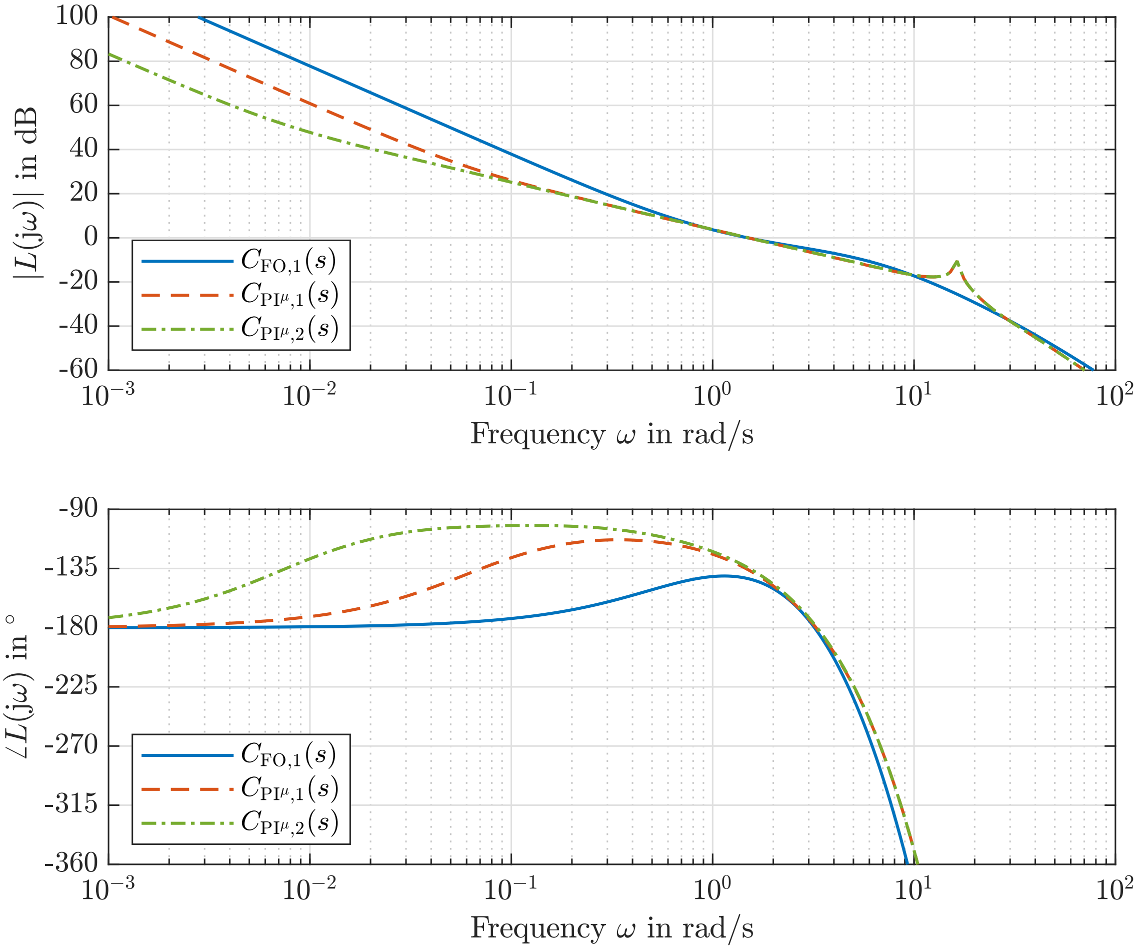

Figure A.4: Bode plot of the open loop for integer-order approximations of the PI^μ controller for the dominant delay τ_1.

A Bode plot of both resulting PI^μ controllers is depicted in Figure A.4 opposite to $C_{\mathrm{FO},1}$ of (5.17). The controller with the smaller approximation range achieves a phase margin of $\Psi_{\mathrm{PI}^\mu,1} = 43.99°$, the larger frequency band yields $\Psi_{\mathrm{PI}^\mu,2} = 45.53°$, while the crossover frequencies coincide: $\omega_{\mathrm{c},\mathrm{PI}^\mu} = 1.50\,\mathrm{rad/s}$. The differences between the controllers are clearly visible at lower frequencies. Both controllers naturally result in less magnitude slope for low frequencies due to the fractional-order integrator. However, the positive phase exceeds the PI-lead based controller $C_{\mathrm{FO},1}$. Furthermore, a magnitude peak at ω_0 can be observed since the conjugate complex pair of stable poles is partially compensated with the implicit term.

Since the disturbance attenuation of input disturbances is of special interest, consider the magnitude plot of the disturbance sensitivity functions (5.21) in Figure A.5.

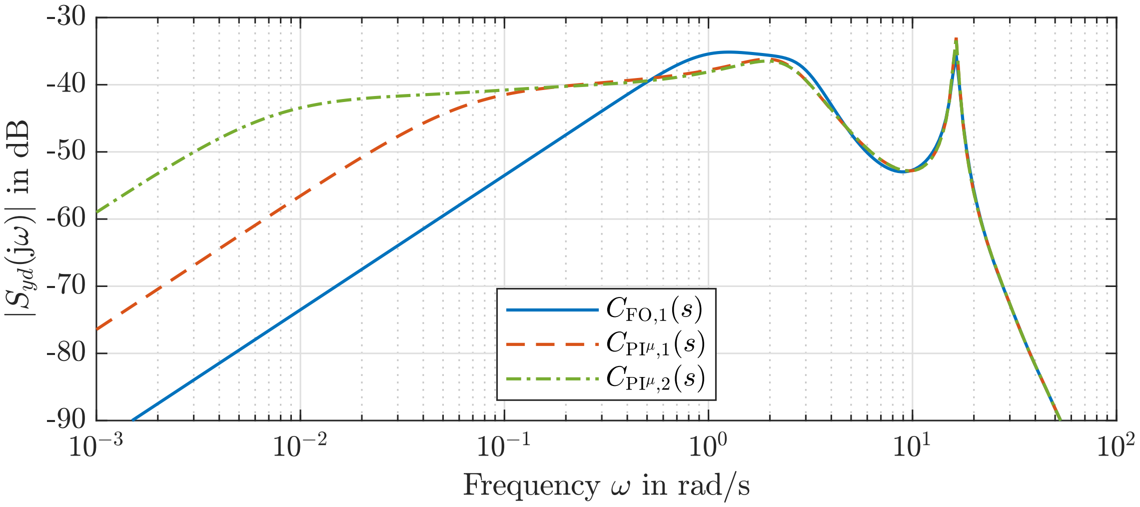

Figure A.5: Magnitude plot of the disturbance sensitivity function S_{yd} using different integer-order approximations of the PI$^{\mu}$ controller for the dominant delay τ_1.

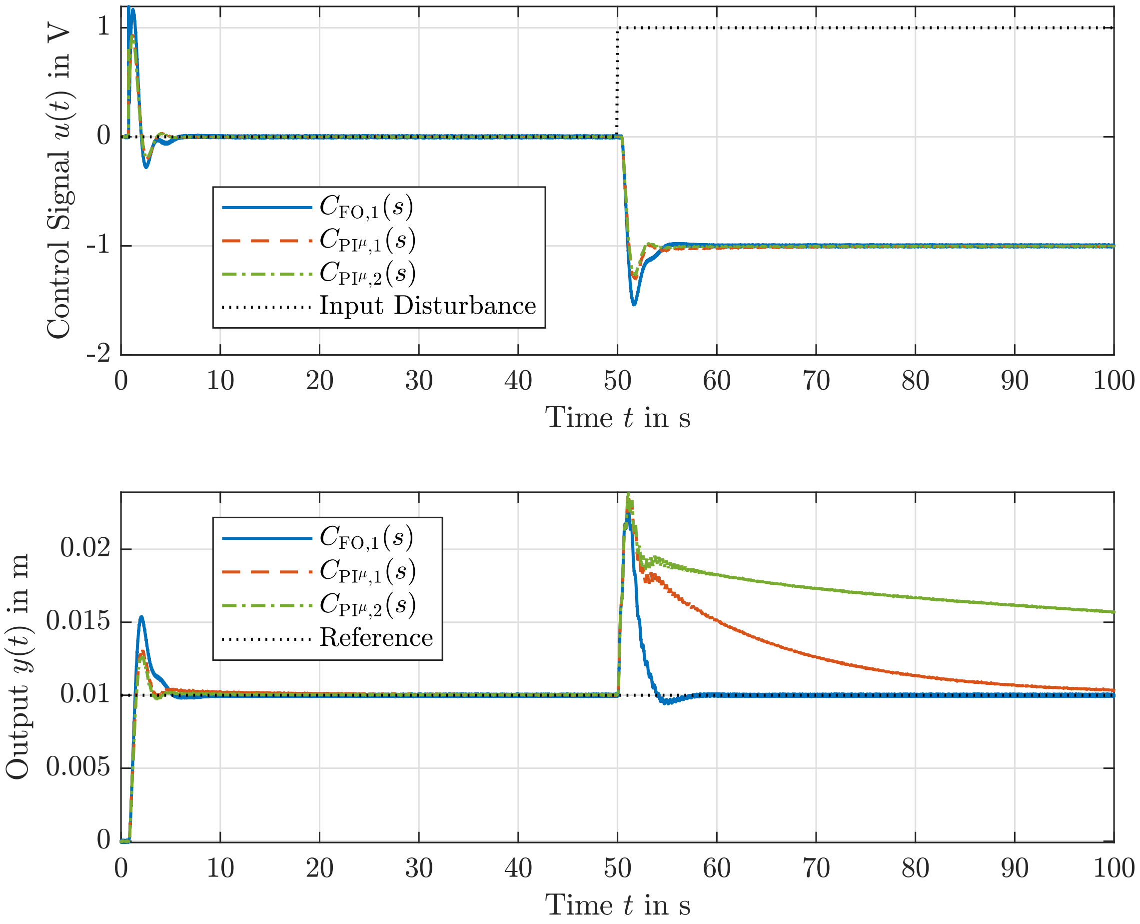

Figure A.6: Time response to a step in the reference $r(t) = \sigma(t)$ as well as the disturbance $d_u(t) = \sigma(t - t_d)$ at $t_d = 50\,\mathrm{s}$ using a fractional-order PI$^{\mu}$ controller.

Due to the small slope at low frequencies, only slow convergence following a disturbance step is expected.

The simulation results for a reference step at $t_r = 0\,\mathrm{s}$, i.e. $r(t) = \sigma(t)$, and a step of the input disturbance $d_u(t)$ at $t_d = 50\,\mathrm{s}$, resulting in $d_u(t) = \sigma(t - t_d)$, are depicted in Figure A.6. Note that all controllers are realized in the standard control configuration (see Figure 3.6), hence without a prefilter.

The results clearly illustrate the effect of the different approximation ranges on the decay rate of the disturbance response. The initial overshooting is significantly reduced compared to $C_{\mathrm{FO},1}$, however, the disturbance responses are not sufficient. Regarding the simulation and experimental studies in Chapter 6, $C_{\mathrm{FO},1}$ is combined with a prefilter as a second-degree of freedom leading to precise tracking capabilities.

A.3 Simulation and Experimental Results

In this section, we present further simulation and experimental results that are only briefly mentioned in Chapter 6.

A.3.1 Disturbance Attenuation

Exemplary time responses to the input disturbance $d_u(t)$ acting in the frequency range Ω_{d} for the nominal value of the small communication delay $\tau = \tau_2$ and initial condition $x_{0,\mathrm{d}}$ are depicted in Figure A.7 (next page). Only a short period of time is presented. The disturbance injection starts at $t = 2\,\mathrm{s}$. The detailed simulation model obviously captures the main process characteristics.

The frequency spectra of the disturbance attenuation experiments for the nominal value of the dominant communication delay $\tau = \tau_1$ are depicted in Figure A.8 (next page). The amplitude peak of the jitter signal is clearly visible at $\omega_{\mathrm{j}} = 450\,\mathrm{rad/s}$, however appears to be well damped by the process.

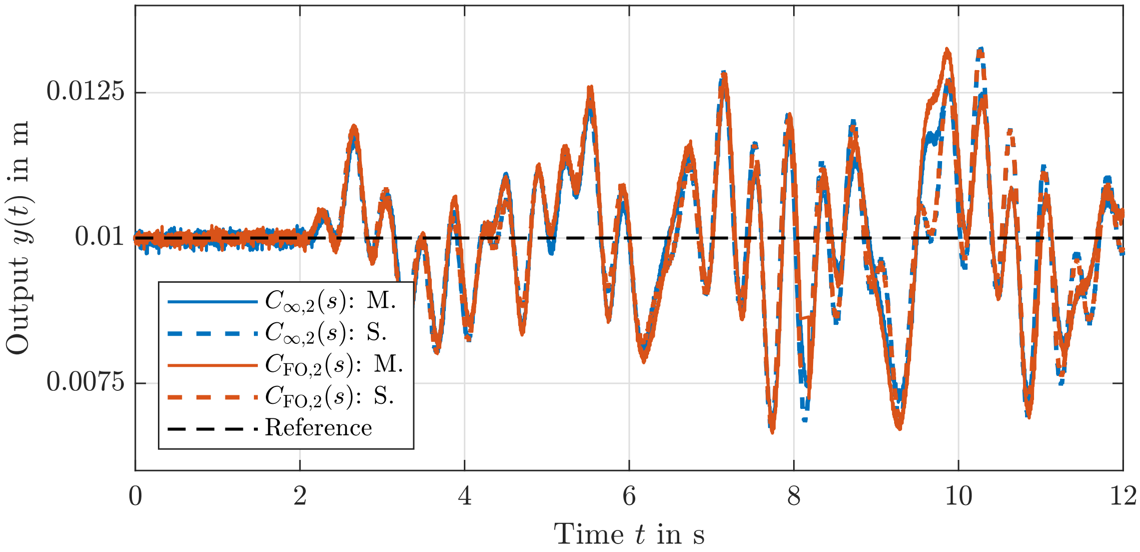

Figure A.7: Exemplary time responses to the input disturbance for both controllers with the nominal value of the small time delay $\tau = \tau_2$. Measurement and simulation are abbreviated by 'M.' and 'S.', respectively.

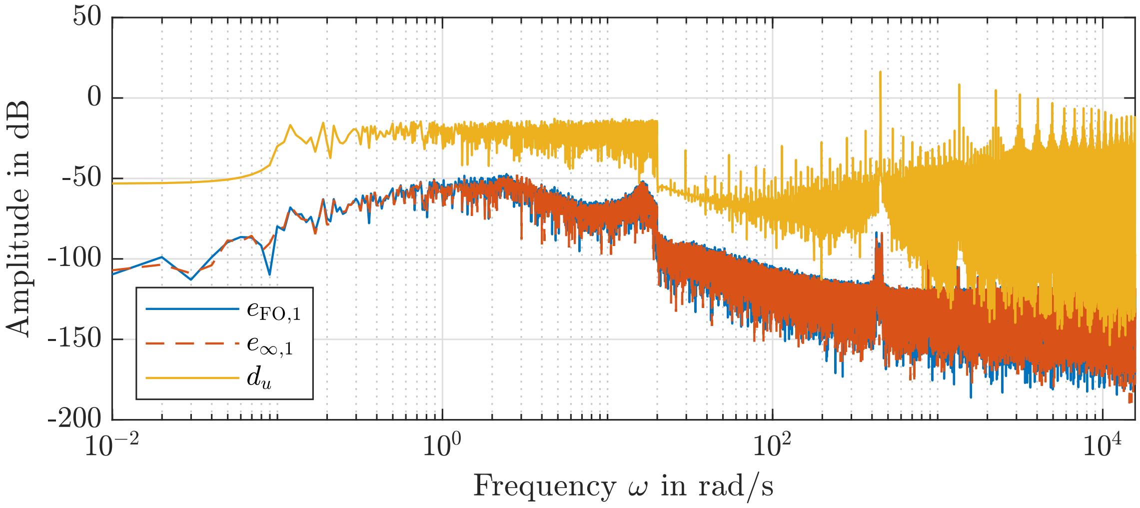

Figure A.8: Entire frequency spectra of the input disturbance and the control errors for experiments with both controllers $C_{\mathrm{FO},1}$ and $C_{\infty,1}$ and the nominal value of the dominant communication delay $\tau = \tau_1$.

Regarding the disturbance attenuation experiments for the small delay $\tau = \tau_2$, similar frequency spectra can be obtained. These are depicted in Figure A.9 (Page A 11) and also show the qualitative shape of the corresponding magnitude plot of the disturbance sensitivity function in Figure 5.10.

The frequency data can be evaluated in the relevant spectrum, i.e. for $\omega \in \Omega_{\mathrm{d}}$, leading to similar results as the RMS error values, which are summarized in Table A.3.

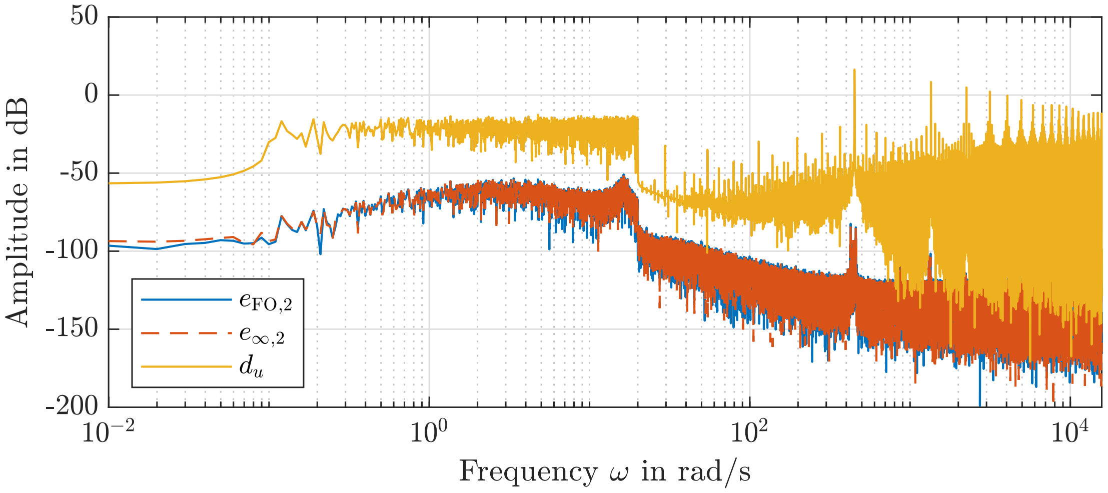

(a) Entire spectra.

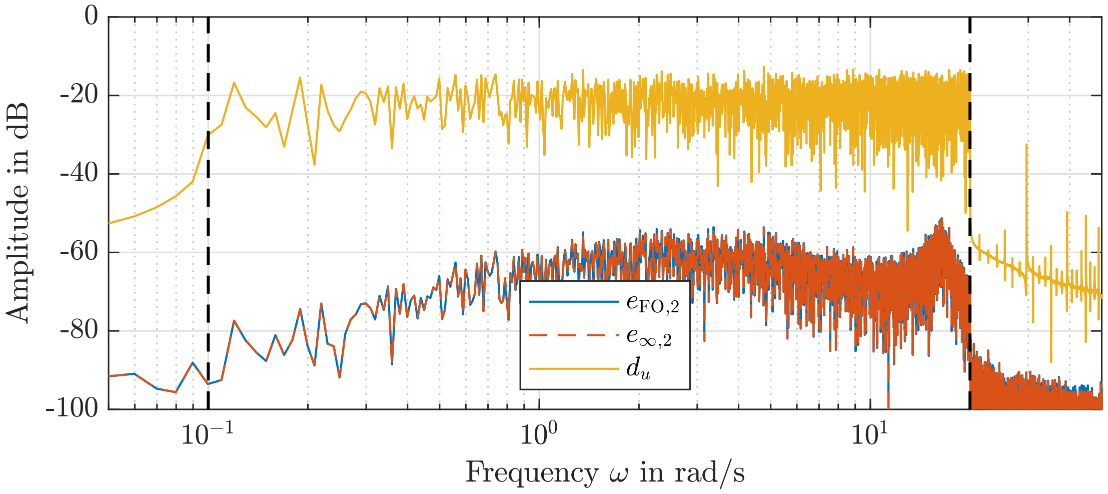

(b) Relevant spectra.

Figure A.9: Frequency spectra of the input disturbance and the control errors for experiments with both controllers $C_{\mathrm{FO},2}$ and $C_{\infty,2}$ and the nominal value of the dominant communication delay $\tau = \tau_2$. The dashed black lines indicate the frequency spectrum of the input disturbance Ω_{d} which is used to calculate the metrics in Table A.3.

Table A.3: Frequency analysis of the disturbance attenuation experiments for both delays with $|e(\omega)|$ in dB and $\omega \in \Omega_{\mathrm{d}} = \left[0.1\,\frac{\mathrm{rad}}{\mathrm{s}},\, 20\,\frac{\mathrm{rad}}{\mathrm{s}}\right]$.

		Dominant Delay τ_1			**Small Delay τ_2**		
Contr.	**Metric**	$\tau = 0.9\tau_1$	$\tau = \tau_1$	$\tau = 1.1\tau_1$	$\tau = 0.9\tau_2$	$\tau = \tau_2$	$\tau = 1.1\tau_2$
$C_{\infty,i}$	$\max_\omega \lvert e(\omega)\rvert$	-49.077	-47.253	-46.966	-50.944	-50.914	-50.944
	$\mu(\lvert e(\omega)\rvert)$	-60.792	-60.369	-60.219	-62.591	-62.419	-62.179
	$\min_\omega \lvert e(\omega)\rvert$	-104.036	-99.844	-99.825	-108.445	-101.959	-95.760
$C_{\mathrm{FO},i}$	$\max_\omega \lvert e(\omega)\rvert$	-48.330	-47.726	-46.920	-51.372	-51.253	-50.935
	$\mu(\lvert e(\omega)\rvert)$	-60.723	-60.742	-60.380	-62.682	-62.329	-61.877
	$\min_\omega \lvert e(\omega)\rvert$	-108.204	-102.271	-100.618	-97.324	-100.264	-95.741

A.3.2 Tracking Performance

The simulation and experimental results for the tracking experiments are discussed in Section 6.2. However, exemplary time responses for the set-point change `lm` are only presented for the dominant communication delay τ_1. Therefore, analog results regarding the small delay τ_1 are presented in this section. For a detailed discussion see Section 6.2.1.

Considering the set-point change `lm` for the small communication delay, the outputs are depicted in Figure A.10. The simulation results are restricted to the nominal case $\tau = \tau_2$, since the variation is very little only.

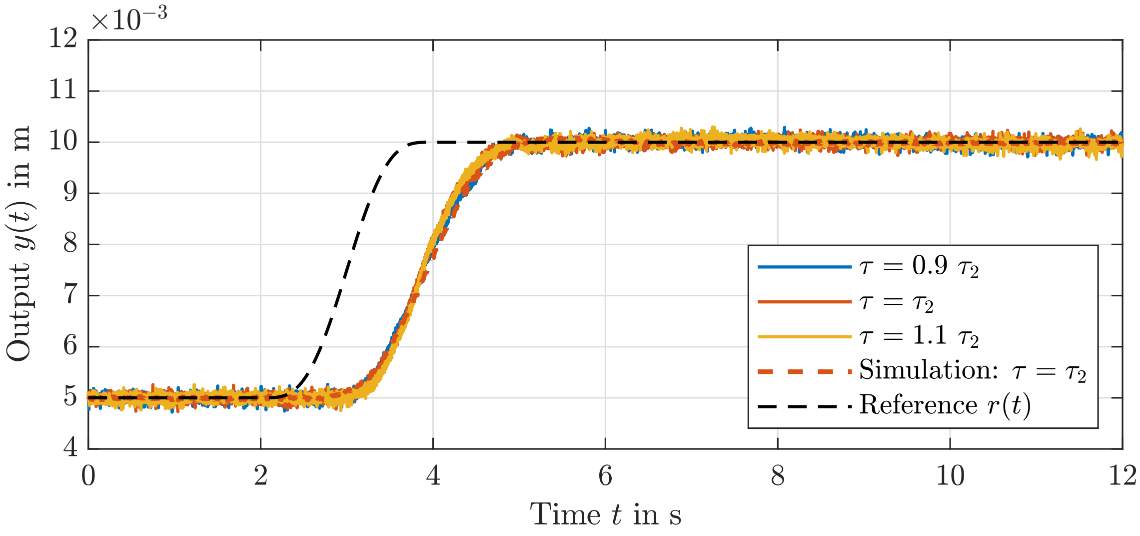

(a) Closed-loop response using $C_{\infty,2}$ (5.9).

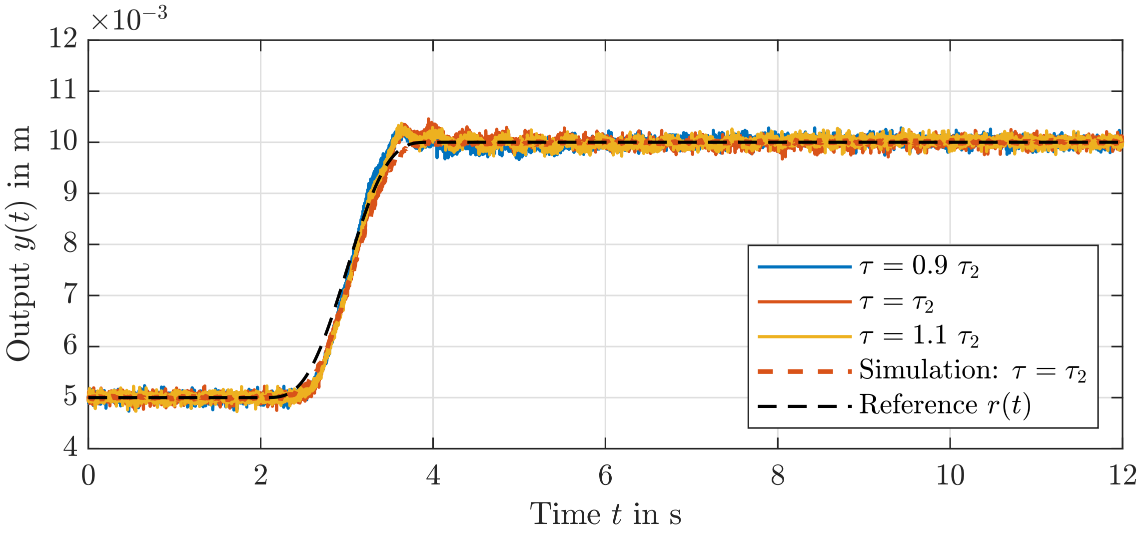

(b) Closed-loop response using $C_{\mathrm{FO},2}$ (5.20) with prefilter (5.14).

Figure A.10: Time responses to the set-point change for both controllers and the small delay with the initial conditions $x_{0,\mathrm{t}} = [0.005 \;\; 0 \;\; 0.005 \;\; 0]^\top$ and a variation of the plant's time delay by ±10 %.

The corresponding control inputs are shown in Figure A.11. As discussed in Section 6.2.1, they show significantly more noise amplification. This is expected due to the higher open-loop crossover frequencies.

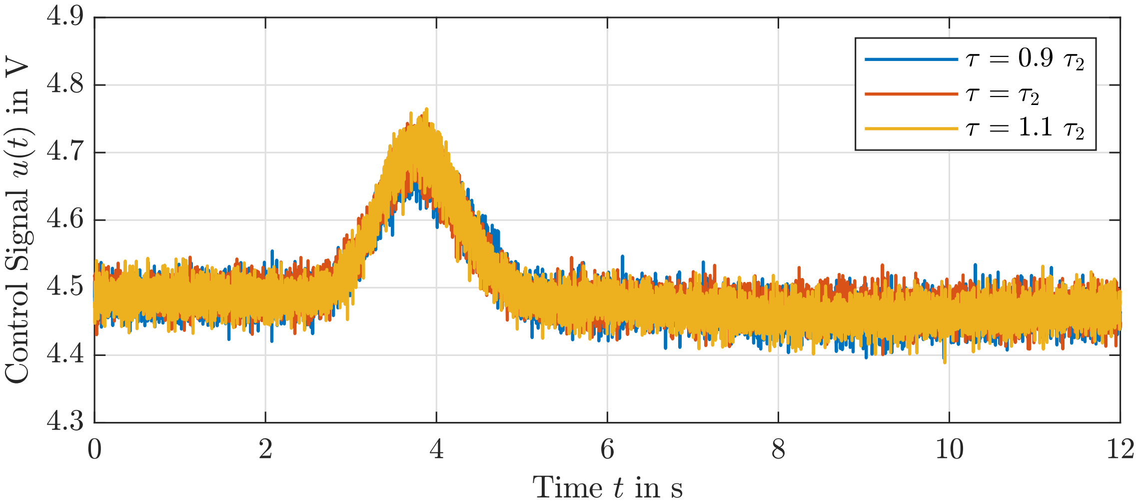

(a) Control signal for the response in Figure A.10a.

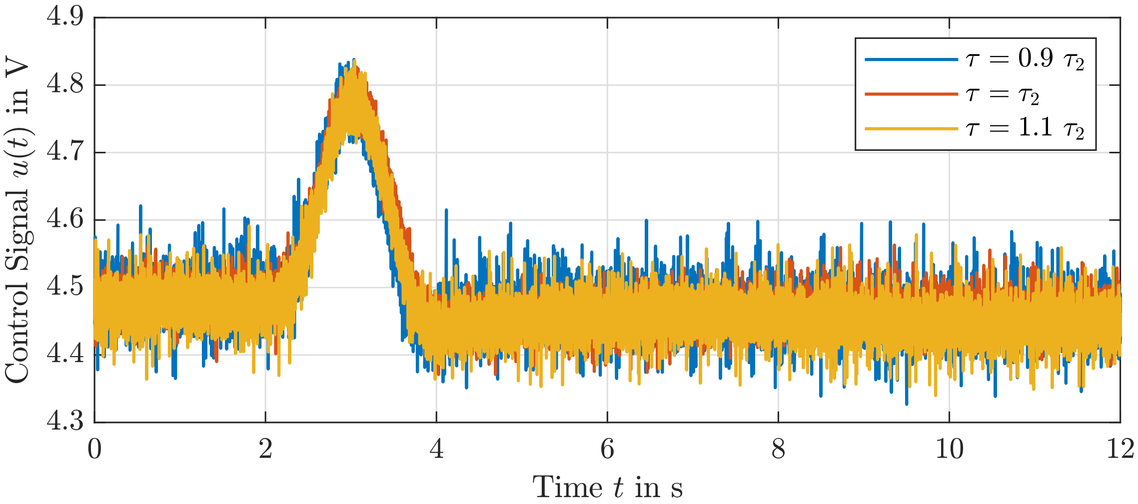

(b) Control signal for the response in Figure A.10b.

Figure A.11: Control signals for the time responses in Figure A.10.

Finally, we consider the entire tracking experiments as in Section 6.2.2. The histograms of the remaining evaluation metrics are summarized in Figure A.12. It can be observed that the error-related evaluation metrics are smaller for the small delay τ_2 and for $C_{\mathrm{FO},i}$ in general. This is not the case for the maximum absolute control effort in Figures A.12g and A.12h, which increases for the dominant delay. Furthermore, it is independent of the set-point change direction. Regarding the small communication delay, the metrics of the two controllers differ in the fourth digit only.

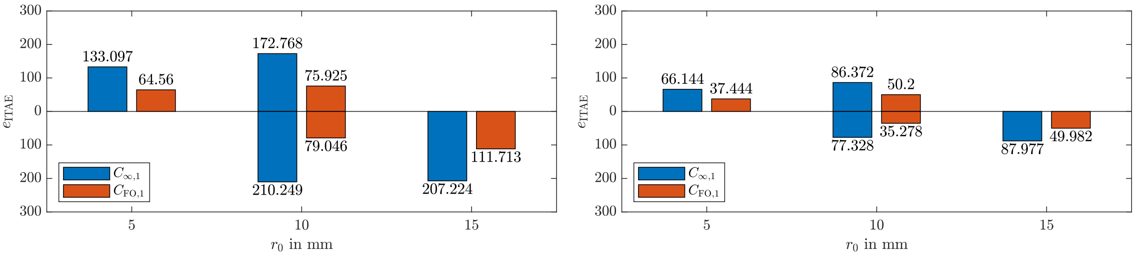

(a) Dominant communication delay $\tau = \tau_1$.

(b) Small communication delay $\tau = \tau_2$.

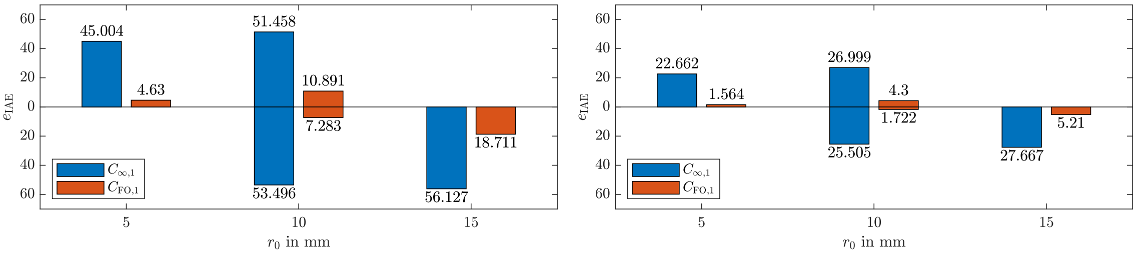

(c) Dominant communication delay $\tau = \tau_1$.

(d) Small communication delay $\tau = \tau_2$.

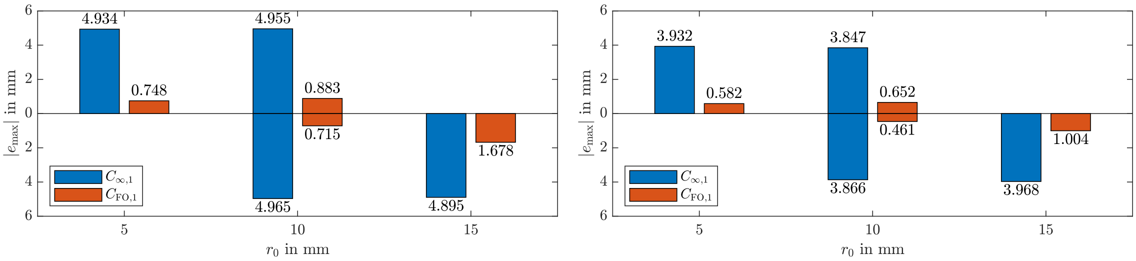

(e) Dominant communication delay $\tau = \tau_1$.

(f) Small communication delay $\tau = \tau_2$.

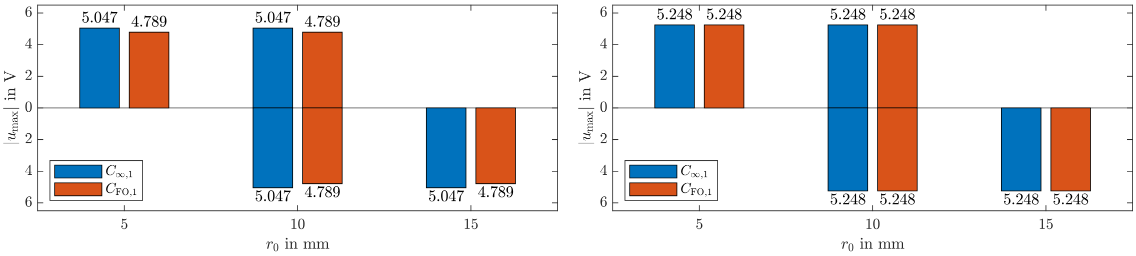

(g) Dominant communication delay $\tau = \tau_1$.

(h) Small communication delay $\tau = \tau_2$.

Figure A.12: Histograms of ITAE e_{ITAE}, IAE e_{IAE}, maximum error $|e_{\max}|$ and maximum control effort $|u_{\max}|$ for $\tau = \tau_i$ and both controllers. The bar orientation shows the direction of the set-point changes, e.g. the bars at the left-hand side ($r_0 = 5\,\mathrm{mm}$) correspond to the set-point change `lm`.